UNIVERSIDADE DE LISBOA
INSTITUTO SUPERIOR TÉCNICO

Scalar field effects on the motion of stars

Miguel Coelho Ferreira

Supervisor: Doctor Vítor Manuel dos Santos Cardoso

Thesis approved in public session to obtain the PhD Degree in Physics
Jury final classification: Pass with Distinction

2019

TÉCNICO LISBOA

UNIVERSIDADE DE LISBOA
INSTITUTO SUPERIOR TÉCNICO

Scalar field effects on the motion of stars

Miguel Coelho Ferreira

Supervisor: Doctor Vítor Manuel dos Santos Cardoso

Thesis approved in public session to obtain the PhD Degree in Physics
Jury final classification: Pass with Distinction

Jury

Chairperson: Doctor José Pizarro de Sande e Lemos, Instituto Superior Técnico, Universidade de Lisboa

Members of the Committee:

Doctor Pedro Tonnies Gil Ferreira, Department of Physics, University of Oxford, UK

Doctor Vítor Manuel dos Santos Cardoso, Instituto Superior Técnico, Universidade de Lisboa

Doctor Caio Filipe Bezerra Macedo, Faculdade de Física, Universidade Federal do Pará, Brasil

Doctor Miguel Rodrigues Zilhão Nogueira, Instituto Superior Técnico, Universidade de Lisboa

Funding Institution:

Grant number PD/BD/113481/2015 from Fundação para a Ciência e a Tecnologia

2019

El ánimo que somos se vuelca en sus productos [...], dedicado plenamente a crear, poseer y tomar forma; pero lo producido no tiene más vida que la de provenir de una creación, de un querer activo que *ya* se ha realizado, luego su vida está toda ella en el pasado y por tanto muerta en cierto modo: [...] toda obra es insuficiente (y también todo *status* público, todo nombre proprio, todo título académico o professional, toda construcción cara a los otros o frente a uno mismo de una personalidad dada de una vez por todas) porque en ella lo posible, la *dynamis*, adopta el rostro fatal de lo que es lo que es y no otra cosa, de la identidad necesaria. La posibilidad, la *dynamis*, la liberdad... son de lo que está echo el aire que respira nuestra subjetividad, cuyo principio es acción.

Fernando Savater, *Invitación a la ética*

Resumo

Campos escalares fundamentais são ingredientes essenciais de algumas das soluções propostas para os mais prementes problemas da Física teórica moderna. A sua deteção pode contribuir para a compreensão, por exemplo, da composição da matéria escura e/ou do correto horizonte teórico para a Física à escala de Planck. Caso sejam verdadeiramente elementos do Universo físico, há boas razões para acreditar que estes campos dão origem a estruturas astrofisicamente relevantes. Nesta tese, estudamos a maneira como a presença de tais estruturas pode ser inferida a partir do seu efeito na dinâmica de corpos celestes.

Prestamos atenção a dois tipos de estruturas de campos escalares: estrelas de bosões e "nuvens" de bosões que se desenvolvem em torno de buracos negros em rotação. A estrelas de bosões são formadas devido ao colapso do campo escalar e as suas características podem ser variadas, dependendo do modelo e da escala de energia à qual estão a ser analisadas. Estas estrelas podem ser consideradas como imitadores de buracos negros, quando muito compactas, mas também como galos galácticos, nos casos em que são mais diluídas. Na presença de buracos negros em rotação, a existência de campos escalares leves promove o crescimento espontâneo de "nuvens" de bosões. Analisámos o efeito que estas nuvens escalares têm em sistemas binários de rácio de massa extremo – sistema binários nos quais um buraco negro supermassivo (BNSM) é orbitado por um objeto muito menos massivo. Concluímos que, se o BNSM está rodeado por uma estrutura de campo escalar real, órbitas circulares equatoriais desenvolvem uma estrutura ressonante que pode afetar de modo peculiar o binário. No cenário mais especifico do centro da Via Láctea, calculamos o efeito que uma nuvem de campo escalar complexo, suportada pelo BNSM central, tem na evolução orbital da estrela S2 e verificamos que tais efeitos podem ser detetados pela missão GRAVITY.

As estrelas de bosões não têm superfície física. Isso quer dizer que outras estrelas as podem penetrar e, ao fazê-lo, podem também as perturbar. Estudamos tal cenário com uma estrela de bosões diluída e apuramos que se desenvolvem aglomerados duradouros de campo escalar em rotação, mas a estrela de bosões não é destruída.

Palavras-chave: campos escalares, estrelas de bosões, buracos negros, órbitas estelares, centro da galáxia, mecânica celeste

Abstract

Fundamental scalar fields are essencial ingredients in proposed solutions to many of the most pressing problems in modern theoretical Physics. Their detection may shed light, for instance, on the composition of dark matter and/or on the correct theoretical landscape of Planck-scale physics. In the event of being actual elements of the physical Universe, there are good reasons to believe that these fields give rise to astrophysically-relevant structures. This thesis studies how the presence of such structures can be inferred from their effect on the dynamics of celestial bodies.

We focus on two types of scalar-field structures: boson stars and bosonic "clouds" grown from spinning black holes. Boson stars are formed due to the collapse of a scalar field and their characteristics can be very different, depending on the model and energy scale at which they are analysed. These structures can be useful black hole mimickers, when very compact, but are also proposed constituents of galactic haloes, when dilute. The very existence of light, scalar degrees of freedom triggers the growth of bosonic "clouds" around spinning black holes. We analyse the effect that these scalar cloud structures have on Extreme-Mass-Ratio-Inspirals – binary systems in which a supermassive black hole (SMBH) is orbited by a much lighter object. We find that if the SMBH is surrounded by a real scalar field structure, equatorial circular orbits develop a resonant structure, that may affect distintively the inspiral. In the more specific scenario of the center of Milky Way, we calculate the effect a complex scalar cloud supported by the central SMBH has on the orbital evolution of the S2 star, finding that those effects may be detected by the GRAVITY instrument.

Boson stars do not have a physical surface. This means that other stars can penetrate them and, in that process, disturb them too. We study such scenario with a diluted boson star and we find that long-lived rotating scalar-field clusters develop as a result, but the boson star is not destroyed.

Keywords: scalar fields, boson stars, black holes, stellar orbits, center of the galaxy, celestial mechanics

Acknowledgments

I would like to thank my parents and my brother for their unconditional support;

I would like to thank my girlfriend for taking care of me and for allowing me to take care of her: she is the compass that keeps me on track, reminding me which way is North;

I would like to thank my supervisor for his time, his patience and his scientific example, which inspires and motivates us all;

I would like to thank IDPASC for awarding me the scholarship that allowed me to pursue my PhD studies and to FCT which funded it (grant number PD/BD/113481/2015);

I would like to thank everyone at CENTRA (Center for Astrophysics and Gravitation) for their contribution in making this group such a dynamical and inspiring one. It was a great honor to be part of it for the last 4 years. I want to leave a special word of gratitude to professor José Lemos, Vincenzo Vitagliano, Sante Carloni, Viktor Czinner, Caio Macedo, Miguel Zilhão, David Hilditch, Sérgio Almeida, Manuel Torrinha, Dulce Conceição and Rita Sousa. I would also like to mention my office colleagues, specially Richard Brito, for his example of excellence and for always having time to listen to my doubts and problems, Filip Hejda, for the long and pleasant discussions, and Jorge Lopes, who accepted to proof-read this thesis. Finally, a very special word of appreciation to professor Paulo Garcia, for his encouragement, enthusiasm and companionship – without him, part of this thesis wouldn't have been written;

I would like to thank Júlia Oliveira, from Área de Pós-Graduação, and Natália Antunes, from LIP (Laboratório de Instrumentação e Física Experimental de Partículas), for their sympathy and for helping me navigate the bureaucracy when I most needed;

I would like to thank everyone at *Diferencial*, the IST's students' newspaper, for allowing me to be part of the project. It was an honor to participate! A special word to Afonso Anjos and to Francisco Moreira de Azevedo for their friendship and guidance;

I would like to thank my good friends Pedro Lencastre and Vasco Ferreira for proof-reading this thesis;

Finally, I would like to thank André C. Marta for developing the LaTeX template being used to write this thesis.

Contents

Preamble

The research presented in this thesis has been carried out at Center for Astrophysics and Gravitation (CENTRA) at Instituto Superior Técnico – Universidade de Lisboa.

I declare that this thesis is not substantially the same as any that I have submitted for a degree, diploma or other qualification at any other university and that no part of it has already been or is concurrently submitted for any such degree, diploma or other qualification.

Most of the work presented here is the outcome of collaborations with Professor Vítor Cardoso, Professor Caio Macedo and the GRAVITY Collaboration, particularly Professor Paulo Garcia. Most of the chapters of this thesis have been published. The publications here presented are included below:

1. Miguel C. Ferreira, Caio F. B. Macedo, Vítor Cardoso, " Orbital fingerprints of ultralight scalar fields around black holes", Phys. Rev. D **96** (2017) 083017, [arXiv:1710.00830];

2. Miguel C. Ferreira, " How do scalar-field dark matter halos react to orbiting bodies?", Phys. Rev D **99** (2019) 103008, [arXiv:1904.10777];

3. A. Amorim, M. Bauböck, M. Benisty, J.-P. Berger, Y. Clénet, V. Coudé du Forest, T. de Zeeuw, J. Dexter, G. Duvert, A. Eckart, F. Eisenhauer, Miguel C. Ferreira, F. Gao, Paulo J.V. Garcia, E. Gendron, R. Genzel, S. Gillessen, P. Gordo, M. Habibi, M. Horrobin, A. Jimenez-Rosales, L. Jocou, P. Kervella, S. Lacour, J.-B. Le Bouquin, P. Léna, T. Ott, M. Pössel, T. Paumard, K. Perraut, G. Perrin, O. Pfuhl, G. Rodriguez Coira, G. Rousset, O. Straub, C. Straubmeier, E. Sturm, F. Vincent, S. von Fellenberg, I. Waisberg, F. Widmann, "Scalar field effects on the orbit of S2 star", (accepted for publication in Monthly Notices of the Royal Astronomical Society), [arXiv:1908.06681]

I also collaborated with Mateja Bošković, Francisco Duque and Filipe S. Miguel in the publication

- Mateja Bošković, Francisco Duque, Miguel C. Ferreira, Filipe S. Miguel, Vítor Cardoso, " Motion in time-periodic backgrounds with applications to ultralight dark matter haloes at galactic centers", Phys. Rev D **98** (2018) 024037, [arXiv:1806.07331],

which is not included in this thesis.

Chapter 1

Introduction

Since the detection of the Higgs boson [1, 2], fundamental scalar fields entered the list of building blocks of Nature. This detection reinforces the suspicion that more of them exist. The idea is seductive because if verified, the new scalar fields may prove very useful in explaining poorly understood aspects of the physical world (such as the nature of dark matter) or in being smoking-guns of high-energy theories (such as string theory). Both their mass and the coupling to the Standard Model (SM) are expected to be very small, reducing the hopes of detecting them using particle colliders. In what follows, we will be exploring a less direct detection approach based on the hypothesis that scalar fields may form structures of astrophysical significance. These structures affect the motion of celestial bodies in unique ways, which can be ultimately related to the characteristics of the scalar field itself. By understanding these signatures, one can use them – in case of a comparison with observational data is possible – as hints for the existence of scalar fields.

1.1 Scalar fields

Scalar fields are the simplest objects one can have in a field theory. Their simplicity and versatility puts them in the center of the most important debates of modern physics, being used, for instance, to model inflation [3, 4], to model quintessence [5, 6], to describe extensions of General Relativity (GR) (see, for instance, Ref. [7]), or as new particles, such as the proposed Quantum Chromodynamics (QCD) axion [8–10] or the plethora of scalar fields that appear in the four-dimensional, low-energy description of string theory [11]. In this thesis, we are not specifically interested in their ancestry, so we will be considering the simple model of a free, massive scalar field that, at the energy scales in which GR is a good description of gravity, is minimally coupled to the underlying spacetime. This is our bedrock assumption.

Of all the scenarios mentioned above, scalar fields are introduced either *by hand* (i.e. they are used where they fit the restrictions of the corresponding theory) or consistently, in the cases their appearance is a consequence of mathematical manipulations associated with the structure of the theory. In spite of our lack of interest in the provenance of the scalar fields, there is one example that is particularly relevant: the String Axiverse scenario [12], in which scalar fields appear consistently in String Theory. The full String Theory framework requires more than four spacetime dimensions. Studying their four-dimensional effective structure amounts to go through a process of compactification. This process gives rise to several four-dimensional, massless scalar fields which can, due to non-perturbative effects, acquire mass [11]. This formation process resembles the one of the QCD axion that was introduced by Peccei and Quinn, Weinberg and Wilczek [8–10] as a solution to the QCD strong Charge-Parity (CP) problem. This original embodiment of the concept of axion – from now on the QCD axion – has received much attention and its characteristics are experimentally constrained (see, e.g., Ref. [13]). String theory axions, however, are less constrained and can, at least theoretically, have masses as small as 10^{-33} eV. Moreover, the coupling of these fields to the SM particles are expected to be very weak (see, for instance, Ref. [14] and references therein) and that is one of the reasons why these fields are proposed as Dark Matter (DM)-candidates [15].

Scalar fields with such low-mass and with negligible interactions with baryonic matter may prove difficult to be detected using collider experiments. The only relevant coupling of these ultra-light scalar fields to the SM is the one with the photon, and it is by exploring this coupling that most of the experimental efforts have tried to produce the particles described by these fields. The most well established experiments are light-shining-through-walls experiments [16], which try to produce axions by making a laser beam cross a region with a strong magnetic field, helioscopes [17], which try to detect axions produced in the solar core, and haloscopes [18] which target the detection of photons directly converted from axions. Other lines of research, focusing in less direct signatures have been suggested, and these ultralight scalar fields have shown to be copious sources of phenomenology: both cosmologically [19, 20], with axionic scalar fields leaving their imprint in cosmic microwave background anisotropies and in the distribution of large scale structures, and astrophysically (see, e.g., Ref. [21, 22]), with scalar fields, among other things, being able to form astrophysically relevant structures either by collapsing [22–26] or as a result of the interaction with BHs [27–30] (in which a spectrum of quasi-bound states appears associated with scattering events and the superradiant mechanism). Our focus will be on the astrophysical effects of the scalar-field structures.

1.2 Scalar-field structures

We will focus on two types of scalar-field structures: self-gravitating structures, particularly, boson stars and oscillatons, and BH's quasi-bound states of scalar-fields.

Self-gravitating solutions

The first solution of an astrophysical, self-gravitating, scalar-field structure was obtained by Kaup in 1968 [31]. Using a massive complex scalar field minimally coupled to gravity, a spherically-symmetric solution to the Einstein-Klein-Gordon system of equations was found numerically and it was first named *Klein-Gordon geon*. The following year, Ruffini and Bonazzola [32] studied a quantised real scalar field and used as source of the Einstein equations the expectation value of the energy momentum tensor in a configuration where N bosons occupy the lowest energy state. Calculating the energy-momentum in this way matches the energy-momentum obtained by Kaup with a massive complex scalar field, giving rise to the same results. This means that the classical treatment of the system can be used to derive its most important characteristics. Up until the 1980s there was not much interest in this topic, but then a set of new works dealing with scalar fields in gravitational context appeared (see, e.g., [33–35]). During that period, several terms were used to refer to these rediscoved structures, particularly the term boson star (BS), which started to be used widely to describe these localized structures of scalar fields. The question of stability of these solutions is a topic that has attracted much interest. The first studies were performed with a linear analysis [36–39] concluding that excited BS states are unstable and that ground states can be organized in a stable and an unstable branch, whose division is set by the maximum mass configuration of the BS solutions (see Fig. 2.5). The understanding of the unstable ground state solutions was investigated in later, full numerical studies that evolved the Einstein-Klein-Gordon equations [40–42] and it was concluded that they can collapse to BHs, disperse to infinity or transition to the stable branch.

In 1992, Seidel and Suen [43] found solutions of a real scalar field coupled to gravity, which became known as oscillatons. Derrick's theorem [44] state that it is not possible to find a classical time-independent stable solution of a real scalar field in flat spacetime. Kaup avoided this theorem by considering a complex field, and Seidel and Suen did it by considering a time-dependent real scalar field. Considering that the field can be written as a sum of sinusoidal functions oscillating with frequencies that are multiple of a fundamental one they were able to construct solutions of the Einstein-Klein-Gordon system. The dynamics and stability of oscillatons were studied in Refs. [45, 46], where a set of quasi-stable ground states were found (excited states are unstable, similarly to the BS case). These solutions are quasi-stable because they have a small radiating tail [47–49], but the mass-loss rate is for much of the parameter space larger than a Hubble time.

The formation of BSs and oscillatons happens by the so called "gravitational cooling process" [50–52], by which a generic bosonic cloud would gravitationally cool to a BS or Oscillaton by ejecting, through scalar radiation, parts of its total scalar matter.

These solutions (either BSs or oscillatons) can be studied in a Newtonian limit [40, 53, 54]. When the magnitude of the scalar field is very small, the solutions of the Einstein-Klein-Gordon system have extremely large spatial extent and the underlying spacetime geometry is very close to Minkowski. It was shown that to study this regime, it is sufficient to work with the simpler Schrodinger-Poisson (SP) system instead of the Einstein-Klein-Gordon one. Moreover, the SP system describes the dynamics of both complex and real scalar fields [51] in the low-energy limit.

BH quasi bound states

In the previous case of the self-gravitating structures, the underlying metric has an umbilical relation with the scalar field solution. Other scenarios in which scalar fields may participate are not so intricate, specifically the case in which the background metric, on top of which the scalar field is analysed, is fixed and insensitive to the scalar-field backreactions. In this case, one considers that the metric is a vacuum solution of the Einstein equations – meaning that the energy momentum tensor due to the scalar field is negligible – and the Klein-Gordon equation is solved with this solution as a background.

The massive KG equation in the Kerr background is hard to solve and the spectrum of bound states has been found in the regimes $M\mu = r_g/\lambda_C \gg 1$ [27] and $M\mu = r_g/\lambda_C \ll 1$ [28] where r_g and λ_C are the gravitational radius of the BH and λ_C is the Compton wavelength of the scalar field. Later, this spectrum was also studied numerically [29, 30] and both methods agreed in the corresponding regimes. The most relevant result of these studies is that some elements of the massive KG spectrum present a positive imaginary part. These elements correspond to quasi-bound states that can, by extracting rotational energy from the BH through a process known as superradiance [55], avoid complete absorption by the BH's horizon. Thus, massive real scalar fields around BHs can lead to very long-lived—for all purposes stationary—configurations [56–59], while complex fields may form truly stationary configurations [60–63]. Furthermore, numerical studies have shown (see, e.g., Refs. [56, 57, 64]) that BHs may support scalar field structures that resulted from a scattering event. In this scenario, a scalar wave meets a BH and part of it gets trapped in its quasi-bound state structure.

1.3 Astrophysical effects of scalar fields

Although predicted to be small, some works have explored the coupling between these ultra-light scalar fields and the photon in an astrophysical setting. By considering that scalar clouds around a BH may emit electromagnetic radiation, Refs. [65–67] have calculated specific signatures for those systems.

One the most seductive scenarios, particularly after the first successful gravitational wave detection [68], is the collision of two BSs and its gravitational wave output; Refs. [69–71] study such event either in the case of head-on collisions or in the case of an inspiralling binary. Other works tackle a slightly different scenario, in which it is considered an inspiraling binary with one of the elements being a BS; some examples are Ref. [72, 73], in which an Extreme Mass Ratio Inspiral (EMRI) composed of a SMBH and a BS is investigated in order to extract distinctive features out of the GW signal. In other works the coexistence of fermions and bosons in the same astrophysical structure is studied. In Ref. [74], the possibility of light bosons affecting the equation of state of neutron stars is considered: constrains on the couplings to the SM particles are obtained. The possibility of bosonic particles being accreted by fermionic stars is the theoretical backbone of studies of fermion-boson stars – which are evolved and quasi-normal modes (QNM) are calculated in Ref. [75]. In Ref. [76, 77] stable configurations of systems containing bosons and fermions are constructed, taking to a next level a long tradition in the literature (e.g., Refs. [78–81]) and obtaining yet another theoretical argument in favour of the possibility of stars accreting bosonic particles in their interior.

Given the weak coupling of these light scalar fields to matter, the astrophysically-sized structures composed exclusively by these particles are expected to interact with other celestial bodies only through their gravitational influence. This means that if these objects exist they may, at least in a first approach, mimic BHs. A great effort has been made to find conclusive tests to distinguish these structures from BHs: in Ref. [82], the authors investigate the possibility of distinguishing between rotating BHs and BSs just by looking at the images of accreting tori around them; in Ref. [83] the response of a BS to the accretion of supersonic winds is compared to the one of a BH of the same mass; in Ref. [84] the spectral lines profile of an Extremely Compact Object (which can be a BS) are calculated and compared to those of a BH. In Ref. [85] accretion disks are studied around BSs and in Ref. [86], the gravitational redshift of those structures is calculated. Ref. [87] calculates the QNMs of BSs and in Ref. [88] their tidal deformability is studied; in Ref. [89] the authors study the shadow of BSs and the evolution under perturbations. One of the most important aspects that distinguishes BHs and BSs is the fact that the latter do not contain an event horizon, which means that particles and light will be able to reach its center. So, the study of orbits in the spacetimes generated by BSs [90–99] as well as their gravitational lensing effects [100, 101] assume particular importance.

The limit in which the BSs and oscillatons can be studied using the Schrodinger-Poisson system, i.e., the weak-field, Newtonian limit is typically considered in galactic scenarios with the weak-field BS being considered as a Dark Matter clump, a very seductive scenario given the ability of BSs in this limit to solve some of the problems of the Cold Dark Matter (CDM) paradigm [15, 102, 103]. This line of research has been used to constrain the value of the mass of the scalar field: using rotation curve measurements [104] and pulsar timing measurements [105–107]. In Ref. [108], the authors use measurements of the environment in the center of galaxies to constrain the scenario in which a scalar-field structure describes the DM content in that region.

BH quasi-bound states are also fertile sources of phenomenology. In Refs. [109, 110] the gravitational wave output due to the presence of a real scalar-field cloud around a BH is calculated. In Refs. [111, 112], the authors calculate the shadows of BHs with scalar hair, i.e., they extract the effect of the scalar-field structure on the way the light coming from behind the system is distorted. Observations of other effects typically associated with the presence of BHs can be scrutinized for the presence of scalar fields: in Ref. [113] the authors study how the quasi-periodic oscillations observed in the X-ray flux observed in accreting compact objects distinguish between Kerr BHs and BHs with bosonic hair; in Ref. [114] the iron Kα line of the reflection spectrum of BHs with scalar hair and BHs without hair is used as a way of distinguishing between the two structures; in Ref. [115] the authors consider BH binaries in which one of the BHs supports a scalar cloud and study the effects the presence of this cloud has on the GW signal of the binary.

1.4 Structure of the document

In this document, we present a set of results to be added to this vast body of work. In Chapter 2 we will introduce all concepts that are used in the rest of the document: the Einstein-Klein-Gordon equations underpin everything. Both BSs, oscillatons and scalar clouds around BHs are solutions of that system of equations. We make a brief characterization of each of these solutions and highlight the relevant aspects for the understanding of the other sections.

In Chapter 3 we generically focus on the Extreme-Mass-Ratio-Inspiral (EMRI) scenario which is a binary of two massive bodies, one with a mass much bigger than the other, in which the latter inspirals (due to the emission of gravitational radiation) into the former. These systems are long lived and are one of the main targets of the next generation of GW wave detectors. If the more massive component of this binary harbours a real scalar field cloud, then, we argue, orbital resonances develop and may affect the movement of the lighter component of the EMRI as it inspirals into the more massive one.

In Chapter 4 we bring the possibility of the development of a scalar field cloud around a BH to a more specific stage: the center of the Milky Way. Considering that the center of the galaxy is occupied by a BH around which a complex scalar field cloud has developed, we calculate how the cloud affects the variation of the orbital elements of the S2-star, one of the stars that are monitored as they orbit that central massive object. We obtain that, even with very conservative assumptions, the presence of such a scalar cloud can leave a measurable imprint on the variation of the orbital elements of the aforementioned star.

Finally, in Chapter 5 we focus on low-energy, self-gravitating scalar field structures. In this regime, such structures are stable and we explore their reaction to the presence of an orbiting, point-like particle. The scalar field is tidally deformed and that deformation affects the whole system: on the one hand, the scalar-field structure develops long-lived rotating overdensities and, on the other hand, the point-like particle, as it traverses the scalar-field structure, experiences a gravitational friction force.

In what follows, and unless otherwise stated, Planck units are used ($G = c = \hbar = 1$).

Chapter 2

Framework

In this chapter, we present the theoretical foundations of the rest of the document and we set notation. In Section 2.1 we discuss quasi-bound states of scalar fields in the presence of BHs, with special attention to the case in which the Compton wavelength of the scalar field is bigger than the gravitational radius of the BH. In Section 2.2 we introduce the concept of self-gravitating bound states of scalar fields. We focus on spherically symmetric boson stars (BSs) and oscillatons; we describe how these structures are obtained from the Einstein-Klein-Gordon system and we characterize them.

2.1 Scalar fields in the presence of BHs

In the presence of BHs, scalar field quasi-bound states can be found. The fate of these bound-states will depend on how the scalar-field modes are related to the superradiance condition.

2.1.1 Description of quasi-bound states

The Scalar-Field-BH system is governed by the action

$$S = \int d^4x\sqrt{-g}\left(\frac{R}{16\pi} - \frac{1}{2}g^{\alpha\beta}\Psi^*_{,\alpha}\Psi^*_{,\beta} - \frac{\mu^2}{2}\Psi\Psi^*\right), \tag{2.1}$$

in which R is the Ricci scalar, $g_{\alpha\beta}$ and g is the metric and its determinant, $\Psi(t, r, \theta, \phi)$ is a (complex or real) scalar field with mass $\mu = m_s$, Ψ^* indicates complex conjugation of the field and $\Psi_{,\alpha}$ indicates derivation with respect to the indexed coordinate. The study of the quasi-bound states is made with the assumption that the scalar-field contribution as a matter source is negligible. So, the Einstein equations are satisfied by a vacuum solution, in this case the Kerr metric,

$$
\begin{aligned}
ds^2 = &-\left(1-\frac{2Mr}{\rho^2}\right)dt^2 - \frac{4aMr\sin^2\theta}{\rho^2}dtd\phi + \frac{\rho^2}{\Delta}dr^2 + \rho^2 d\theta^2 + \\
&+\left[(r^2+a^2)\sin^2\theta + \frac{2Mr}{\rho^2}a^2\sin^4\theta\right]d\phi^2,
\end{aligned} \tag{2.2}
$$

where

$$
\Delta = r^2 - 2Mr + a^2 \quad \text{and} \quad \rho^2 = r^2 + a^2\cos^2\theta, \tag{2.3}
$$

in which M is the BH mass, $a = J/M$ is the rotation rate of the BH and (t, r, θ, ϕ) are the Boyer-Lindquist coordinates. The Kerr metric is held fixed and the Klein-Gordon (KG) equation

$$
g^{\mu\nu}\nabla_\mu\nabla_\nu\Psi = \mu^2\Psi, \tag{2.4}
$$

where ∇_μ represents the covariant derivative, is solved in this background. This equation admits separable solutions [116, 117] of the form

$$
\Psi = \mathrm{e}^{-\mathrm{i}\omega t + \mathrm{i}m\phi} S_{\ell m}(\theta)\psi_{\ell m}(r), \tag{2.5}
$$

in the case of a complex scalar field (the real scalar field case can be obtained by isolating the real part of the previous expression), where ω is the mode frequency of the scalar field and ℓ and m are angular indices. Substituting in the KG equation, one obtains two Ordinary Differential Equations (ODEs) for the radial and angular parts of each frequency mode of the scalar field

$$
\frac{d}{dr}\left(\Delta\frac{d\psi_{\ell m}}{dr}\right) + \left[\frac{\omega^2(r^2+a^2)^2 - Mam\omega r + m^2a^2}{\Delta} - (\omega^2a^2 + \mu^2r^2 + \Lambda_{\ell m})\right]\psi_{\ell m} = 0, \tag{2.6}
$$

and

$$
\frac{1}{\sin\theta}\frac{d}{d\theta}\left(\sin\theta\frac{dS_{\ell m}}{d\theta}\right) + \left[a^2(\omega^2-\mu^2)\cos^2\theta - \frac{m^2}{\sin^2\theta} + \Lambda_{\ell m}\right]S_{\ell m} = 0, \tag{2.7}
$$

where $\Lambda_{\ell m}$ is a separation constant. The angular equation has solutions given by the set of spheroidal harmonics [118] $S_{\ell m} = S_\ell^m(\cos\theta; c)$ where $c = a(\omega^2 - \mu^2)^{1/2}$, ℓ and m are integers. It is relevant that in the limit $c \to 0$ (i.e. when the frequency of the scalar field function is dominated by the rest mass of the scalar field) it is verified (see Ref. [62] and references therein)

$$S_\ell^m(\cos\theta; c) \to P_\ell^m(\cos\theta), \quad \Lambda_{\ell m} \to \ell(\ell+1), \tag{2.8}$$

where the P_ℓ^m are the associated Legendre polynomials.

The quasi-bound state solutions of the KG-equation satisfy two conditions: they are ingoing at the horizon and exponentially decaying at infinity. To obtain them, one has to enforce those conditions and to do it, it is convenient to rewrite the radial equation in terms of a coordinate that can penetrate the horizon such as the tortoise coordinate

$$\frac{dr_*}{dr} \equiv \frac{r^2+a^2}{\Delta}; \tag{2.9}$$

then, in terms of $U_{\ell m} = (r^2+a^2)^{1/2}\psi_{\ell m}$, the radial equation reads

$$\frac{d^2 U_{\ell m}}{dr_*^2} + [\omega^2 - V(r,\omega)]U_{\ell m} = 0, \tag{2.10}$$

where the potential $V(r,\omega)$ is written as

$$\begin{aligned} V(r,\omega) =& \frac{\mu^2\Delta}{r^2+a^2} + \frac{4am\omega Mr - a^2m^2 + \Delta[\Lambda_{\ell m} + (\omega^2-\mu^2)a^2]}{(r^2+a^2)^2} + \\ &+ \frac{\Delta(2Mr^3 + a^2r^2 - 4Ma^2r + a^4)}{(r^2+a^2)^4}, \end{aligned} \tag{2.11}$$

and one verifies that

$$V(r,\omega) \sim \begin{cases} \mu^2 & \text{as } r \to \infty \quad (r_* \to \infty), \\ \omega^2 - (\omega - m\Omega_+)^2 & \text{as } r \to r_+ \quad (r_* \to -\infty), \end{cases} \tag{2.12}$$

where

$$r_+ = M + (M^2 - a^2)^{1/2}, \tag{2.13}$$

is the radial coordinate of the BH's event horizon, and

$$\Omega_+ = \frac{a}{r_+^2 + a^2}, \tag{2.14}$$

is its angular velocity. This means that the boundary behavior of the radial function is given by

$$\psi_{\ell m}(r) \sim \begin{cases} \frac{\mathrm{e}^{\pm \mathrm{i} k r_*}}{r} & \text{as } r \to \infty \quad (r_* \to \infty), \\ \mathrm{e}^{\pm \mathrm{i}(\omega - m\Omega_+) r_*} & \text{as } r \to r_+ \quad (r_* \to -\infty), \end{cases} \tag{2.15}$$

with $k = (\omega^2 - \mu^2)^{1/2}$. To select the bound-state solutions we have to impose that at the horizon it behaves as an ingoing wave, which can be guaranteed by choosing a negative group velocity for the solution, i.e., we shall have

$$\mathrm{e}^{-\mathrm{i}(\omega - m\Omega_+) r*} \text{ as } r \to r_+ \quad (r_* \to -\infty), \tag{2.16}$$

and at infinity the solution should represent outgoing waves only, which means we have to choose positive group velocity only, i.e.,

$$\frac{\mathrm{e}^{+\mathrm{i} k r_*}}{r} \text{ as } r \to \infty \quad (r_* \to \infty). \tag{2.17}$$

Moreover, writing $k = \mathrm{i}\sqrt{\mu^2 - \omega^2}$, one sees that whenever $\omega^2 < \mu^2$, the solution tends to zero at infinity. In general, the frequency of the scalar field mode, ω, has a real and an imaginary part, i.e.

$$\omega = \omega_R + \mathrm{i}\omega_I, \tag{2.18}$$

but considering that $|\omega_I| \ll |\omega_R|$ (see, e.g., Refs. [27, 30]), the exponential decay at infinity decreed by the condition $\omega^2 < \mu^2$ implies that

$$\omega_R^2 < \mu^2. \tag{2.19}$$

Superradiant instability

Using the general expression for the frequency (Eq. (2.18)) we can see that the time-dependence of the scalar field (see Eq. 2.5) reads, explicitly

$$\mathrm{e}^{-\mathrm{i}\omega t} = \mathrm{e}^{-\mathrm{i}\omega_R t}\mathrm{e}^{\omega_I t}, \tag{2.20}$$

which means that the real part, ω_R, will set the oscillation frequency of the field mode whereas the imaginary part, ω_I, will set its growth or decay rate, for positve or negative values, respectively.

Numerical studies of these bound states show that (see, e.g., Ref. [30]) the values of the frequencies can be organized in the following way

(i) $\omega_I < 0$ for $\omega_R > m\Omega_+$,

(ii) $\omega_I > 0$ for $\omega_R < m\Omega_+$,

(iii) $\omega_I = 0$ for $\omega = m\Omega_+$,

where m is an integer associated with the angular mode (see Eqs. (2.7) and (2.15)). For the first case, the solutions decay with time, for the second case – which is called the superradiant case [55] – the solution grows with time, being able to extract energy from the BH that harbours it; the third case corresponds to a situation in which there is no growth or decay – in the case of a complex field, the resulting energy density is stationary [60, 62].

2.1.2 Small coupling approximation

Although these solutions are typically obtained using numerical methods (for details on the numerical construction of the quasi bound states check, for instance, Appendix A of Ref. [109]) if the scalar field has a Compton wavelength λ_C that is larger than the gravitational radius of the BH, i.e.

$$\alpha = r_g\mu = \frac{GM}{c^2}\frac{m_s c}{\hbar} = M\mu \ll 1, \quad \lambda_C = \frac{1}{\mu}, \tag{2.21}$$

then it is possible to find analytical solutions. The method to find these solutions was originally presented in Ref. [28]. In this limit, the angular functions are given by the associated Legendre polynomials

$$S_\ell^m \to P_\ell^m(\cos\theta), \tag{2.22}$$

and the radial function is given by

$$\psi_{\ell n}(r) = A_{\ell n}\tilde{r}^\ell \mathrm{e}^{-\tilde{r}/2} L_n^{2\ell+1}, \tag{2.23}$$

where $L_n^{2\ell+1}$ represent the Laguerre polynomials, n is the overtone number and the radial coordinate is normalized as

$$\tilde{r} = \frac{2rM\mu^2}{\ell+n+1}. \tag{2.24}$$

The frequency of the scalar field is complex and it is given by [28]

$$\begin{cases} \omega_R & \sim \mu - \mu \left(\frac{M\mu}{\ell+n+1}\right)^2 \\ \omega_I & \sim \mu \left(\frac{am}{M} - 2\mu r_+\right) \frac{\alpha^{4\ell+4}}{\sigma_\ell} \end{cases}, \tag{2.25}$$

where σ_ℓ is a parameter that depends on the angular indices (ℓ, m); for the dominant unstable mode, $\ell = 1$, it is obtained that $\sigma_1 = 48$ [110]. The fact that the frequency has an imaginary component, means that for certain modes, the profile of the scalar field will grow with time. The field mode that will grow more efficiently due to the superradiant mechanism is the $n = 0, \ell = m = 1$ mode [30, 110] for which the scalar field function can then be written as

$$\Psi = \left[A_{10}\mathrm{e}^{\omega_I t}\right] \mathrm{e}^{-\mathrm{i}(\omega_R t - \phi)} r(M\mu^2) \mathrm{e}^{-\frac{r(M\mu^2)}{2}} \sin\theta. \tag{2.26}$$

where A_{10} is a constant to be fixed later. One can normalize the coordinates in terms of the BH mass by applying the substitution

$$\begin{cases} r \to r/M, \\ t \to t/M, \end{cases} \tag{2.27}$$

such that the scalar-field function is written as

$$\Psi = \left[A_{10}\mathrm{e}^{\omega_I t}\right] \mathrm{e}^{-\mathrm{i}(\omega_R t - \phi)} r\alpha^2 \mathrm{e}^{-\frac{r\alpha^2}{2}} \sin\theta, \tag{2.28}$$

making the dependence on the mass coupling parameter, $\alpha = M\mu$, explicit. Notice also that with the normalized coordinates, the frequencies are measured in units of M^{-1} meaning that we can write

$$\begin{cases} \omega_R & \sim M\mu - (M\mu)\left(\frac{M\mu}{\ell+n+1}\right)^2, \\ \omega_I & \sim \left(\frac{a}{M}m - 2M\mu r_+\right) \frac{(M\mu)^{4\ell+5}}{\sigma_\ell}. \end{cases} \tag{2.29}$$

The real part of the frequency, which determines the oscillation of the scalar field, is very close to the value of the mass of the scalar field function and the value of the imaginary part of the frequency is much smaller than the real component. This result agrees with the choice expressed in Eq. (2.22) for the angular momentum function where it was assumed that $\omega^2 \sim \mu^2$.

2.1.3 Complex and real fields

In the rest of the document we will be using complex and real scalar fields. We have used the complex scalar field case

$$\Psi = \left[A_{10}\mathrm{e}^{\omega_I t}\right] \mathrm{e}^{-\mathrm{i}(\omega_R t-\phi)} r\alpha^2 \mathrm{e}^{-\frac{r\alpha^2}{2}} \sin\theta, \tag{2.30}$$

to make all the derivations. To obtain the real scalar field solution, we simply consider the real part of the complex one (see, for instance, Ref. [109, 110])

$$\mathrm{Re}[\Psi] = \left[A_{10}\mathrm{e}^{\omega_I t}\right] \cos(\omega_R t-\phi) r\alpha^2 \mathrm{e}^{-\frac{r\alpha^2}{2}} \sin\theta \tag{2.31}$$

So far, we explicitly wrote the exponential factor, $\mathrm{e}^{\omega_I t}$, that describes the growth of the scalar field function. From now on, and given that $\omega_I \ll \omega_R$, we will absorb it in the normalization constant that multiplies the scalar field function, i.e., we will write

$$A_0 \equiv A_{10}\mathrm{e}^{\omega_I t}. \tag{2.32}$$

By doing this we are making the reasonable assumption that one can separate the growing scale (associated with ω_I) from the oscillating scale (associated with ω_R), meaning that the growing dynamics of the scalar field structure can be ignored. This situation corresponds to a scenario in which we have a scalar field with a given profile for a long enough time that it can be considered constant. This will be translated in the value of the constant A_0 which is related to the total mass of the scalar cloud.

2.1.4 The peak of the scalar field cloud

One of the ways to characterize these bound-state solutions is by the maximum value of their radial distribution. This quantity is related to the mass coupling parameter as

$$R_{\text{peak}} \sim \frac{1}{\alpha^2}. \tag{2.33}$$

This means that the smaller the mass coupling parameter (i.e., the bigger the difference between the Compton wavelength of the scalar field and the gravitational radius of the BH) the farther is the peak of the cloud from the BH. From Fig. 2.1 one can also see that as the peak of the scalar

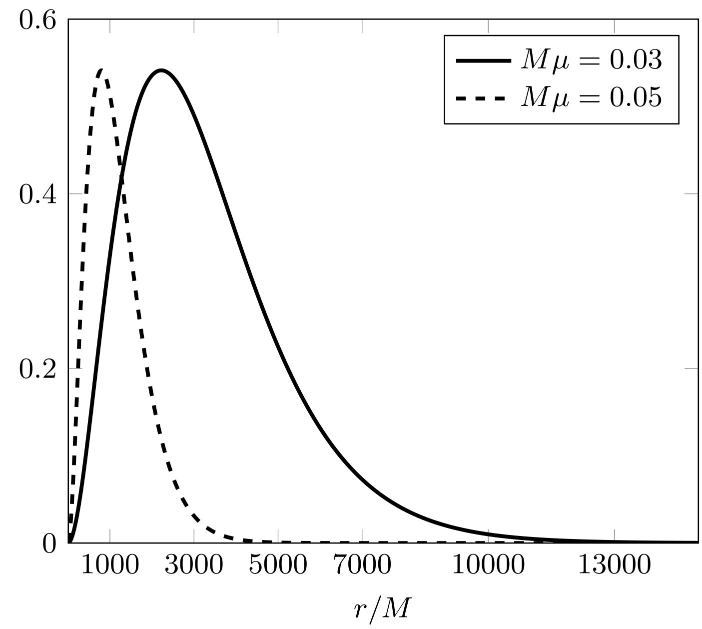

Figure 2.1: Comparing the radial profile of the quasi-bound state density function ($\Psi\Psi^*/\sin^2\theta A_0^2$) (see Eq. (2.30)) for two different values of the mass coupling parameter. We observe that the smaller the mass coupling parameter, the farther the peak is located from the BH's horizon. Moreover, decreasing the mass coupling parameter also causes the scalar cloud to become more extended.

field density gets farther from the BH, the width of the whole distribution increases too. This means that for a fixed BH mass M, lighter fields give rise to more extended bound states.

2.1.5 Effective gravitational effect of the scalar field clouds

The bound-state solutions we are analysing are constructed under the condition that $\alpha \ll 1$ and this condition implies, taking into account the position of the peak of the cloud, that

$$r_g \ll R_{\text{peak}}, \tag{2.34}$$

where r_g is the gravitational radius of the BH. In other words, the bound-state solutions of the KG equation in the small mass coupling limit concentrate most of their influence very far from the BH.

Far from the BH the spacetime is approximately flat. So, we can describe the gravitational influence of the scalar-field cloud as if its energy density sources a small spacetime deviation from a flat metric, i.e., as if the metric in the region where the scalar field cloud peaks can effectively be written as

$$ds^2 = (-1 + 2U)dt^2 + (1 + 2V)dr^2 + r^2 d\Omega^2, \tag{2.35}$$

where U and V are functions of the radial coordinate only. The corresponding Newtonian gravitational potential, U_N, corresponds to the function U. Following Appendix A, we obtain that in the case of a complex scalar field, the leading order of the Einstein equations correspond to

$$U = V, \quad \nabla^2 U = -4\pi\mu^2 |\Psi|^2 , \tag{2.36}$$

whereas if the scalar field is real, one verifies that

$$\begin{cases} \nabla^2(U - V) = 12\pi\frac{\mu^2}{2}[A_0 g(r)\sin\theta]^2 \cos(2(\omega t + \phi)), \\ \nabla^2 V = -4\pi\frac{\mu^2}{2}[A_0 g(r)\sin\theta]^2, \end{cases} \tag{2.37}$$

where $g(r) = \alpha^2 r \exp(-\alpha^2 r/2)$. From this analysis, we see that a real scalar field gives rise to a time dependent, Newtonian-like potential; this is because its pressure is of the same order of its energy density (see other accounts of this fact in Ref. [51, 54, 106]). The complex scalar field case is simpler: because it gives rise to a static energy-momentum tensor, its effective, Newtonian-like potential will also be static.

2.1.6 Mass of the scalar clouds

To calculate the total mass of the scalar field clouds, we will take advantage of the fact that their profiles are mainly concentrated in regions that are mostly flat, i.e. far from the BH which harbours them. This allows us to consider that their effective gravitational influence can be described by their energy-momentum tensor written in a flat background

$$T^{\mu\nu} = \Psi^{*,(\mu}\Psi^{,\nu)} - \frac{1}{2}\eta^{\mu\nu}\left(\Psi^*_{,\alpha}\Psi^{,\alpha} + \mu^2\Psi^*\Psi\right), \tag{2.38}$$

where $\eta_{\mu\nu}$ is the Minkowski metric. Moreover, by considering the functional form of the scalar field under analysis (Eqs. (2.30) and (2.31)) and their frequency (Eq. (2.25)), one can consistently argue that the dominant term of the 00 component of the energy-momentum tensor (which describes the energy density of the scalar field) is given by (see Appendix A)

$$\rho = T_{00} \sim \mu^2 |\Psi|^2. \tag{2.39}$$

Taking this into account, one can calculate the total mass of the scalar cloud by computing

$$M_{SC} = \int \rho_{r,c} r^2 \sin\theta \mathrm{d}r \mathrm{d}\theta \mathrm{d}\phi, \tag{2.40}$$

where $\rho_{r,c}$ is the the density function and can be written as

$$\begin{cases} \rho_c = \mu^2 A_C^2 \mathrm{e}^{-r\alpha^2} r^2 \alpha^4 \sin^2\theta, \\ \rho_r = \frac{\mu^2}{2} A_R^2 \mathrm{e}^{-r\alpha^2} r^2 \alpha^4 \sin^2\theta, \end{cases} \tag{2.41}$$

where ρ_c, A_C and ρ_r, A_R correspond to the value of the energy density and amplitude of the field profile for the complex and real scalar field case, respectively.

Since the expressions for the energy density of the scalar field cloud are written in terms of the normalized coordinates (Eq. (2.27)), the integration over the whole space should take that into account, by rescalling also the integration variables. Performing this rescalling we will end up with the following expressions for the value of the mass of the scalar cloud

$$M_{SC} = \begin{cases} M\alpha^2 A_C^2 \int \mathrm{e}^{-r\alpha^2} r^2 \alpha^4 \sin^2\theta r^2 \sin\theta \mathrm{d}r \mathrm{d}\theta \mathrm{d}\phi, \\ \frac{M}{2}\alpha^2 A_R^2 \int \mathrm{e}^{-r\alpha^2} r^2 \alpha^4 \sin^2\theta r^2 \sin\theta \mathrm{d}r \mathrm{d}\theta \mathrm{d}\phi, \end{cases} \tag{2.42}$$

where M is the mass of the BH. Simplifying these expressions, we obtain that

$$M_{SC} = \begin{cases} M\frac{64\pi A_C^2}{\alpha^4}, \\ M\frac{32\pi A_R^2}{\alpha^4}. \end{cases} \tag{2.43}$$

One can then conclude that the amplitude of the scalar field function and the mass of the scalar cloud are related by

$$\begin{cases} A_C^2 = \left[\frac{M_{SC}}{M}\right] \frac{\alpha^4}{64\pi}, \\ A_R^2 = \left[\frac{M_{SC}}{M}\right] \frac{\alpha^4}{32\pi}. \end{cases} \tag{2.44}$$

2.2 Self-gravitating bound states

So far, we focused in solutions of the Klein-Gordon equation in which the background metric is fixed. This is a good description of a situation in which the scalar field is a subdominant term. In this section, we drop the latter assumption, such that the scalar field is considered to be the main source of spacetime curvature. This means that, instead of working with the KG-equation only, we will work with the Einstein-Klein-Gordon system

$$\begin{cases} R_{\alpha\beta} - \frac{R}{2} g_{\alpha\beta} = 8\pi T_{\alpha\beta}, \\ \nabla_\alpha \nabla^\alpha \Psi = \mu^2 \Psi, \end{cases} \tag{2.45}$$

where ∇_α is the covariant derivative, $R_{\alpha\beta}$ and R are the Ricci's tensor and scalar, respectively and $T_{\alpha\beta}$ is the energy-momentum tensor of the scalar field Ψ with mass $m_s = \mu\hbar/c$.

2.2.1 Spherically symmetric solutions of the EKG system

The spherically symmetric solutions of the Einstein-Klein-Gordon system are the simplest ones. In this case the metric is given by the generic form

$$ds^2 = -A(t,r)dt^2 + B(t,r)dr^2 + r^2 d\Omega^2, \tag{2.46}$$

where one is allowing for the possibility of time-varying metric coefficients and where $d\Omega$ is the solid angle element given by

$$d\Omega = d\theta + \sin^2\theta d\phi. \tag{2.47}$$

We are interested in self-gravitating bound states of the EKG system; considering a generic situation in which the scalar field is given by a separable function

$$\Psi(t,r) = H(t)\psi(r), \tag{2.48}$$

and assuming that there is not an event horizon in the respective spacetime, the bound state solutions must be regular at the origin and decay exponentially at infinity. The latter condition is realized if the frequency of the scalar field is real and always smaller than the rest mass of the

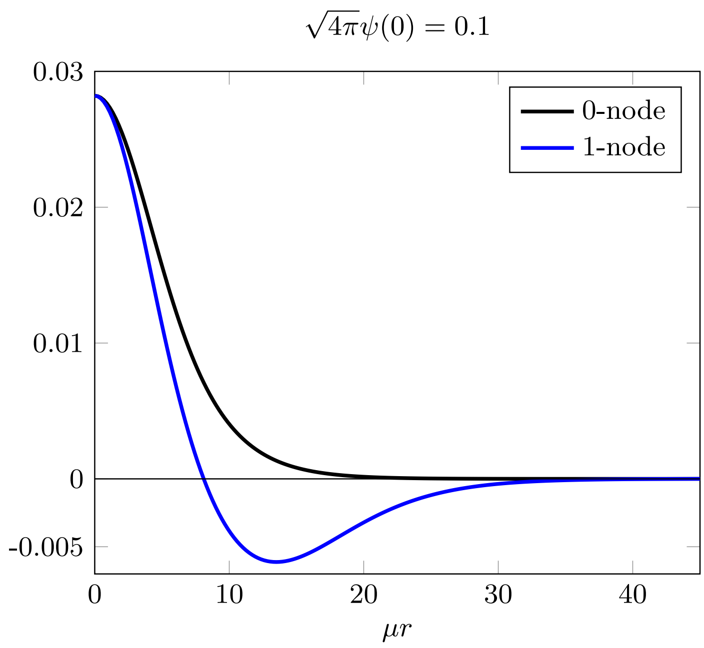

Figure 2.2: Radial profiles of two boson star solutions, both with $\psi(0)\sqrt{4\pi} = 0.1$. One with 0-nodes (a ground state) and another with 1-node (an excited state).

scalar field, i.e.,

$$\omega < \mu. \tag{2.49}$$

This must be verified because, in the limit $r \to \infty$, the Klein-Gordon equation reduces to its flat-spacetime version

$$\psi''(r) + \frac{2\psi'(r)}{r} + \left(\omega^2 - \mu^2\right)\psi(r) = 0, \tag{2.50}$$

where it was used that $H \sim \exp(-\mathrm{i}\omega t)$ and the prime indicates derivation with respect to the radial coordinate; the decaying solution for this equation (which is the one we are interested in) is

$$\psi(r) = \frac{\exp(-\sqrt{\mu^2 - \omega^2}r)}{r}, \tag{2.51}$$

for which one must verify that $\mu^2 - \omega^2 > 0$. The frequency of the scalar field solutions has a central importance and is used to characterize them. This characterizing value comes from the temporal part of the scalar field function. From its spatial part comes another characteristic, which is the number of nodes. The existence of nodes (see Fig. 2.2) in a scalar-field solution is an indication that the solution is unstable [36–39], whereas the ones without nodes – called ground state solutions – have a stable and an unstable branch. In what follows we will only deal with ground state solutions.

Boson stars

For the case in which the scalar field is complex, one writes (see Refs. [31, 32])

$$\Psi = \exp(-\mathrm{i}\omega t)\psi(r), \tag{2.52}$$

where ω is the frequency of the scalar field and $\psi(r)$ is the radial profile of the scalar field. In calculating the energy-momentum tensor of the complex scalar field,

$$T^{\alpha\beta} = \Psi^{*,(\alpha}\Psi^{,\beta)} - \frac{1}{2}g^{\alpha\beta}\left(\Psi^{*}_{,\sigma}\Psi^{,\sigma} + \mu^2\Psi^{*}\Psi\right), \tag{2.53}$$

the terms depending on the field will be independent of the time coordinate. By dropping the time-dependence of the metric tensor

$$ds^2 = -A(r)dt^2 + B(r)dr^2 + r^2 d\Omega^2, \tag{2.54}$$

substituting Eq. (2.54) and Eq. (2.52) in the Einstein-Klein-Gordon system of Eq. (2.45) and performing a scalling of variables

$$\omega \to \omega/\mu, \quad t \to \mu t, \quad r \to \mu r, \quad \psi \to \frac{\psi}{\sqrt{4\pi}}, \tag{2.55}$$

one obtains a coupled system of equations for all the relevant quantities of the problem

$$\frac{A(r)\left(rB'(r) + B(r)^2 - B(r)\right)}{r^2 B(r)^2} = \frac{A(r)\psi'(r)^2}{B(r)} + \psi(r)^2\left(A(r) + \omega^2\right), \tag{2.56}$$

$$B(r)\left(\frac{r\psi(r)^2\left(\omega^2 - A(r)\right)}{A(r)} + \frac{1}{r}\right) + r\psi'(r)^2 = \frac{A'(r)}{A(r)} + \frac{1}{r}, \tag{2.57}$$

$$\psi'(r)\left(-\frac{A'(r)}{A(r)} + \frac{B'(r)}{B(r)} - \frac{4}{r}\right) = 2\left(\frac{B(r)\psi(r)\left(\omega^2 - A(r)\right)}{A(r)} + \psi''(r)\right). \tag{2.58}$$

This coupled set of ODEs is solved using the shooting method where one of the free parameters is the frequency ω of the scalar field. The solutions obey two conditions: (a) the regularity of the system, which means that at the origin one fixes

$$A'(0) = B'(0) = \psi'(0) = 0, \tag{2.59}$$

and (b) finiteness of the scalar field solution, which means that at infinity, the scalar-field function must behave according to

$$\lim_{r\to\infty} \psi(r) = 0. \tag{2.60}$$

These conditions are not enough to solve the coupled system of ODEs. An inspection of the equations of motion close to the origin shows that the condition

$$B(0) = 1, \tag{2.61}$$

is automatically satisfied for a regular and finite solution of the system, while at infinity, it is verified that

$$\lim_{r\to\infty} B(r) = 1, \tag{2.62}$$

under the same conditions. The value of the scalar field and of the metric component $A(r)$ at the origin are left free, i.e.

$$A(0) = A_0, \quad \psi(0) = \psi_0. \tag{2.63}$$

We have three free parameters – the frequency ω and the values at the origin of $\psi(r)$ and $A(r)$ – and two shooting conditions, namely, the finiteness of the scalar field function and asymptotic flatness of the metric

$$\lim_{r\to\infty} \psi(r) = 0, \text{ and } \lim_{r\to\infty} A(r) = 1. \tag{2.64}$$

One of the free parameters can be chosen by us and it will be the central value of the scalar field function, ψ_0. Then the shooting method will determine ω and A_0.

Following this method, we obtain stable (i.e. 0-node) boson star solutions that will be further characterized by the value of the scalar field function at the origin and by the corresponding values for the frequency and the value of the metric function at the origin – $A(0)$. In Fig. 2.3 it is plotted one profile of a 0-node complex scalar field function and in Fig. 2.4 the relation between the central value of the profile of 0-node scalar-field solutions and their frequency. Notice that there is a minimum value for the frequency of the scalar field and that the solutions are divided in a stable and unstable branch.

Oscillatons

If instead of a complex scalar field one considers a real one, the corresponding energy-momentum tensor will have a time-dependence. This means that we have to consider time-dependent metric functions. From now on, and for numerical convenience, we will be writing the spherically symmetric metric as

$$ds^2 = -A(t,r)dt^2 + B(t,r)dr^2 + r^2 d\Omega^2 = -B(t,r)\left(\frac{1}{C(t,r)}dt^2 + dr^2\right) + r^2 d\Omega^2. \quad (2.65)$$

Using this metric and a generic real scalar field function $\Psi(t,r)$ in the Einstein-Klein-Gordon system of Eq. (2.45) and rescalling the variables as in Eq. (2.55) one isolates the following set of equations

$$-\frac{B'}{rB} + B\left(\Psi^2 - \frac{1}{r^2}\right) + C\dot{\Psi}^2 + \Psi'^2 + \frac{1}{r^2} = 0, \quad (2.66)$$

$$2\Psi'\dot{\Psi} - \frac{\dot{B}}{rB} = 0, \quad (2.67)$$

$$\frac{B'}{B} + B\left(r\Psi^2 - \frac{1}{r}\right) + \frac{1}{r} = \frac{C'}{C} + rC\dot{\Psi}^2 + r\Psi'^2, \quad (2.68)$$

$$2rBC\Psi + rC'\Psi' + C\left(r\dot{C}\dot{\Psi} - 4\Psi' - 2r\Psi''\right) + 2rC^2\ddot{\Psi} = 0, \quad (2.69)$$

where the dot means time derivative and the prime means radial derivative. To obtain oscillaton solutions of this system, one considers that both the metric functions as well as the scalar field can be written as

$$B(t,r) = \sum_{j=0}^{\infty} B_{2j}(r)\cos(2j\omega t), \quad (2.70)$$

$$C(t,r) = \sum_{j=0}^{\infty} C_{2j}(r)\cos(2j\omega t), \quad (2.71)$$

$$\Psi(t,r) = \sum_{j=0}^{\infty} \psi_{2j+1}(r)\cos([2j+1]\omega t). \quad (2.72)$$

We follow the original work – Ref.[43] – in restricting the expansion of the metric functions to even component of the cosine expansion and the scalar-field expansion to odd ones. (See also Ref. [45, 54])

To the best of our knowledge there is not a solution that encompasses all the orders of the expansion; the accepted usage is the truncation of the expansion for a maximum value of $j = j_{max}$. Ref. [43] studies the convergence of the series as a function of j_{max} and obtains solutions of the system obeying the desired boundary conditions that converge rapidly, i.e., for small values of j_{max} – this justifies the truncation procedure. In any case, the value of j_{max} influences the accuracy of the solution obtained; for most cases $j_{max} = 1$ is accurate at a $\sim 1\%$ level. That is the value we are going to use in our construction

$$B(t,r) = B_0(r) + B_2(r)\cos(2\omega t), \tag{2.73}$$

$$C(t,r) = C_0(r) + C_2(r)\cos(2\omega t), \tag{2.74}$$

$$\Psi(t,r) = \psi_1(r)\cos(\omega t) + \psi_3(r)\cos(3\omega t). \tag{2.75}$$

In order to determine the components of the harmonic expansion, we substitute Eqs. (2.73), (2.74) and (2.75) in Eqs. (2.66), (2.67), (2.68) and (2.69), such that each equation is written has a harmonic sum; out of these harmonic sums, we force the coefficients of the terms $\cos(2j\omega t)$ and $\cos((2j+1)\omega t)$ with j up to $j_{max} = 1$ to be zero and out of that we obtain six ODEs for the variables $B_0, B_2, C_0, C_2, \Psi_1, \Psi_3$. These equations are solved numerically using the shooting method. As in the case of boson stars, we have to impose regularity at the origin and finiteness of the solution. The conditions are the same as the ones for the boson star, the challenge here is to translate them to each of the components of the expansion. The conditions are the following:

- regularity at the origin: $A'(t,0) = B'(t,0) = \psi'(t,0) = 0, \forall t$;
- finiteness of the solution: $\lim_{r\to\infty} \Psi(t,r) = 0, \forall t$;
- asymptotically flat metric.

These general considerations are translated to each of the elements of the expansion:

- $B(t,0) = 1, \forall t$ is read off from the equations of motion, this means that conditions $B_0(0) = 1$ and $B_2(0) = 0$ are guaranteed;
- $\Psi(t,0)$ and $C(t,0)$ are not fixed, which means that we will have the freedom to choose the value of $\psi_1(0)$ and the shooting method (see, e.g., [119]) will provide the values for $\psi_3(0), C_0(0), C_2(0)$;
- regularity at the origin is guaranteed by imposing that the radial derivatives at the origin are zero, for all the components;
- finiteness of the solution translates immediatly into $\lim_{r\to\infty} \psi_1(r) = \lim_{r\to\infty} \psi_3(r) = 0$;
- similarly to the analysis of boson stars, the equations of motion guarantee that $\lim_{r\to\infty} B(t,r) = 1, \forall t$ which means that we will have $\lim_{r\to\infty} B_0(r) = 1$ and $\lim_{r\to\infty} B_2(r) = 0$;

- forcing the metric to be asymptotically flat means that we want $\lim_{r\to\infty} C(t,r) = 1$ which amounts to impose $\lim_{r\to\infty} C_0(r) = 1$ and $\lim_{r\to\infty} C_2(r) = 0$.

Summarizing this analysis, we have five free parameters $\psi_1(0), \psi_3(0), C_0(0), C_2(0), \omega$ and four condition to enforce:

$$\lim_{r\to\infty} \psi_1(r) = 0, \tag{2.76}$$

$$\lim_{r\to\infty} \psi_3(r) = 0, \tag{2.77}$$

$$\lim_{r\to\infty} C_0(r) = 1, \tag{2.78}$$

$$\lim_{r\to\infty} C_2(r) = 0. \tag{2.79}$$

Again, and similarly to the case of BSs, we'll be interested in the ground-state solutions of the EKG system, which means that we obtain scalar profiles $\psi_1(r)$ and $\psi_3(r)$ that do not contain nodes. In Fig. 2.4 we plot the relation between the central value of the dominant scalar component, $\psi_1(0)$, and the numerically obtained frequency value ω.

Finally, notice that since $A(t,r) = B(t,r)/C(t,r)$ (see Eq. (2.65)), the coefficients of A are obtained like this

$$A_0 = \frac{2B_0C_0 - B_2C_2}{2C_0^2 + C_2^2}, \tag{2.80}$$

$$A_2 = \frac{2B_2C_0 - 2B_0C_2}{2C_0^2 - C_2^2}, \tag{2.81}$$

such that A is written as

$$A(t,r) = A_0(r) + A_2(r)\cos(2\omega t). \tag{2.82}$$

2.2.2 Characterizing the self-gravitating solutions

We will use two different ways of characterizing the self-gravitating scalar-field structures. On the one hand, we focus on the more direct quantities that are related to their construction: the central value of the scalar field function ($\psi(0)$ or $\psi_1(0)$) and the fundamental frequency (ω). In Fig. 2.4 it is represented the relation between these two quantities for both BSs and oscillatons. Notice that both types of solutions present a minimum value for the fundamental frequency; that value is different for each of the solutions, with the BSs presenting a lower value than the oscillatons. However not all of the solutions presented in this plot are equally important in terms of astrophysical analysis. As shown in Ref. [36–39, 54] boson stars and oscillatons can be organized in a stable and unstable branch, being the stable branch composed of solutions with a central value of the scalar field smaller than ~ 0.1 as indicated by a vertical line in Fig. 2.4.

Another way to characterize these self-gravitating solutions is through more indirect quantities – the radius and the mass. To calculate the mass, we use the fact that they are spherically symmetric solutions of the Einstein equations, which means that their exterior metric is described, according to the Birkhoff's theorem [120, 121], by a Schwarzschild metric with the corresponding mass parameter. So, one can define the mass of the scalar-field structure as

$$\mu M = \lim_{r\to\infty} \frac{r}{2}\left(1 - \frac{1}{B(t,r)}\right), \tag{2.83}$$

where μ is equal to the mass of the scalar field in Planck units. Unlike fermion stars which have a physical boundary, these scalar-field self-gravitating bound states do not possess one. So, in order to define their radius, one considers the value of the radial coordinate up to which 98% of the total mass is contained. The quantitites obtained in this way can be organized in a Mass-Radius plot (see Fig. 2.5). We see that there is a maximum mass for both types of solutions and they differ slightly. As mentioned before, only a subset of the nodeless solutions of the EKG system is stable; this is the subset that is located to the right of the maximum mass value in the Mass-Radius plot, i.e., all the solutions that have mass smaller than the maximum mass and radius bigger than the radius of the maximum-mass solution.

Well within the stable branch, one can find a region in which BSs and oscillatons solutions give rise to similar structures. This regime is indicated with a small circle in Fig. 2.4 and corresponds to the cases in which the magnitude of the scalar field is very small and the fundamental frequency is approximately given by the mass of the scalar field. In this regime, the metric corresponding to the scalar-field structures is approximately flat so that the whole system can be analysed from a Newtonian perspective.

2.2.3 Newtonian limit

Recovering the analysis made in Appendix A, we will restrict, for convenience, the following analysis to the case of a complex scalar field. Assuming that the frequency of the scalar field function is approximately given by the scalar field's mass, $\omega \approx \mu$, and that the metric deviates

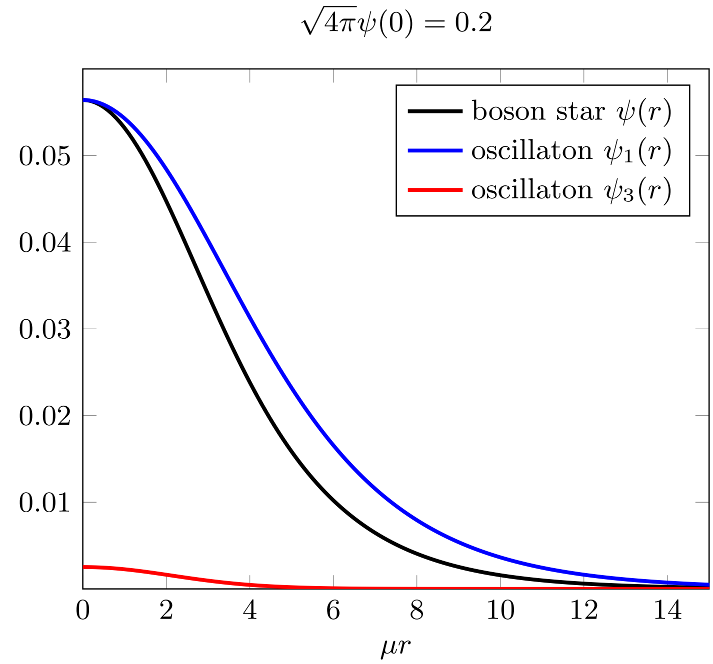

Figure 2.3: Radial profiles of a boson star, $\psi(r)$, and of an oscillaton, $\psi_1(r)$ and $\psi_3(r)$, for the same central value $\psi(0)\sqrt{4\pi} = \psi_1(0)\sqrt{4\pi} = 0.2$.

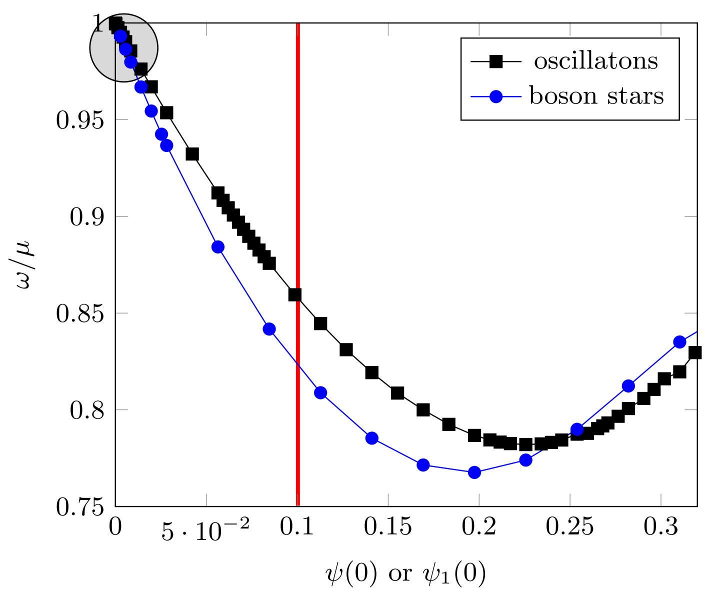

Figure 2.4: Relating the frequency of the scalar field function with the central value of $\psi(r)$, for boson stars, and $\psi_1(r)$, for oscillatons. Notice the little gray circle, which corresponds to a low-energy regime (the bound-state is almost a free state), where the oscillaton and boson star solutions are similar. Notice also the redline; according to Ref. [54] stable configurations are on the left and unstable configurations on the right.

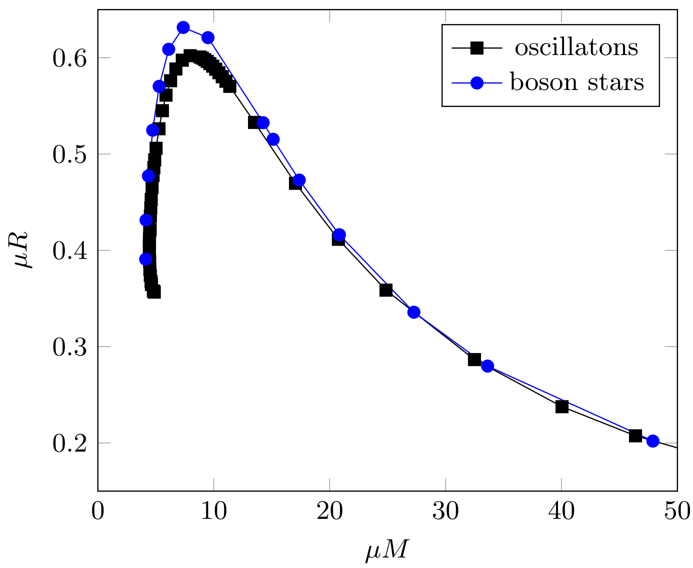

Figure 2.5: Mass-Radius relation for boson stars and oscillatons. Notice the maximum mass attained by both types of structures. In agreement with, e.g., Ref. [22] one can see that $M^{\rm osc}_{\rm max} \sim 0.60 m^2_{\rm Planck}/m_s$, for oscillatons, and $M^{\rm BS}_{\rm max} \sim 0.63 m^2_{\rm Planck}/m$ for boson stars. The configuration with the maximum mass sets the boundary between the stable and unstable branch, with all the solutions to the right of the maximum mass being stable. The central value of the scalar field that corresponds to the maximum mass if given by $\psi \sim 0.1$ and all the configurations with a small value are stable. Notice also that the Newtonian configurations are in the far right of the plot, where the description of BSs and oscillatons agree.

slightly from a flat metric, i.e.,

$$ds^2 = (-1 + 2U)dt^2 + (1 + 2U)dr^2 + r^2 d\Omega^2, \tag{2.84}$$

we know, from Appendix A that the dominant component of the Einstein equations is the Poisson equation (notice that we are not using normalized units here)

$$\nabla^2 U = -4\pi\mu^2 \left|\Psi\right|^2. \tag{2.85}$$

In this limit, and for $\omega \approx \mu$, the scalar field function can be separated in a dominant and a subdominant term as follows:

$$\Psi = \mathrm{e}^{-\mathrm{i}\mu t}\chi(t, r). \tag{2.86}$$

$\chi(t, r)$ contains the slow time-variation of the scalar field as well as the spatial profile. Plugging this into the Klein-Gordon equation

$$\nabla_\alpha \nabla^\alpha \Psi = \mu^2 \Psi, \tag{2.87}$$

and considering the background metric of Eq. (2.84), the low-energy component of the scalar field is described by the Schrodinger equation

$$\mathrm{i}\partial_t\chi = -\frac{1}{2\mu}\nabla^2\chi + \mu U\chi. \tag{2.88}$$

Going back to the Fig. 2.4, we see that the set of oscillatons and BSs that are in the upper left corner ($\omega \approx \mu$ and $\psi(0) \ll 1$) can be conveniently described by

$$\begin{cases} \nabla^2 U &= -4\pi\mu^2 \left|\chi\right|^2, \\ \mathrm{i}\partial_t\chi &= -\frac{1}{2\mu}\nabla^2\chi + \mu U\chi. \end{cases} \tag{2.89}$$

Ref. [54] has set the limit in which the Newtonian and the GR solution agree to be

$$\psi(0) < 10^{-3}. \tag{2.90}$$

2.3 Summary

In this chapter we discussed two astrophysically relevant structures that may develop if ultra-light scalar fields exist. We covered self-gravitating scalar field structures for both complex and real scalar fields, analysing their characteristics and their Newtonian limit. We also explored the quasi-bound states of scalar fields around rotating black holes; our analysis focused in the limit in which the Compton wavelength of the scalar field is much bigger than the gravitational radius of the BH. In this limit, we saw that the maximum value of the scalar field profile is attained very far from the BH. Taking advantage of this circumstance, we calculated the effective gravitational potential that results from the existence of such structure both for the complex and the real case. In the next chapter we will study how the latter case influences the orbital evolution of a binary system.

Chapter 3

Scalar field influence on a generic EMRI

The detection of Gravitational Waves (GWs) by the LIGO collaboration [68] opened a new path in the study of the Universe. LISA [122] – the Laser Interferometer Space Antenna – , one of the new facilities that will improve the capacity to study GWs, is tuned to detect them coming from Extreme-Mass-Ratio-Inspirals (EMRI) [123, 124]. EMRIs are inspiraling binary systems in which the mass of one of the components is much bigger than the other – the ratio should be of the order $10^4 - 10^6$. One of the most favoured scenarios to realize such a system is the one in which a SMBH ($M \sim 10^6 M_\odot$) is orbited by a solar mass BH or by a neutron star or white dwarf. As the lighter element of the binary is expected to inspiral towards the SMBH due to the emission of GWs, any deviation to that scenario will contain information about the environment surrounding the SMBH. In this chapter we focus on an EMRI in which the SMBH supports an ultralight scalar field quasi-bound state – we shall abbreviate it to Black Hole-Scalar Field system (BHSFS). We study the impact of the scalar field structure on the orbital structure of the orbiting body with special emphasis on circular orbits. Unless otherwise stated, normalized variables of Eq. (2.27) are being considered. This chapter is based on Ref. [125].

3.1 Setup

Our hypothesis is that a real, massive scalar-field quasi-bound state exists around a SMBH (see Section 2.1). The scalar field is described by (see Eq. (2.31))

$$\Psi = A_0 \cos(\omega_R t - \phi) r\alpha^2 \mathrm{e}^{-\frac{r\alpha^2}{2}} \sin\theta, \tag{3.1}$$

where $\alpha = M\mu$ (see Eq. (2.21)) and

$$\omega_R \sim \mu. \tag{3.2}$$

The amplitude, A_0, is related to the scalar field total mass

$$A_0^2 = \left[\frac{M_{SC}}{M}\right] \frac{(M\mu)^4}{32\pi}, \tag{3.3}$$

For a cloud with $M_{SC} \sim 20\% M$ we have $A_0 \sim 0.05(M\mu)^2$. We take this as our reference value.

In the limit $M\mu \ll 1$, the maximum value of the radial profile is attained at $r = R_{\text{peak}}$ and this region is far from the BH, meaning that the curvature of spacetime is low and it is valid an analysis of the scalar field using a flat background metric (see details in Section 2.1). In this limit, the gravitational effect of the SMBH is described by a Keplerian potential

$$V_0 = -\frac{1}{r}, \tag{3.4}$$

and the presence of the real scalar field cloud is given by a perturbative potential of the form

$$V_1 \sim V_1^0 + V_1^1 \cos(2(\phi - \omega_R t)), \tag{3.5}$$

which is the solution of the equation (using $\alpha = M\mu$)

$$\nabla^2 V_1 = -4\pi \frac{\alpha^2}{2} \left[A_0 r \alpha^2 \mathrm{e}^{-\frac{r\alpha^2}{2}} \sin\theta\right]^2 \Big(1 - 3\cos\left(2(\omega_R t - \phi)\right)\Big), \tag{3.6}$$

Using the harmonic decomposition technique (see Appendix A), we obtain that the expressions for the perturbative gravitational potential sourced by the presence of the real scalar field is given by

$$V_1^0 = Q_1(r) + Q_2(r)\cos^2(\theta), \tag{3.7}$$

and

$$V_1^1 = Q_3(r)\sin^2(\theta). \tag{3.8}$$

The functions $Q_i(r)$ are given by (we'll use $\alpha = M\mu$ in order to reduce the length of the expressions)

$$Q_1(r) = \frac{A_0^2 \pi e^{-r\alpha^2}}{2\alpha^8 r^3}\Big(-192 - 192\alpha^2 r + 2r^4\alpha^{10} + r^5\alpha^{12} - 4r^3\alpha^8(-3 + r^2\alpha^2) - 24r^2\alpha^6(-1 + r^2\alpha^2) + (16\alpha^2 - 160r^2\alpha^4) + (16r\alpha^4 - 80r^3\alpha^6) - 16e^{r\alpha^2}(-12 + r^2\alpha^6 + (\alpha^2 - 4r^2\alpha^4))\Big), \tag{3.9}$$

$$Q_2(r) = \frac{A_0^2 \pi e^{-r\alpha^2}}{2r^3\alpha^8}\Big(576 + 576r\alpha^2 - 2r^4\alpha^{10} - r^5\alpha^{12} + 48e^{r\alpha^2}(-12 + \alpha^2) + 4r^3\alpha^8(-2 + r^2\alpha^2) + 24r^2\alpha^6(-1 + r^2\alpha^2) + 48\alpha^2(-1 + 6r^2\alpha^2) - (48r\alpha^4 - 96r^3\alpha^6)\Big), \tag{3.10}$$

$$Q_3(r) = \frac{A_0^2 \pi e^{-r\alpha^2}}{2r^3\alpha^8}\Big(-3456 - 3456r\alpha^2 - 2r^4\alpha^{10} - r^5\alpha^{12} + 48e^{r\alpha^2}(72 + \alpha^2) - 8r^3\alpha^8(1 + 3r^2\alpha^2) - 48(\alpha^2 + 36r^2\alpha^4) - 48(r\alpha^4 + 12r^3\alpha^6) - 24(r^2\alpha^6 + 6r^4\alpha^8)\Big). \tag{3.11}$$

We are interested in studying the movement of an orbiting particle whose orbital plane is the equatorial one (i.e. $\theta = \pi/2$) and so, the total gravitational potential which acts on it is given by

$$U_N\left(r, \theta = \frac{\pi}{2}, \phi\right) = V_0 + V_1 = -\frac{1}{r} + Q_1(r) + Q_3(r)\cos(2(\phi - \omega_R t)), \tag{3.12}$$

where (r, ϕ) are inertial polar coordinates in the plane. This potential has two distinctive features. First, it has a radial dependence, which can modify the structure of bound orbits of the background field, for instance changing Kepler's law[1]. Second, it has a periodic angular dependence on ϕ and ω, breaking the axial symmetry of the gravitational potential. This second feature also appears in planetary motion around disks and galactic formation, and therefore can enrich the kinematics of particles around BHs. For convenience, we will organize the potential in Eq. (3.12) specialised to the equatorial plane as

$$U_N(r, \phi) = V_r(r) + \delta V(r, \phi), \tag{3.13}$$

making an explicit separation between the angular and non-angular dependent components.

[1]The new potential will not be proportional to r^{-1} and therefore, according to Bertrand's theorem [126], not all bound orbits will be closed.

3.2 Quasi-circular orbits

To estimate the impact of the presence of the scalar field on the dynamics of the EMRI, we will quantify the modifications it causes on circular orbits. These orbits are the simplest type of orbits in a standard EMRI and understanding how they change in response to the scalar field is a first step towards understanding how the global structure of the EMRI is modified.

Under our assumptions, the study of the orbital behavior of a stellar object in the EMRI reduces to the analysis of the Lagrangian

$$\mathcal{L} = \frac{1}{2}(\dot{r}^2 + r^2(\dot{\phi} + \omega_R)^2) - U_N(r,\phi), \tag{3.14}$$

which describes its motion under the influence of the potential of Eq. (3.13) in a system of coordinates that is corotating with the scalar field. In regions where $|Q_3| \,/\, |V_0| \ll 1$, one can obtain some insight into this system by exploring the effect of the azimuthal-dependent part on the stable circular orbits of the Keplerian potential V_0. The perturbative approach is set up by considering the evolution of small deviations r_1 and ϕ_1 to the radial and angular behavior of a stable circular orbit of radius R_0

$$r(t) = R_0 + r_1(t)\,, \tag{3.15}$$

$$\phi(t) = \phi_0(t) + \phi_1(t)\,, \tag{3.16}$$

where $\phi_0(t) = \phi_i + (\Omega_0 - \omega_R)t$ with $\Omega_0^2 = V_0'(R_0)/R_0$ and, for convenience, we fix the initial condition to be $\phi_i = 0$. Neglecting second order terms in r_1 and $\dot{\phi}_1$, the equations of motion in the corotating frame are written as

$$\ddot{r}_1 + \left(\frac{\partial^2 V_0}{\partial r^2} - \Omega_0^2\right) r_1 - 2\Omega_0 R_0 \dot{\phi}_1 + \frac{\partial Q_1}{\partial r} + \frac{\partial(\delta V)}{\partial r} = 0\,, \tag{3.17}$$

$$\ddot{\phi}_1 + \frac{2\Omega_0}{R_0}\dot{r}_1 + \frac{1}{R_0^2}\frac{\partial(\delta V)}{\partial \phi} = 0\,, \tag{3.18}$$

in which all derivatives are evaluated at $r = R_0$. To study Eqs. (3.17) and (3.18) we consider that, since $\phi_1(t) \ll \phi_0(t)$, one can write the expression for δV considering that $\phi(t) \sim (\Omega_0 -$

$\omega_R)t$. The equations are then written as

$$\ddot{r}_1 + \left(\frac{\partial^2 V_0}{\partial r^2} - \Omega_0^2\right) r_1 - 2\Omega_0 R_0 \dot{\phi}_1 + \frac{\partial Q_1}{\partial r} + \frac{\partial Q_3}{\partial r}\cos(2(\Omega_0 - \omega_R)t) = 0\,, \tag{3.19}$$

$$\ddot{\phi}_1 + \frac{2\Omega_0}{R_0}\dot{r}_1 - \frac{2}{R_0^2} Q_3 \sin(2(\Omega_0 - \omega_R)t) = 0\,, \tag{3.20}$$

where the coefficients are evaluated at $r = R_0$. Integrating Eq. (3.20) and substituting the result in (3.19) one obtains

$$\ddot{r}_1 + \left(\frac{\partial^2 V_0}{\partial r^2} + 3\Omega_0^2\right) r_1 + \frac{\partial Q_1}{\partial r} = -B(R_0)\cos(2(\Omega_0 - \omega_R)t), \tag{3.21}$$

whose general solution is given by

$$r_1(t) = A\cos(\kappa_0 t + \alpha) - B(R_0)\frac{\cos(2(\Omega_0 - \omega_R)t)}{\kappa_0^2 - 4(\Omega_0 - \omega_R)^2} - \frac{C(R_0)}{\kappa_0^2}, \tag{3.22}$$

$$\phi_1(t) = -\frac{2\Omega_0 A}{R_0 \kappa_0}\sin(\kappa_0 t + \alpha) + D(R_0)\sin(2(\Omega_0 - \omega_R)t) - \frac{C(R_0)}{\kappa_0^2}t, \tag{3.23}$$

with $\kappa_0^2 = V_0'' + 3\Omega_0^2$ and

$$A = \left[r_{1i} - \frac{B}{\kappa_0^2 - 4(\Omega_0 - \omega_R)^2} + \frac{C}{k_0^2}\right]\cos^{-1}\alpha, \tag{3.24}$$

$$\tan\alpha = \dot{r}_{1i}^{-1}\kappa_0\left[\frac{C}{k_0^2} - r_{1i} - \frac{B}{\kappa_0^2 - 4(\Omega_0 - \omega_R)^2}\right], \tag{3.25}$$

$$B = \frac{\partial Q_3}{\partial r} + \frac{4\Omega_0 Q_3}{R_0(\Omega_0 - \omega_R)}, \tag{3.26}$$

$$C = \frac{\partial Q_1}{\partial r}, \tag{3.27}$$

$$D = \frac{\Omega_0 B}{R_0(\kappa_0^2 - 4(\Omega_0 - \omega_R)^2)(\Omega_0 - \omega_R)} - \frac{Q_3}{R_0^2(\Omega_0 - \omega_R)^2}, \tag{3.28}$$

where all the quantities are calculated at R_0 and $(r_{1i}, \dot{r}_{1i})$ are the initial conditions for the radial motion. This kind of solution is long known in problems with non-axisymmetric potentials (see, e.g., Refs. [127–131]). We can readily see the presence of some singularities in Eqs. (3.22), (3.24) and (3.28). Two of the singularities appear when

$$\kappa_0 = \pm 2(\Omega_0 - \omega_R)\,. \tag{3.29}$$

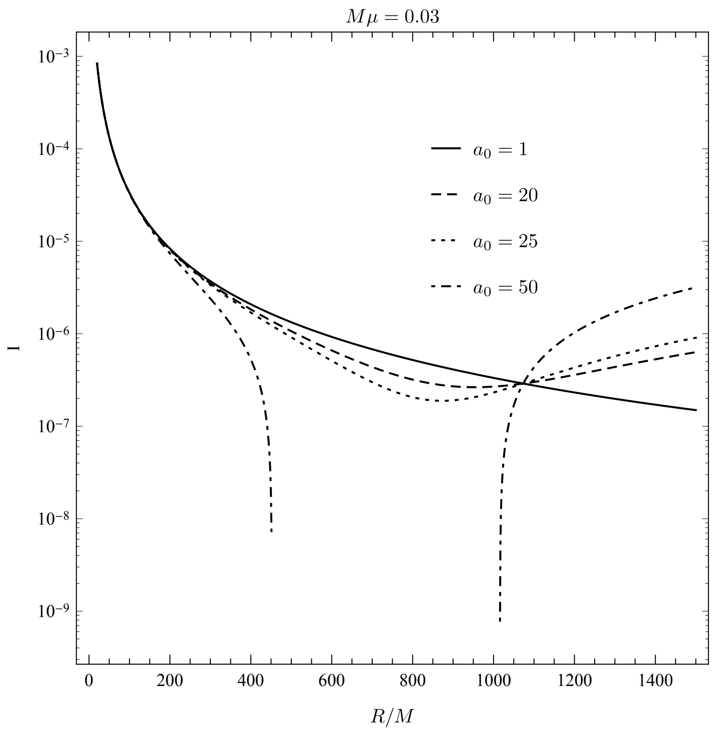

Figure 3.1: Representing the instability measure I of Eq. (3.32) as a function of the radius of the circular orbit for mass coupling $M\mu = 0.03$ and different scalar-field amplitudes. Large scalar amplitudes give rise to a set of unstable orbits. Notice that the range of radii in which the instability measure is negative, depends on the value of the parameter a_0.

These are called Lindblad (inner and outer) resonances. The other singularity, given by

$$\Omega_0 = \omega_R, \tag{3.30}$$

is called co-rotating resonance, because the perturbation is being made to a circular orbit which is synchronized with the potential (in this case with the scalar cloud). When a resonant frequency is approached, the above linear analysis breaks down. We shall look into these particular orbits in the following sections. The radii at which the outer (inner) Lindblad resonance occurs will be termed outer (inner) Lindblad radius $R_{L\pm}$. The radius at which the co-rotating resonance occurs is the co-rotation radius R_C.

3.2.1 Circular orbits

Before considering the effects of the angular part of the gravitational potential, we will focus on the effects due to its radial term only. To further explore its effects, we ignore the presence of the ϕ-dependent part of the potential V_1 in the Eqs. (3.19) and (3.20) and the solution is given by Eqs. (3.22) to (3.25) with $B(r) \equiv 0$ and $D(r) \equiv 0$. As in the analysis with the angular part of the potential, the behavior of the perturbations indicates that the circular stable orbits of the BHSFS are not exactly Kleperian. We start with initial conditions at $r_{1i} = \dot{r}_{1i} = 0$, and initial radius such that the orbit would be circular if the scalar cloud did not exist. We find a solution that deviates from the Keplerian circular orbit. This, of course, is expected: given a value of the angular momentum, the corresponding value of the radius of the circular orbit of the total radial potential V_r is different from the radius of the circular orbits of V_0. Quantifying this radial difference is a way of looking into the influence of the scalar field on the orbital structure around the SMBH. We will indicate the radii of the circular orbits of the total potential V_r by R_0^*; their values are given, for fixed angular momentum L, by

$$\frac{L^2}{(R_0^*)^3} = \frac{dV_r}{dr}, \tag{3.31}$$

where the derivative is taken at R_0^*. The stability of these orbits is guaranteed as long as [132]

$$I \equiv \frac{dV_r}{dr} + \frac{R_0^*}{3}\frac{d^2V_r}{dr^2} > 0. \tag{3.32}$$

This inequality is always verified in the range of the mass coupling parameter we are considering, thus all circular orbits of the potential V_r are stable. Notice, however, that the amplitude of the scalar field can be larger. Parametrizing the amplitude of the scalar field as

$$\tilde{A}_0 = a_0 A_0, \tag{3.33}$$

where A_0 is the standard amplitude of the scalar field (see Eq. (3.3)), we observe that for $a_0 > a_0^{\mathrm{insta}}$, unstable orbits appear. More precisely, for $a_0 < a_0^{\mathrm{insta}}$ all circular orbits are stable and for $a_0 > a_0^{\mathrm{insta}}$ a window of unstable circular orbits with $R_{\mathrm{min}} < R_0^* < R_{\mathrm{max}}$ exists. This is shown in Fig. 3.1, where it is represented the quantity described in Eq. (3.32). Furthermore, it is also observed that after crossing the boundary imposed by a_0^{insta}, the range $\{R_{\mathrm{min}}, R_{\mathrm{max}}\}$ increases with a_0.

For small values of the angular momentum and mass coupling parameter, the difference between the radius of Keplerian circular orbits, R_0, and the radius of circular orbits of the BHSFS, R_0^*, is negligible[2]; however, this difference has a non-trivial evolution once we start to

[2]We keep the angular momentum fixed. This observation shows that close to the SMBH Keplerian circular orbits are good approximations for the circular orbits of the whole system. This reinforces the validity of the

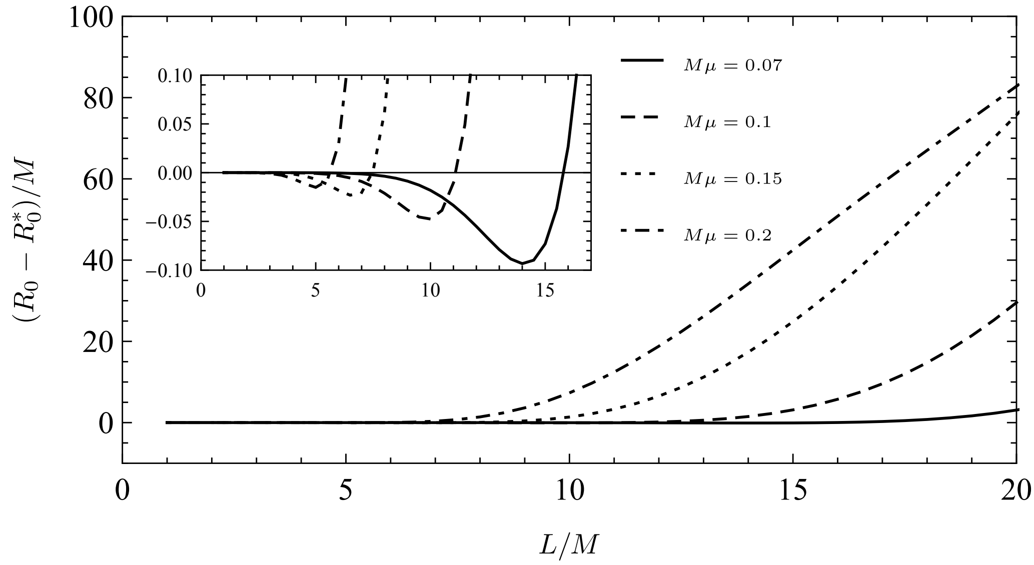

Figure 3.2: Difference between the radius of a Keplerian circular orbit with angular momentum L and the radius of a circular orbit of the potential V_r (Eq. (3.13)) with the same angular momentum. For small values of the angular momentum the difference is negligible, but then it grows indefinitely for larger values. This growth means that, far from the SMBH, a stable circular orbit of the BHSF system with a given angular momentum has a smaller radius than its Keplerian counterpart (in which the Kepler potential is generated only by the SMBH).

vary those parameters; this can be appreciated in Fig. 3.2. As the angular momentum increases, the difference between the radii has a behavior which is controlled by the value of the mass coupling parameter: large values of α imply a large radii difference for a fixed value of the angular momentum. Notwithstanding, the difference in radii at large distances is due to the fact that now the orbiting particle sees a different effective mass (central object plus the scalar field surrounding it, see Fig. 3.3).

Another way of looking at the difference between the circular orbits of an isolated BH and a scalar-surrounded one is to observe that close to the SMBH a potential $V = -M/r$ is dominant, while far from the SMBH the dynamics are dominated by $V = -M_{\text{eff}}/r$ in which M_{eff} is an effective mass value, in units of the mass M of the SMBH. It was numerically found that our system has $M_{\text{eff}} \sim 1.26$, as can be seen in Fig. 3.3. This number can be interpreted by looking at Eq. (3.31) in the form

$$L^2 = R_0^* + R_0^{*3} \frac{\partial Q_1}{\partial r}(R_0^*), \tag{3.34}$$

results we obtained for the location of the resonant orbits.

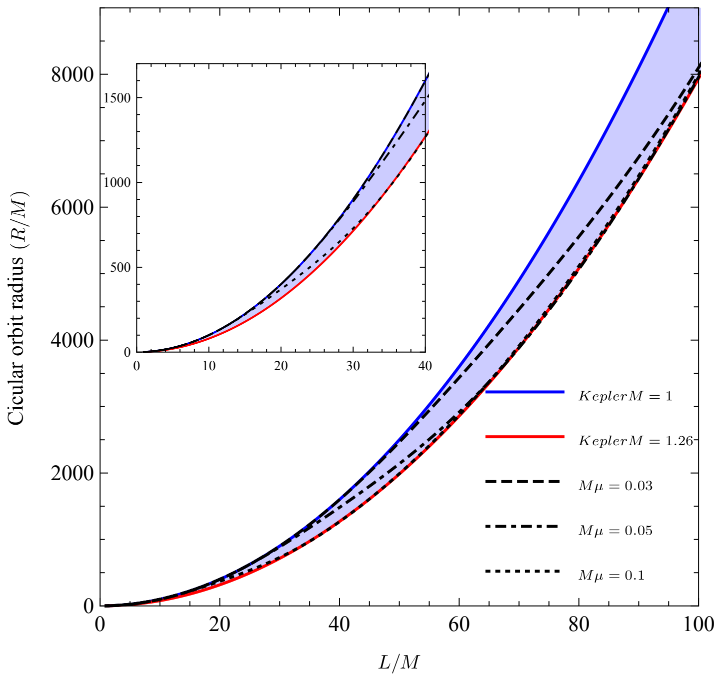

Figure 3.3: Representing the value of the radii of stable circular orbits as a function of the angular momentum. Continuous lines refer to circular orbits of a Keplerian potential $-M/r$ – the blue line corresponds to a Keplerian potential with $M = 1$ and the red line to $M = 1.26$. Discontinuous lines represent the radii of circular orbits for the potential of the BHSF system V_r; for small values of the angular momentum, these values are similar to those generated by a Keplerian potential with $M = 1$ while for large values of the angular momentum they stabilize to the curve described by the Keplerian potential with $M = 1.26$. This fact leads us to the conjecture that any other mass coupling parameter would generate a plot that would be bounded by the two Keplerian curves; the only influence of the mass coupling parameter is the extent to which the radii of circular orbits deviate from a Keplerian relation, as can be seen in the inline. In fact, the bigger the mass coupling parameter the smaller is the range of the deviation.

and observing that for large values of angular momentum L and radius R_0^* it can be written as

$$L^2 = R_0^* + R_0^{*3}\left(\frac{32\pi a_0^2}{R_0^{*2}}\right), \tag{3.35}$$

where the amplitude of the scalar field A_0 was again written as $A_0 = a_0(M\mu)^2$. Using the value for a_0 prescribed in Eq. (3.3) we obtain

$$L^2 = 1.25R_0^* \tag{3.36}$$

which is close to the value obtained numerically[3]. We see, then, that far from the SMBH the potential governing the dynamics is still Keplerian, but the mass sourcing it is not the SMBH mass. This "effective" mass M_{eff} corresponds to the mass of the SMBH plus the total mass contained the scalar field.

3.2.2 Resonant orbits

For the rest of this section, we will go back to Eqs. (3.22) and (3.23), focusing on the resonant orbits. For a particle near the resonant orbits, the general perturbative approach presented in those equations is not adequate since it gives unphysical behavior for the perturbations[4]. Our main motivation to pursue a more detailed analysis of these orbits is their important role in the so called angular momentum transfer mechanisms in the context of galactic dynamics [135–137]. In other words, it is possible that BHs anchoring scalar fields may give rise to galactic-like structure on lengthscales of a few hundred Schwarzschild radii.

The radii of the circular orbits that correspond to the resonant frequencies are obtained by substituting the expressions for the angular frequency $\Omega(r)$ and the epicyclic frequency $\kappa(r)$ in the equations defining the resonances and solving for the radial coordinate. By doing this, one can immediately see that the smallest of the three resonant radii is the one that corresponds to the inner Lindblad frequency. In order to guarantee that Newtonian mechanics can be used to study the inner Lindblad resonant orbit, its radius should be considerably bigger than the gravitational radius of the SMBH; to be precise, let's consider that it is an order of magnitude bigger, i.e. $R_{L-} \gtrsim 20M$. This scale can be controlled by the mass coupling $\alpha = M\mu$ given

[3]Recall that, using non-scaled variables, the circular orbit of a Keplerian potential $-M/r$ with angular momentum L has a radius given by $R = L^2/M$.

[4]The complete understanding of this problem is out of the scope of our work. More details can be found in Refs. [133, 134].

that the scalar field rotates with angular frequency $\omega_R \sim \alpha$; taking this into account, the inner Lindblad radius is given by

$$\frac{R_{L-}}{M} \approx \left(\frac{1}{4(M\mu)^2}\right)^{1/3}, \tag{3.37}$$

from which one can estimate the maximum value of $M\mu$ such that a Newtonian analysis is justified, which in the case $R_{L-} \gtrsim 20M$, corresponds to $\alpha \lesssim 0.006$. Once the inner Lindblad radius is sufficiently far from the central BH such that Newtonian mechanics is valid, then the other two resonances (corotation and outer Lindblad resonance) are automatically ensured to be within the same regime. The corotation and outer Lindblad radii are, respectively,

$$\frac{R_C}{M} \approx \left(\frac{1}{(M\mu)^2}\right)^{1/3}, \quad \frac{R_{L+}}{M} \approx \left(\frac{9}{4(M\mu)^2}\right)^{1/3}, \tag{3.38}$$

i.e., $R_{L-} < R_C < R_{L+}$.

The analytical solutions we shall be presenting for the quasi circular resonant orbits follow from the same assumptions made for the general quasi-circular orbits, i.e., the perturbations r_1 and ϕ_1 will be considered small. To do this, we take the equations of motion for the perturbations and analyze them separately for each of the three resonant frequencies mentioned previously.

Lindblad Resonances

To study the behavior of the system at the Lindblad resonances, we have to go back to equations (3.19) and (3.20) and make the explicit substitution

$$R_0 \to R_{L\pm} \quad \Omega_0 \to \omega_R \pm \frac{1}{2}\kappa_{L\pm}, \tag{3.39}$$

which under the same reasoning applied before will allow us to write

$$\ddot{r}_1 + \kappa_{L\pm}^2 r_1 + C(R_{L\pm}) + \tilde{B}(R_{L\pm})\cos(\kappa_{L\pm}t) = 0, \tag{3.40}$$

with

$$\tilde{B}(R_{L\pm}) = \frac{\partial Q_3}{\partial r} \pm \frac{4\Omega_0 Q_3}{R_{L\pm}\kappa_{L\pm}}. \tag{3.41}$$

The differences between the equations for the inner and the outer Lindblad orbits are the numerical value of the epicyclic frequency, the sign in the equation of motion for ϕ_1 (see Eq. (3.45)) and the functions $B(r), C(r)$. The previous equation has a direct analytic solution given by

$$r_1(t) = -\frac{1}{\kappa_{L\pm}^2}\left[2C(R_{L\pm})+(\tilde{B}(R_{L\pm})-2\kappa_{L\pm}^2\Gamma_1)\cos(\kappa_{L\pm}t)+\kappa_{L\pm}^2(\tilde{B}(R_{L\pm})t-2\kappa_{L\pm}\Gamma_2)\sin(\kappa_{L\pm}t)\right], \tag{3.42}$$

where Γ_1 and Γ_2 depend on the initial conditions as

$$\Gamma_1 = \frac{1}{2\kappa_{L\pm}^2}\left[r_{1i}\kappa_{L\pm}^2 + 2C(R_{L\pm}) + \tilde{B}(R_{L\pm})\right] \tag{3.43}$$

$$\Gamma_2 = \frac{1}{2\kappa_{L\pm}^2}\dot{r}_{1i}. \tag{3.44}$$

Using this expression for the evolution of r_1 in

$$\dot{\phi}_1 + \frac{2(\omega_R \pm \frac{1}{2}\kappa_{L\pm})}{R_{L\pm}}r_1 \pm \frac{2Q_3(R_{L\pm})}{\kappa_{L\pm}R_{L\pm}^2}\cos(\kappa_{L\pm}t) = 0, \tag{3.45}$$

one can derive the expression for ϕ_1.

The solutions for r_1 and ϕ_1 at Lindblad resonances show a different behavior from the general case (3.22) and (3.23), with the radial perturbation growing significantly even when the orbiting body is initially placed in a circular orbit, i.e., when $r_{1i} = \dot{r}_{1i} = 0$. Note that we chose initial conditions to correspond to a circular orbit *in the absence of a scalar cloud*. Because of the term proportional to the time parameter in Eq. (3.42), the radial perturbation increases at each period of oscillation – see Fig. 3.4. This behavior results from the fact that up to first order, the perturbation r_1 is described by the equation of motion for a harmonic oscillator (with natural frequency given by $\kappa_{L\pm}$) being excited by a harmonic force with the same frequency. This is a classical example of resonance. While the first order approximation holds, the value of the radial perturbation increases as seen in Fig. 3.5. Once this approximation stops being valid, which eventually happens if enough time passes, the higher order components of the equations of motion describing r_1 and ϕ_1 become important and the evolution of the radial perturbation is no longer described by Eq. (3.42); the higher order terms force r_1 to decrease, as can be seen in Fig. 3.5, ending up describing a beating pattern. The time that it takes for a complete beat, both at inner and outer Lindblad resonances, depends on the mass coupling parameter and on the amplitude a_0 of Eq. (3.33); we numerically compute this dependence, finding a good fit to be

$$\tau_{\text{beat}} \sim \frac{1}{a_0^{1.3}}\frac{21.5M}{(M\mu)^{\frac{91}{25}}}, \tag{3.46}$$

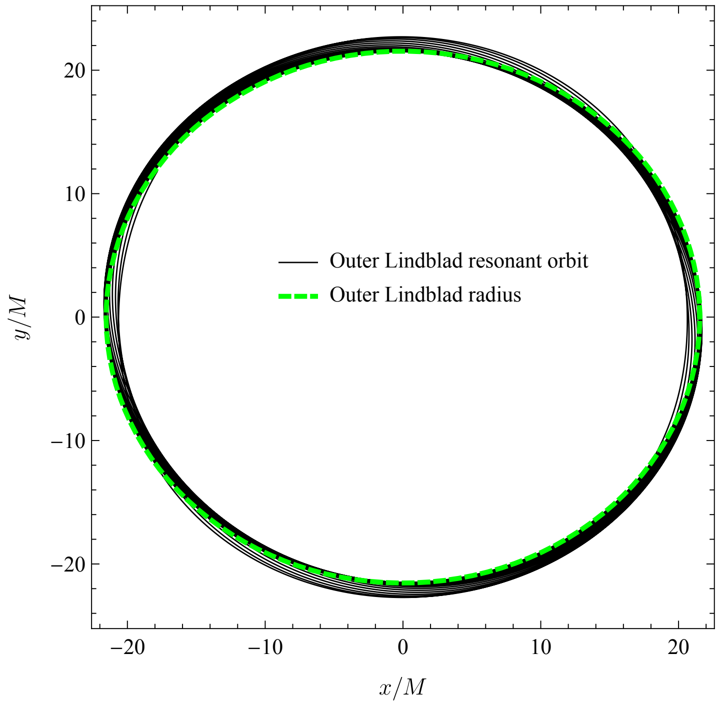

Figure 3.4: Representing the orbit of a particle at the outer Lindblad resonance. We used $M\mu = 0.015$ and we artificially enhanced the scalar field amplitude (again, we artificially increased the amplitude to $\tilde{A}_0 = 350A_0$, where A_0 is the standard amplitude of the scalar field given by $A_0 = 0.05(M\mu)^2$) to allow for an easier representation of the main characteristics. The behavior presented is described by a first order approximation (see Eq. (3.42)) where an increase in the radius of the orbit can be seen.

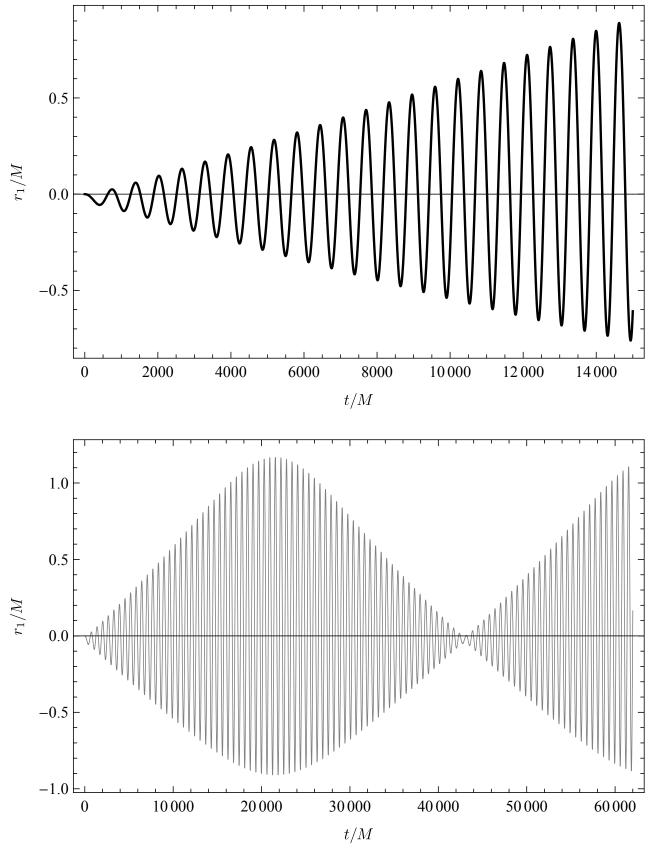

Figure 3.5: Representing $r_1(t) = r(t) - R_{L+}$. Notice that this calculation was made using the initial conditions $\dot{r}_{1i} = r_{1i} = 0$, meaning that the particle was initiated in the circular orbit with radius given by the outer Lindblad radius. The amplitude of the scalar field is artificially enhanced (we use an amplitude $\tilde{A}_0 = 350A_0$ where A_0 is the standard amplitude of the scalar field given by $A_0 = 0.05(M\mu)^2$) in order for the beatting pattern to be more easily observed. The mass coupling parameter used is $M\mu = 0.015$ so that the outer Lindblad radius is $R_{L+} \sim 21.5M$. *Top panel:* The first order evolution of the perturbation r_1 is represented, agreeing with the analytical expression of Eq. (3.42) (see Fig. 3.4 for a depiction of the orbit). *Bottom panel:* As the absolute value of the perturbation increases due to the first order resonant behavior, higher orders of the equation of motion acquire importance preventing an indefinite grow of r_1 by giving rise to a beat pattern.

which means that the analytic solutions of Eq. (3.42) and (3.45) are accurate up to $\tau_{\text{beat}}/2$ in which the maximum value of r_1 is attained.

Corotation Resonance

Going back to the equation of motion (3.17) and (3.18), considering that the circular orbit has a radius given by the corotation radius we see that the zeroth order term vanishes identically and (see Eq. (3.16))

$$\phi(t) = \phi_i + \phi_1(t). \tag{3.47}$$

Thus, what sets corotation apart from the general orbits and Lindblad orbits is the fact that besides the initial condition of the radial perturbation, also the initial angle is important for the motion, as can be seen in the corotation equations of motion

$$\ddot{r}_1 + \left(\frac{\partial^2 \Psi_0}{\partial r^2} - \omega_R^2\right) r_1 - 2\omega_R R_C \dot{\phi}_1 + C(R_C) + \frac{\partial Q_3}{\partial r}\left[\cos(2\phi_i) - 2\sin(2\phi_i)\phi_1\right] = 0\,, \tag{3.48}$$

$$\ddot{\phi}_1 + \frac{2\omega_R}{R_C}\dot{r}_1 - \frac{2Q_3}{R_C^2}\left[\sin(2\phi_i) + 2\cos(2\phi_i)\phi_1\right] = 0, \tag{3.49}$$

where the coefficients are computed at the corotation radius. To write these equations, we considered that the angular perturbation ϕ_1 is small enough to allow for the expansion of the corresponding sinusoidal functions up to first order. Moreover, we observed that in order for the analytical solution to be valid, the initial condition $\phi_{1i} = \phi_1(t = 0)$ has to be of the same order as ϕ_1[5]. After all these cautionary remarks, one can advance to the solution of the equation of motion; the method used previously to obtain the expressions describing the motion of the orbiting body is not adequate in this case. One has to employ a more evolved method, described in Appendix B, which in general gives a solution of the form

$$r_1(t) = C_1 \cos(\omega_1 t) + C_2 \cos(\omega_2 t), \tag{3.50}$$

$$\phi_1(t) = C_3 \sin(\omega_1 t) + C_4 \sin(\omega_2 t), \tag{3.51}$$

[5]The approach presented here focuses on motions around the point $\phi_i = 0$, a stable Lagrangian point. For an alternative approach to the study of the motion at corotation, see Section 3.3 of Ref. [131].

or

$$r_1(t) = C_1 \sin(\omega_1 t) + C_2 \sin(\omega_2 t), \tag{3.52}$$

$$\phi_1(t) = C_3 \cos(\omega_1 t) + C_4 \cos(\omega_2 t), \tag{3.53}$$

where ω_i depends only on the parameters of the problem—both the scalar field and the mass of the SMBH—and C_i depends on the parameters of the problem and the initial conditions. Comparison with the numerical calculations (see Table 3.1) shows good agreement with the analytical solutions for an arbitrary range of the time parameter. In general, one of the sinusoidal functions in the solution for r_1 and ϕ_1 dominates over the other leading to the so called banana orbits [138] which can be appreciated in Fig. 3.6. The width of the banana orbits, which is related to the maximum value attained by the radial perturbation r_1, is dependent on the amplitude of the scalar field but also on the initial angle. The extent of the banana orbit, i.e., the angular range it covers, depends only on the initial conditions of the problem, particularly on the initial angle. Hence, no matter how thin it is, a banana orbit will always be found close to a stable Lagrangian point (see Appendix A) as a result of an initial angle $\phi_{1i} \neq 0$. On the other hand, the time it takes for an orbiting body to describe a complete banana orbit does not depend on the initial angle, being determined by the mass coupling parameter as

$$\tau_{\text{banana}} \sim \frac{15M}{(M\mu)^3}, \tag{3.54}$$

meaning that banana orbits take less time to appear for higher mass couplings[6].

If the initial angle is precisely at $\phi_{1i} = \pi/2$ then the resulting orbit is not a banana orbit. This particular initial angle corresponds to an unstable Lagrangian point (see Appendix B) and a particle that starts there will cover the whole angular range. For initial angles bigger than $\pi/2$, the banana orbits are recovered, but in this case they will be centered around the stable Lagrangian point $\phi_i = \pi$.

As this discussion illustrates, one sees that the position of the Lagrangian points determines the shape of corotation orbits. Most notably, the proximity to a given Lagrangian point determines the way the orbiting body reacts to a perturbation: a particle at an unstable Lagrangian

[6]This timescale is much smaller than the instability time scale of the scalar field we are considering, which is given by $\tau/M \sim (M\mu)^{-9}$ (see Section 2.1).

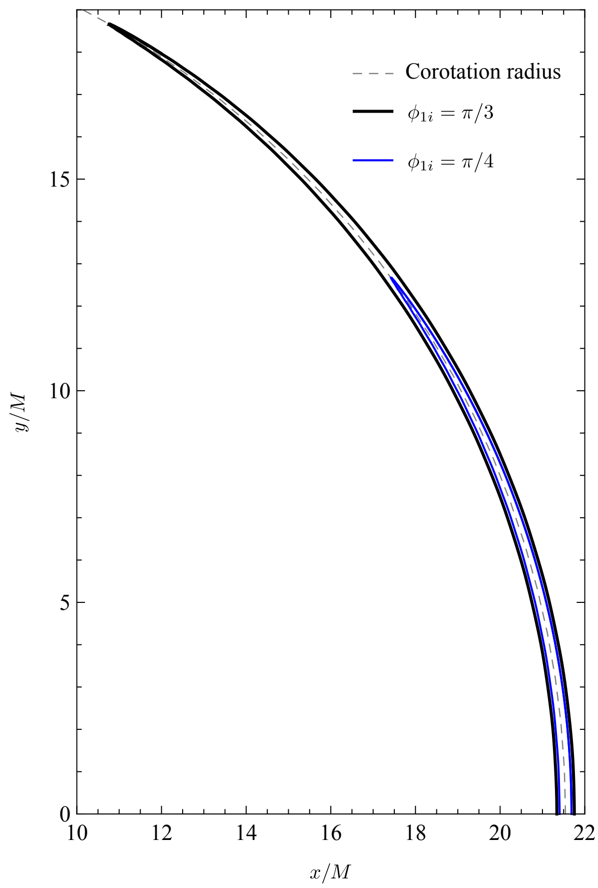

Figure 3.6: Representing banana orbits. The mass coupling parameter used in the calculations is $M\mu = 0.01$ so that the corotation radius is given by $R_C \sim 21.5M$. The orbits are depicted in the co-rotating frame and because they are symmetric in y we show only one quadrant. We used an artificially enhanced amplitude for the scalar field (we use $\tilde{A}_0 = 350A_0$) in order to make possible a clearer representation of the orbits. We show two initial angles, $\phi_{1i} = \pi/3$ and $\phi_{1i} = \pi/4$. The influence of the initial angle on the extent and on the width of the banana orbit is apparent, and can be related to the approximate analytic solution presented in Table 3.1.

Table 3.1: The general solution, described by Eqs. (3.50)-Eq. (3.53), for the specific cases described in Figs. 3.6 and 3.7. To obtain these values we applied the method described in Appendix B. From these expressions we can see the immediate influence of the initial perturbations ϕ_{1i} and r_{1i} on the amplitude of the solutions.

Initial conditions	$\boldsymbol{r_1(t)}$	$\boldsymbol{\phi_1(t)}$
$r_{1i} = \dot{r}_{1i} = \dot{\phi}_{1i} = 0$	$r_1 = \phi_{1i}[-0.004\sin(0.01t) + 0.2\sin(0.0002t)]$	$\phi_1 = \phi_{1i}[-0.0004\cos(0.01t) + \cos(0.0002t)]$
$\phi_{1i} = \dot{r}_{1i} = \dot{\phi}_{1i} = 0$	$r_1 = r_{1i}[-3\cos(0.01t) + 4\cos(0.0002t)]$	$\phi_1 = r_{1i}[0.3\sin(0.01t) + 17\sin(0.0002t)]$

point will spend some time at that point, which depends on the mass coupling parameter as

$$\tau_{\text{unstable}} \sim \tau_{\text{banana}} \sim \frac{15M}{(M\mu)^3}, \tag{3.55}$$

and then it will rapidly move to the other unstable Lagrangian point. On the other hand, a particle at a stable Lagrangian point stays there indefinitely or, in case of a perturbation, librates around it - it is this libration that gives rise to banana orbits.

The libration around stable Lagrangian points may induce an accumulation of orbiting bodies in the surrounding regions. In fact, perturbations to a body sitting exactly at a stable Lagrangian point will force it to librate around it, as shown in Fig. 3.7, and find itself trapped. A similar effect was obtained in N-body calculations in a galactic setting [139] and constitutes a fingerprint of a gravitational potential of the form given in Eq. (3.12)

3.2.3 Orbital torque

The fact that the perturbing gravitational potential imposed by the presence of the scalar field has an angular component means that the angular momentum is not exactly conserved (cf. Eq. (3.18)). The angular momentum of the orbiting body initialized in a circular orbit of radius R_0 is given by

$$L = (R_0 + r_1)^2(\Omega_0 + \dot{\phi}_1), \tag{3.56}$$

and the the torque responsible for this is, up to first order, given by

$$\frac{dL}{dt} = \frac{dL_1}{dt} = 2R_0\Omega_0\dot{r}_1 + R_0^2\ddot{\phi}_1. \tag{3.57}$$

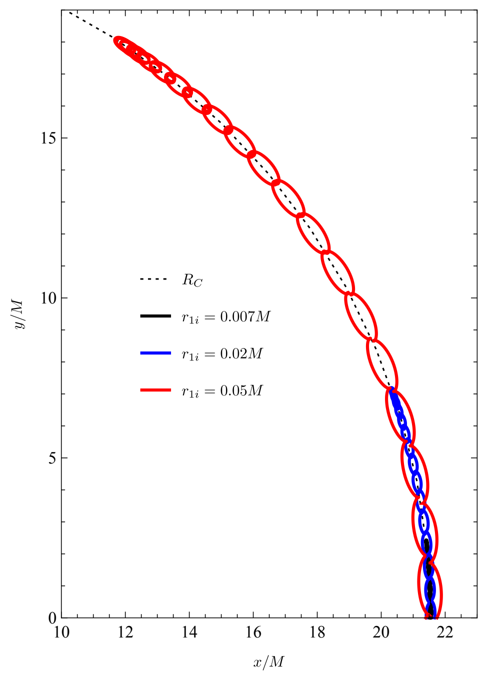

Figure 3.7: Orbital motion due to a radial perturbation to a particle at the stable Lagrangian point $\phi_i = 0$. The amplitude of the scalar field is artificially enhanced (we use $\tilde{A}_0 = 350A_0$) so that the features of the movement are clearer and the mass coupling parameter used is $M\mu = 0.01$. The orbits are initiated at radial position $r(0) = R_C + r_{1i}$ for different values of the radial perturbation r_{1i} as an illustration of the fact that nearly circular orbits in the vicinity of the corotation orbit are described by a libration around stable Lagrangian points. The approximate analytical solution describing the motion is presented in Table 3.1.

To get an idea of the magnitude of this effect, we calculate the average value of this quantity over a revolution around the central BH

$$\left\langle \frac{dL_1}{dt} \right\rangle = \frac{1}{\Delta t} \int_0^{\Delta t} \frac{dL_1}{dt} dt, \tag{3.58}$$

where Δt is the interval over which we average. We obtain an expression for this quantity by observing that the expression for $\ddot{\phi}_1$ is related with r_1 (see Eq. (3.20) and (3.49)) such that we can write

$$\frac{dL_1}{dt} = 2Q_3 \sin(2(\Omega_0 - \omega_R)t) \tag{3.59}$$

for the general case,

$$\frac{dL_1}{dt} = 4Q_3 \Big(\sin(2\phi_i) + \cos(2\phi_i)\phi_1 \Big) \tag{3.60}$$

for the corotation case and

$$\frac{dL_1}{dt} = \pm 2Q_3 \sin(\kappa_{L\pm} t) \tag{3.61}$$

for the inner and outer Lindblad case. The average values are

$$\left\langle \frac{dL_1}{dt} \right\rangle = 0 \tag{3.62}$$

for the general case,

$$\left\langle \frac{dL_1}{dt} \right\rangle = \pm \frac{(\Omega_0 - \omega_R)}{\pi} Q_3 \left(\frac{1 - \cos\left(\frac{2\pi\kappa_{L\pm}}{\Omega_0 - \omega_R}\right)}{\kappa_{L\pm}} \right) \tag{3.63}$$

for the inner (minus sign) and outer (plus sign) Lindblad resonances, where we used $\Delta t = 2\pi/(\Omega_0 - \omega_R)$, and

$$\begin{aligned} \left\langle \frac{dL_1}{dt} \right\rangle = \frac{2\omega_R}{\pi} Q_3 \Big(& 2\sin(2\phi_i) + 2\cos(2\phi_i) \times \\ & \Big[\frac{C_3}{\omega_1} \big(1 - \cos(2\pi\omega_1/\omega_R)\big) + \frac{C_4}{\omega_2} \sin(2\pi\omega_2/\omega_R) \Big] \Big) \end{aligned} \tag{3.64}$$

for the corotation case, where we considered $\Delta t = 2\pi/\omega_R$.

The change in the angular momentum of a particle over a complete orbit around the BH is considerable only when the particle is orbiting at a resonant orbit. Particularly, since the function Q_3 is overall negative, we see that at the inner Lindblad resonance there is an increase in the angular momentum while at the outer Lindblad resonance there is a decrease. At the corotation resonance the angular momentum transfer depends structurally on the initial angle ϕ_i: explicitly, as argument of sinusoidal functions, and implicitly, affecting the values of the constants C_3 and C_4 (cf. Appendix B). The latter fact can be seen by calculating the change in the angular momentum of a particle in a stable Lagrangian point $\phi_i = 0$ or $\phi_i = \pi$.

In any case, in the mass coupling limit we are considering the angular momentum changes only slightly. Be that as it may, the transfer of angular momentum from the scalar cloud can play an important role on the dynamical evolution of the EMRI in more extreme regimes.

3.3 Discussion

While the existence of light, weakly-coupled scalar fields as part of the description of the physical universe may still be a question to be solved, their potential to produce unique effects in the vicinity of SMBHs is a settled issue. Although the analysis we present doesn't take into account the backreaction of the scalar field to the presence of the orbiting particle or the regions closer to the BH's event horizon, the appearance of resonances in the orbital history of EMRIs is an inescapable feature if a real scalar field exists around the central BH. Our calculations identified the three most important ones – the two Lindblad and the corrotating one. The appearance of these resonances is a direct consequence of the "Newtonian pressure" that survives in the low-energy limit of real scalar field structures. In spite of the appealing phenomenology associated with them, particularly the similarity with the effects giving rise to angular momentum transfer occuring in accretion disks, one would need a very massive cloud to have spectacular orbital effects. Our results show that with conservative assumptions, the effects are small. In any case, the orbital resonances are not the only effect that we observe. The presence of the scalar cloud, no matter its mass, will introduce an "invisible" mass distribution, with a toroidal-like shape, surrounding the BH. Its presence changes the structure of the orbital distribution around the BH. The transition between the regions influenced by the presence of the cloud (i.e. orbits with a radius bigger or equal to the peak of the cloud) to regions where its presence isn't felt (orbits with radius smaller than the peak of the cloud) will also have an impact on EMRIs' orbital evolution. While the detection of the orbital resonances is a distinct sign of the presence of a real scalar field cloud surrounding the central BH, the effects of the toroidal energy density of the scalar field is a common feature of both real and complex scalar fields. In the next chapter, we will pay attention to the effects of the latter.

Chapter 4

A scalar field cloud in the center of the galaxy

The center of the Milky Way contains a very massive object (with mass of the order $10^6 M_\odot$) and all the studies conducted so far point to the possibility that such object is a BH [140]. Reaching this conclusion was mainly a result of an observational effort of a set of stars that populates that region of the galaxy – the S-stars – that culminated in the measurement of the gravitational redshift of one of those stars [141] – the S2 star.

The continuous tracking of the movement of the S2 star will provide information on the evolution of its orbit. Although the orbit is dominated by the presence of the SMBH, other structures that may exist in that region will perturb it and will leave an imprint on its evolution. In this chapter, we propose a scenario in which the central object of the galaxy is a SMBH that harbours a complex scalar field cloud; this structure, because it extends far away from the BH will be able to perturb the orbit of S2. The effects that we derive from this scenario can then be confronted with future data. The results presented in this chapter are based on Ref. [142].

4.1 Describing the effect of the scalar field

We will consider the scenario (already presented in Chapter 2) in which the scalar field cloud that develops around the SMBH in the center of the galaxy corresponds to a toroidal density distribution given by the scalar field function of Eq. (2.30) (notice that the variables are normalized by the BH's mass – Eq. (2.27))

$$\Psi = A_0 \mathrm{e}^{-\mathrm{i}(\omega_R t-\phi)} r\alpha^2 \mathrm{e}^{-\frac{r\alpha^2}{2}} \sin\theta. \tag{4.1}$$

To describe the gravitational potential that results from the presence of the scalar field cloud in a region far from the SMBH we solve the Poisson's equation

$$\nabla^2 U_{\rm sca} = -4\pi (M\mu)^2 |\Psi|^2. \tag{4.2}$$

Putting in the expression of Eq. (4.1) for the functional form of the scalar field function, one obtains

$$\nabla^2 U_{\rm sca} = -4\pi \left[\frac{M_{SC}}{M}\right] \left(\frac{\alpha^{10}}{64\pi} \mathrm{e}^{-\alpha^2 r} r^2 \sin^2\theta\right) \tag{4.3}$$

where we used

$$\alpha = M\mu. \tag{4.4}$$

To solve this equation we use the harmonic decomposition technique and we obtain an expression for the gravitational potential that can be written as (see Appendix A)

$$U_{\rm sca} = \Lambda \left[P_1(r) + P_2(r)\cos^2\theta\right] , \tag{4.5}$$

with $\Lambda = M_{SC}/M$ and

$$P_1(r) = \frac{16\alpha^4 r^2 + 48}{16\alpha^4 r^3} + \frac{e^{-\alpha^2 r}}{16\alpha^4 r^3}\Big[\alpha^{10}\left(-r^5\right) - 6\alpha^8 r^4 - 20\alpha^6 r^3 - 40\alpha^4 r^2 - 48\alpha^2 r - 48\Big] , \tag{4.6}$$

$$P_2(r) = -\frac{9}{\alpha^4 r^3} + \frac{e^{-\alpha^2 r}}{16\alpha^4 r^3}\Big[\alpha^{10} r^5 + 6\alpha^8 r^4 + 24\alpha^6 r^3 + 72\alpha^4 r^2 + 144\alpha^2 r + 144\Big]. \tag{4.7}$$

The equations of motion of the stars

Given that the BH has a much bigger mass than the S2-star, we will be focusing exclusively on the motion of the latter. The equations of motion governing the behavior of a faraway star around the BH surrounded by a scalar cloud are

$$\frac{d^2\boldsymbol{r}}{dt^2} = -\frac{\boldsymbol{r}}{r^3} + \Lambda\nabla\left[P_1(r) + P_2(r)\cos^2\theta\right] \tag{4.8}$$

where $\boldsymbol{r} = x\hat{e}_x + y\hat{e}_y + z\hat{e}_z$ is the normalized point-mass position vector with respect to the BH.

To advance with this exercise, we will assume that the presence of the field is subdominant in such a way that in the Newtonian regime (far away from the BH) the gravitational potential due to the scalar cloud can be considered as a perturbation to the Keplerian potential generated by the central BH. So, the presence of the scalar field will be treated as a perturbation of a Keplerian orbit.

4.2 Perturbing the orbit of S2

To obtain the effect of the presence of the scalar field on the orbit of the S2 star, we will have to use the Gauss equations (see Appendix D). In doing these calculations, we are assuming that the movement of the S2 star can be described by a perturbed Keplerian orbit. Being aware of the multitude of sources of perturbation, we assume also that all of them are additive and the effect of each one of them can be estimated independently.

4.2.1 Perturbing force due to the scalar cloud

The perturbing force that results from the presence of the scalar cloud is given by

$$\boldsymbol{F}_{\mathrm{pert}} = \Lambda\nabla\left[P_1(r) + P_2(r)\cos^2\theta\right] \tag{4.9}$$

and can be decomposed as (see Appendix D)

$$F_R/\Lambda = \sin^2(i)\sin^2(f+\omega)P_2'(r) + P_1'(r) \tag{4.10}$$

$$F_T/\Lambda = -\frac{\sin^2(i)(e\cos(f)+1)\sin(2(f+\omega))P_2(r)}{a\,(e^2-1)} \tag{4.11}$$

$$F_N/\Lambda = -\frac{\sin(2i)(e\cos(f)+1)\sin(f+\omega)P_2(r)}{a\,(e^2-1)} \tag{4.12}$$

where the prime $'$ stands for derivative with respect to the radial coordinate and F_R, F_T, F_N are the radial, transversal and normal (to the orbit) components of the perturbing force, respectively.

4.2.2 Collecting the orbital values of the S2 star

The framework we set up until now is developed in a reference frame which is centered in the BH and whose z-axis is aligned with the BH's spin direction. This means that we'll need the orbital parameters of the S2-star with respect to that reference frame. One can obtain them from the measured, Earth-based reference frame values in Ref. [141] by applying a set of rotations that relate the two frames (following the approach originally presented in Ref. [143] and reproduced in Appendix C). However, given the uncertainty in the orientation of the BH's spin, the aforementioned conversion is not well defined. Facing this problem, we decided to, in a first run of our calculations, use the orientation proposed by Ref. [143].

The orbital elements for the orbit of the S2 star in the re-scaled units of Eq. (2.27) read (see Ref. [141])

$$\begin{aligned} &a_0 = 2.5 \times 10^4, \quad e_0 = 0.88473, \quad i_0 = 133.817^{\circ} \\ &\omega_0 = 66.12^{\circ}, \quad \Omega_0 = 227.82^{\circ} \end{aligned} \tag{4.13}$$

which correspond, in the BH-centered reference frame defined in Ref. [143], to

$$\begin{aligned} &a_0 = 2.5 \times 10^4, \quad e_0 = 0.88473, \quad i_0 = 90.98^{\circ} \\ &\omega_0 = 81.60^{\circ}, \quad \Omega_0 = 254.191^{\circ} \end{aligned} \tag{4.14}$$

4.3 Calculating the variation of the orbital parameters

In this section, we are going to calculate the mean variation of the orbital parameters over a complete orbit. These variations will be related to the mass coupling parameter $\alpha = M\mu$ because the distribution of the scalar field density depends on that parameter. This is crucial given that one expects that the effects on the orbit of the star will depend on the position of the scalar-field cloud with respect to it.

4.3.1 Calculating the orbital parameter variations

Using Eqs. (D.9) to (D.14), one can calculate the average variation of the orbital parameters of S2 over one period. This calculation will uncover the magnitude of the effect and relate it to the parameters of the problem. We calculate it using the standard integral

$$\langle \Delta\kappa \rangle = \int_{f_0}^{f_0+2\pi} \frac{d\kappa}{dt}\frac{dt}{df'}df'. \tag{4.15}$$

where $\kappa \in \{a, e, i, \Omega, \omega, \mathcal{M}_0\}$[1] and dt/df' is obtained by inverting an embodiment of the Kepler equation

$$\frac{df}{dt} = \sqrt{\frac{1}{a^3}}\left(\frac{(1+e\cos f)^2}{(1-e^2)^{3/2}}\right). \tag{4.16}$$

Notice that the calculation of $\langle \Delta\kappa \rangle$ assumes that the variations in the orbital parameters are sufficiently slow for it to be justified to consider that the background values (i.e. the inital values of the orbital parameters) are a good approximation of the orbit along a whole period. Another important aspect is that the value of $\langle \Delta\kappa \rangle$ does not depend on the value of f_0. We calculate the integrand for each of the orbital parameters in the Appendix D.

[1]These are the orbital parameters that characterize an elliptical orbit (see appendix D).

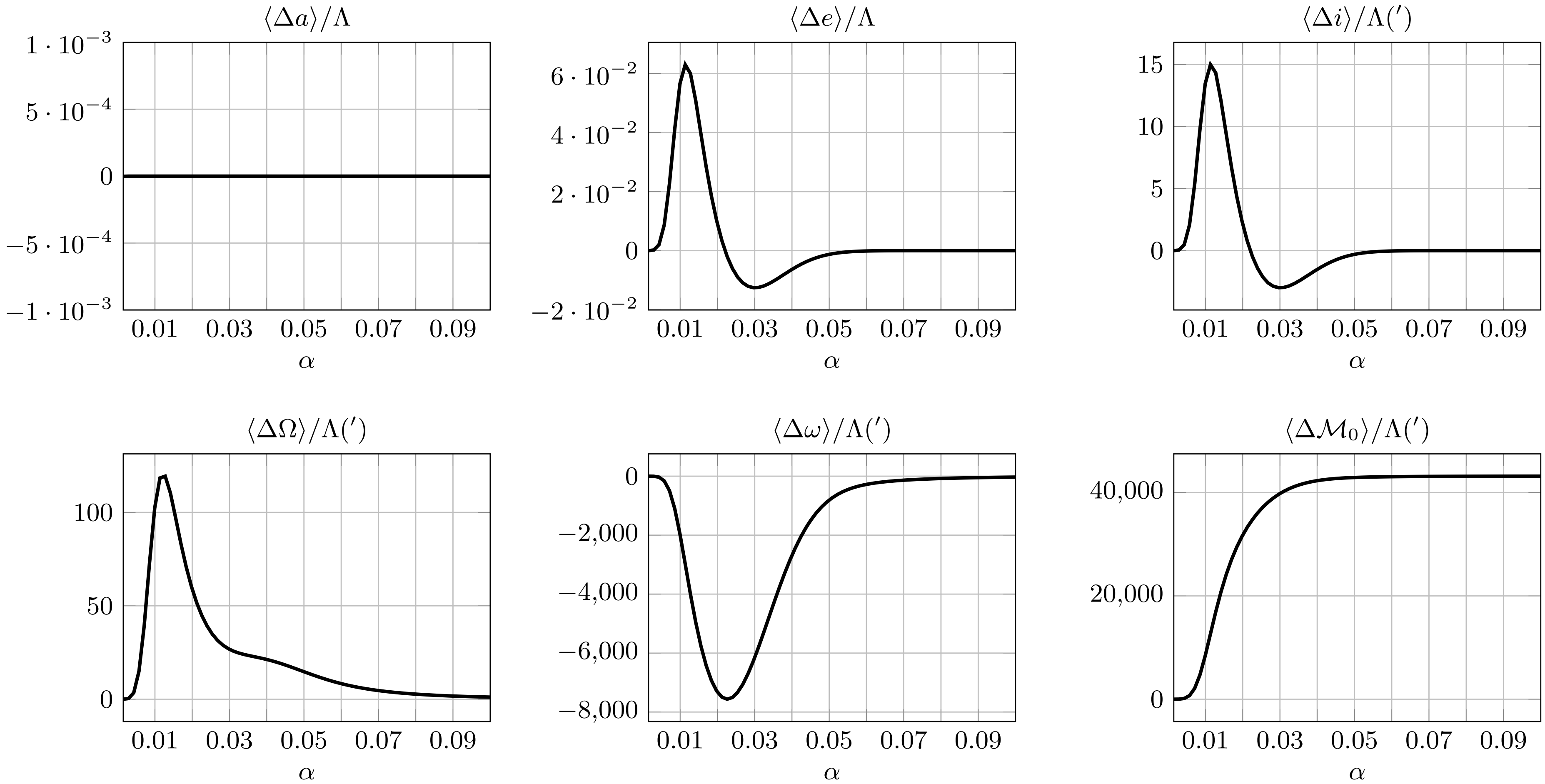

Figure 4.1: Using the orbital parameters in the BH-centered reference frame considering the spin orientation of the BH given by Ref. [143]. Notice that the angular elements are presented in arcminutes.

4.3.2 Using a fixed direction of the BH spin

From Appendix D, one can see that the derivatives of the functions $P_1(r)$ and $P_2(r)$ (the ones from Eqs. (4.6) and (4.7), respectively) only influence the radial force and that the function $P_1(r)$ does not participate in the calculations; we use those expressions in the integral of Eq. (4.15) and we are able to calculate the average value of variation of the orbital parameters as a function of the mass coupling parameter α. We present those results in Fig. 4.1 considering that the unperturbed orbit is described by the orbital parameters of Eq. (4.14). Notice that all plots show the values of the variation of the orbital parameters normalized by the parameter Λ; one verifies that:

1. The average variation of the semi-major axis $\langle\Delta a\rangle/\Lambda$ is negligible;

2. For values $\alpha \lesssim 0.001$ the effect of the scalar field cloud on the variation of all the orbital parameters is very small and only for bigger values one observes typical order of magnitude variations;

3. There's a maximum value of $\langle\Delta i\rangle/\Lambda$, $\langle\Delta e\rangle/\Lambda$ and $\langle\Delta\Omega\rangle/\Lambda$ and a minimum of $\langle\Delta\omega\rangle/\Lambda$. The maximum of the first three elements occurs for the same value of α - $\alpha \sim 0.012$ - while the minimum of $\langle\Delta\omega\rangle/\Lambda$ occurs for $\alpha \sim 0.022$.

4. The variations $\langle\Delta i\rangle/\Lambda$ and $\langle\Delta e\rangle/\Lambda$ may present a positive or negative variation depending on the mass of the scalar field. Their dependence on α is the same and for the value of $\alpha_0 \sim 0.022$ it is observed that $\langle\Delta i\rangle = \langle\Delta e\rangle = 0$ (notice that for the same value of α, $\langle\Delta\omega\rangle/\Lambda$ attains its minimum value) . For mass coupling parameters $\alpha > \alpha_0$, the variation of these elements is negative.

5. The angular parameters present variations with different orders of magnitude. The smallest is the variation of the inclination, then the longitude of the ascending node, the argument of the periapsis and the largest corresponds to the variation of the mean anomaly at epoch $\mathcal{M}_0$.

6. For all the elements κ for which $\langle\Delta\kappa\rangle \neq 0$, all but $\mathcal{M}_0$ tend to zero as the value of the coupling α increases. This connects with the point number (ii) and has to do with the dependence of the peak of the scalar-field cloud on the value of α. For values $\alpha \lesssim 0.001$ there isn't a variation of the parameters because the whole cloud is farther from the BH

than any part of the orbital trajectory of the star. As the value of α increases, the distance that separates the peak of the cloud from the central BH decreases and one observes variations in the orbital parameters up until the moment when the variations tend to zero again, in this case because for larger values of α the cloud is completely contained inside the orbit of the star. When this happens, the presence of the cloud won't change any of the geometrical parameters that characterize the orbit, but it produces a perturbing radial force that, on top of the main gravitational pull of the BH, will influence the dynamical variables of the orbit, particularly it will affect its mean motion. This effect on the mean motion will be translated in a constant variation of the mean anomaly at epoch for all values of α that correspond to cases in which the scalar cloud is completely inside the orbit.

In order to compare the scalar field cloud results with other predictions, we have to make an assumption on the value of the parameter Λ; we will make the very conservative assumption of $\Lambda = 0.001$, i.e., the mass of the scalar field cloud is 0.1% of the mass of the central BH in agreement with the $\sim 1\%$ upper limits of Ref. [141, 144]. Having established this, we will turn to the plots to obtain the following orders of magnitude

$$\begin{cases} \langle \Delta a \rangle \sim 10^{-10} \\ \langle \Delta e \rangle \sim \pm 10^{-5} \\ \langle \Delta i \rangle \sim \pm 0.001' \\ \langle \Delta \Omega \rangle \sim 0.01' \\ \langle \Delta \omega \rangle \sim -1' \\ \langle \Delta \mathcal{M}_0 \rangle \sim 20' \end{cases} . \tag{4.17}$$

4.3.3 Using other directions of the BH spin

Given the uncertainty in the orientation of the BH spin we can argue that the the orbital elements with respect to the BH-centered frame of reference, Eq. (4.14), cannot be considered with certainty either. This means that one should explore the range of values that one can assign to them. We point out that the calculation of $\langle \Delta\kappa \rangle$ does not depend on the orbital parameter Ω_0. So, we will focus only on i_0 and ω_0.

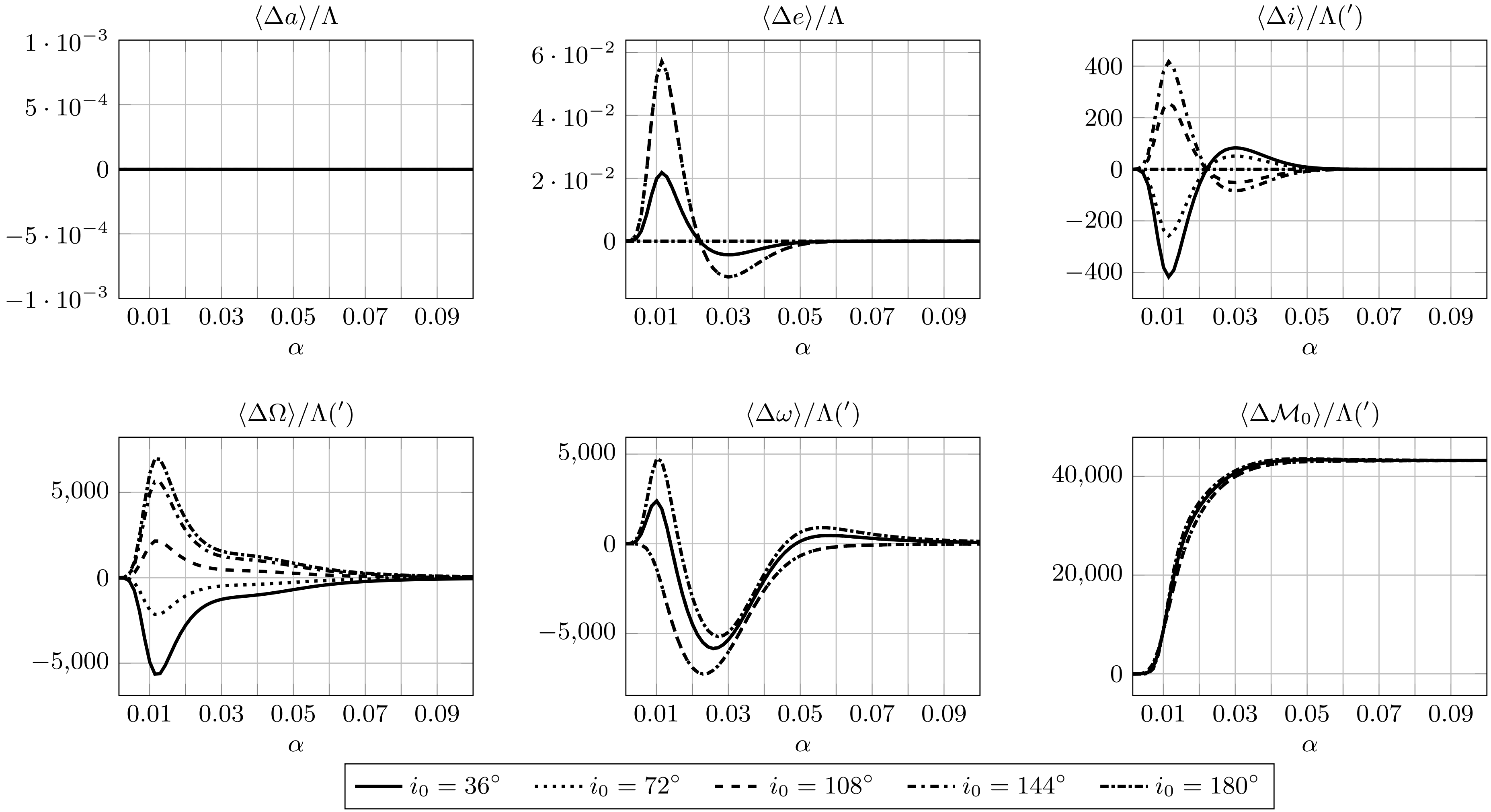

Figure 4.2: Using the orbital parameters in the BH-centered reference frame varying the value of the inclination i; all the other orbital parameters are equal to the ones used in Fig. 4.1

One can conclude, from observing the plots with the varying values of the inclination angle i and the argument of the periapsis ω, that the results are much more sensitive to the former than to the latter. There are, however, two points in common between the two cases: the variation of the semi-major axis remains negligible, such that one can say that $\langle a \rangle \approx 0$, and the variation of the mean anomaly at epoch is, to all purposes, unaffected by the different values of i and ω.

In Fig. 4.2, for different values of the initial inclination $i_0 \in]0, \pi[$, we observe a significant change in the profile of the relations $\Delta\kappa$ vs. α:

1. The variation of the eccentricity remains, similarly to the case of Fig. 4.1, negligible.

2. The variation of inclination and longitude of the ascending node are significantly affected by the inclination of the orbit. One can see that the profile of dependence of these two quantities on α changes both in order of magnitude and in sign. For instance, $\langle \Delta\omega \rangle / \Lambda$ is, independently of the value of α, always positive if $i_0 = 144°$ and always negative if $i_0 = 36°$;

3. We verify that for some values of the parameters α and value of i_0, the variation of ω is positive, which is not verified in Fig. 4.1. Besides this new feature, the order of magnitude of the effect does not change with respect to reference case.

A consequence of the uncertainty in the orbital parameter i_0 is the widening of the range of values for the variation of the orbital parameters due to the present of the scalar cloud. Assuming, again, that $\Lambda = 0.001$, the orders of magnitude for the variation of each of the orbital parameters can reach up to

$$\begin{cases} \langle \Delta a \rangle \sim 10^{-10} \\ \langle \Delta e \rangle \sim \pm 10^{-5} \\ \langle \Delta i \rangle \sim \pm 0.1' \\ \langle \Delta \Omega \rangle \sim \pm 1' \\ \langle \Delta \omega \rangle \sim \pm 1' \\ \langle \Delta \mathcal{M}_0 \rangle \sim 10' \end{cases} \tag{4.18}$$

depending on the value of the initial nclination i_0.

From Fig. 4.3, we observe a much weaker influence of such variation in the shape and order of magnitude of the profiles $\Delta\kappa$ vs. α:

1. One verifies that for some values of ω_0, the order of magnitude of the variation of the eccentricity can be bigger than that of Fig. 4.1. However, and given that Λ is expected to be small, one can conclude that no matter the actual value of ω_0, the contribution of the scalar cloud to the variation of the eccentricity will always be negligible;

2. The influence of the value of ω_0 to the variation $\langle \Delta i \rangle$ is significant because it can make it null;

3. With respect to the variations $\langle \Delta\Omega \rangle$ and $\langle \Delta\omega \rangle$, one observes that different values of ω_0 have no significant influence on them, except for slight supressions on the magnitude of these variations with respect to Fig. 4.1.

Different values of ω_0 do not introduce much change in the orders of magnitude of the potential effects of the scalar-field cloud on the orbital parameters of the orbit. In fact, an inspection of Fig. 4.3 is translated in

$$\begin{cases} \langle \Delta a \rangle \sim 10^{-10} \\ \langle \Delta e \rangle \sim \pm 10^{-4} \\ \langle \Delta i \rangle \sim \pm 0.01' \\ \langle \Delta \Omega \rangle \sim 0.01' \\ \langle \Delta \omega \rangle \sim -1' \\ \langle \Delta \mathcal{M}_0 \rangle \sim 10'. \end{cases} \tag{4.19}$$

which is very similar to the reference case of Fig. 4.1.

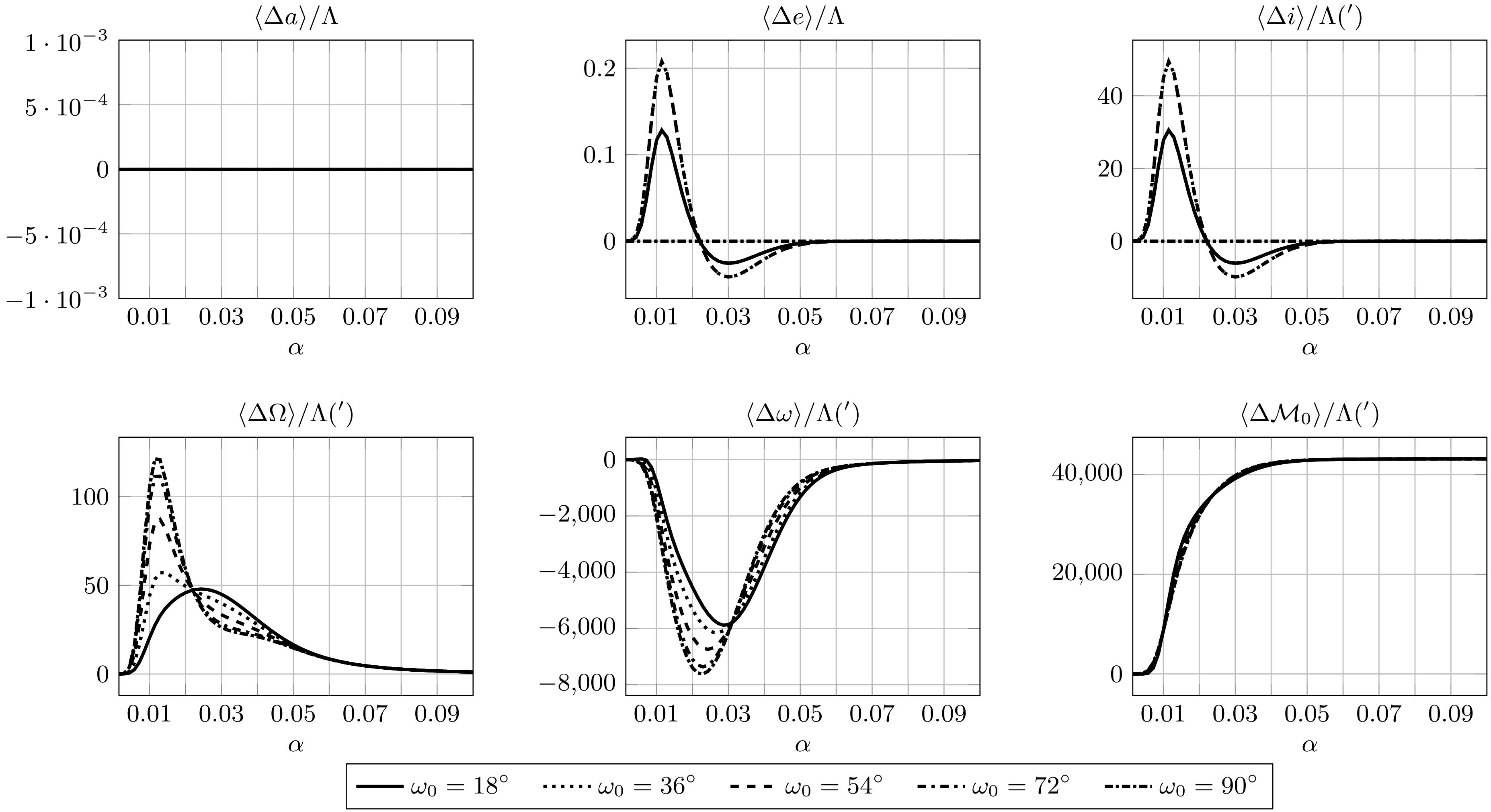

Figure 4.3: Using the orbital parameters in the BH-centered reference frame considering the inclination angle i_0 fixed and varying the value of the initial longitude of the periastron ω_0

4.3.4 The effective range of the mass coupling parameter

From the analysis of the results in Figs. 4.1,4.2 and 4.3, one can see that the values of the factor α that give rise to large variations of the orbital parameters are, approximately, in the range

$$0.001 \lesssim \alpha \lesssim 0.05, \tag{4.20}$$

which corresponds to (see Eq. (2.33))

$$1.2 \times 10^4 \lesssim R_{\text{peak}} \lesssim 3 \times 10^6. \tag{4.21}$$

This range of α is comparable with the orbital range of S2 ($3 \times 10^3 \lesssim r \lesssim 5 \times 10^4$) which means that, as expected, the dynamics of S2 is mostly altered when the orbit intersects the scalar field high density regions.

Moreover, this range of the mass coupling parameter can be translated in a scalar field mass parameter[2]

$$10^{-20}\ \text{eV}/c^2 < m_s < 10^{-18}\ \text{eV}/c^2. \tag{4.22}$$

4.4 Discussion

Given the exquisite agreement between the gravitational redshift predicted by GR and the one that was measured by Ref. [141], it is expected that the GR contributions will be the dominant effect determining the variation of the orbital elements of the stars in the center of the galaxy. However, with increasing capacity by the observational facilities, one can use the deviations from the GR-predicted values as a way of studying the central region of the galaxy.

The largest relativistic orbital effect is due to the static component of the first Post-Newtonian correction, which produces the advance of the periastron, given by, e.g., [146–148]

$$\langle \Delta\omega \rangle = \frac{6\pi}{a(1-e^2)} \sim 11.3'. \tag{4.23}$$

Compared with this, the contribution of the scalar-field cloud to $\langle \Delta\omega \rangle$, in our very conservative assumptions, may be large enough to be detected. However, the vast amount of other reasonable effects that will influence this value, can eclipse this contribution.

[2]For comparison, remember that the mass of the electron is approximately 0.5 MeV$/c^2$ and the upper bound on the photon's mass is 10^{-18} eV$/c^2$ ([145]).

In fact, as stressed by Ref. [146], second Post-Newtonian order effects, tidal distortions of the stars near the periastron or an extended distribution of mass inside the orbit of the star are expected to influence the amount of variation of the periastron longitude. Among them, the one that may compete more directly with the influence of the scalar cloud is an extended distribution of mass inside the orbit of the star.

Following the treatment of Refs. [147, 149, 150], one can calculate the average variation of the orbital parameters of the S2 star as a result of the presence of an extended, power-law, mass distribution of stars (characterized by a exponent γ) that generates a average potential (see Appendix E). Considering two extreme cases – a "light" and a "heavy" case corresponding, respectively, to two limits of the total mass of the extended mass distribution – for the light case, $\gamma = 1.5$, we obtain $\langle \Delta\omega \rangle \sim -1.37'$ and for the heavy case, $\gamma = 2.1$, we obtain $\langle \Delta\omega \rangle \sim -17.19'$. These results indicate that the effect of the galactic potential can be competitive with the first post-Newtonian correction with respect to the argument of the periastron. The other orbital elements are not affected by this distribution of mass, which makes them suitable to use as tests to constrain the parameters of the scalar cloud.

The distinguishing factor of the scalar-field cloud is its potentiality to affect the other orbital parameters besides the position of the periastron. So, only a complete assessment of all the orbital parameters of the S2-star can provide a satisfactory result with respect to the existence of such structure. For the other orbital parameters, the influence of the scalar-field structure will add, primarily, to the GR-predicted frame-dragging effects (see, e.g., Ref. [146]) which will depend on the magnitude and direction of the spin of the SMBH. One can have an estimation of these values by considering that the direction of the BH's spin maximizes the respective contributions, which are constrained from above by (see Ref. [151])

$$\langle \Delta i \rangle \lesssim \frac{4\pi\chi}{na^3(1-e^2)^{3/2}} \sim 0.1'\chi \tag{4.24}$$

$$\langle \Delta\Omega \rangle \lesssim \frac{4\pi\chi}{na^3(1-e^2)^{3/2}}\frac{1}{\sin i} \sim 0.1'\chi \tag{4.25}$$

where $\chi \equiv (c/G)(S_\bullet/M^2)$ is the dimensionless angular momentum parameter of the SMBH. We see that the variation of the inclination due to the scalar field cloud may be of the same order of magnitude of the frame-dragging effects. Moreover, due to the uncertainty associated with the direction of the BH's spin and the dependence of the inclination parameter i_0 in the BH's centered reference-frame, it is hard to fix a value for $\langle \Delta\Omega \rangle$, however, for non-extreme cases of the parameter i_0, the frame-dragging contribution may be of the same order of the scalar-field one. Although naive, these estimates show that the presence of a scalar-field cloud in the vicinity of the SMBH in the center of the galaxy may be detectable through the deviations of the variations of the orbital parameters with respect to the GR-predicted values.

The other S-stars have semi-major axis values in the same order of magnitude as the S2-star. This means that a scalar cloud that affects the latter will also affect the other S-stars. Summing to this the fact that the other S-stars have different angular orbital parameters and the fact that, according to Fig. 4.2, the value of the inclination of the orbit can produce a big change in the order of magnitude of the variation of the orbital parameters, a careful study of all the S-stars will be a robust test on the hypothesis of the scalar-field cloud. Indeed, since the orientation of the orbits of the S-stars is so diverse, the effect of the cloud on each one of them would be different and that difference could be, having a big enough number of measurements, traced back to the nature of the scalar-field cloud.

Chapter 5

Reaction of a scalar-field structure to an orbiting particle

We consider the scenario in which a low-energy, stable, complex scalar field configuration of the Einstein-Klein Gordon system is perturbed by a pointlike mass. This two-component system will be evolved separately and the only interaction between the components is gravitational. The time evolution of the low-energy scalar structure will be described by the Schrodinger-Poisson (SP) system, which will contain the effect of the presence of the point-particle, whereas the movement of the point-particle will be rendered from the gravitational potential of the scalar field configuration by the laws of Newtonian mechanics. This chapter is based in the work of Ref. [152].

5.1 Describing the setup

From Section 2.2, we saw that in the weak-field limit, a spherically-symmetric complex scalar field function can be written as

$$\Psi = \mathrm{e}^{-\mathrm{i}\mu t}\psi(t,r). \tag{5.1}$$

and its dynamics is governed by the SP system

$$\begin{cases} \mathrm{i}\partial_t\psi & = -\frac{1}{2\mu}\nabla^2\psi + \mu U\psi \\ \nabla^2 U & = -4\pi\mu^2\left|\psi\right|^2 \end{cases}. \tag{5.2}$$

Using the typical rescalling of variables,

$$t \to \mu t, \quad r \to \mu r, \quad \psi \to \frac{1}{\sqrt{4\pi}}\psi\,, \tag{5.3}$$

the SP system is written as

$$\begin{aligned} \mathrm{i}\partial_t\psi =& -\frac{1}{2}\nabla^2\psi + U\psi, \\ \nabla^2 U =& \psi\psi^*. \end{aligned} \tag{5.4}$$

It is known [51] that a transformation of the form

$$(t, r, U, \psi) \to (\lambda^{-2}\hat{t}, \lambda^{-1}\hat{r}, \lambda^2\hat{U}, \lambda^2\hat{\psi}), \tag{5.5}$$

leaves the SP system of equations unchanged. Using this property, one can normalize the system by working only with the "hat-variables", meaning that the order of magnitude of all the quantities involved in this problem is hidden in the parameter λ. Notice that Ref. [54] fixes the value of λ for which the behavior described by the SP sytem coincides with the behavior of the Einstein-Klein-Gordon system (i.e. the scale of the low-energy limit)

$$\lambda^2 < 10^{-3}\,. \tag{5.6}$$

This is the limit of validity of all the statements that stem from the analysis of the SP system: these calculations only cover scalar fields whose magnitude is compatible with the previous limit. So, having established the limits of validity of our working system, we will, from now on and unless otherwise stated, work in terms of the "hat-quantities" of Eq. (5.5).

5.1.1 Stationary solutions in the weak-field limit

To find the stationary, spherically symmetric, ground state solutions of the SP system, we follow the same technique used with the EKG system: we consider a scalar field of the form

$$\psi = \exp(-\mathrm{i}\gamma t) f(r), \tag{5.7}$$

i.e. γ is the difference between the total energy of the field and its rest energy (notice that ψ corresponds to the slow-varying part of the scalar field, the total scalar field function being $\Psi \sim \exp(-\mathrm{i}m_s t)\exp(-\mathrm{i}\gamma t)f(r)$; thus, its energy is $E = m_s + \gamma$)[1] and since stationary configurations are bound states of the system, one expects[2] that $\gamma < 0$. By substituting the previous ansatz on the SP system, one obtains

$$f''(r) + \frac{2}{r}f'(r) + 2(\gamma - U(r))f(r) = 0\,, \qquad (5.8)$$
$$U''(r) + \frac{2}{r}U'(r) = f(r)f^*(r)\,.$$

These equations are used to find the profiles $f(r)$ of the stationary configurations of the scalar field. To do it, one has to impose boundary conditions that come from two reasonable physical requirements: the profile has to be regular and finite. Regularity is enforced by demanding that $f'(r)$ and $U'(r)$ are zero in the origin; finiteness is then guaranteed by insisting that $\lim_{r\to\infty} f(r) = 0$. Moreover, one must demand that the resulting gravitational potential $U(r)$, when measured at infinity, describes, as it should, the effect of the total mass of the scalar field configuration.

To calculate the total mass, we will use the fact that we're working in the Newtonian limit and use a volume integral

$$M_{\mathrm{SC}} = \int \rho(t,r)dV\,, \qquad (5.9)$$

where $\rho = \mu^2\Psi\Psi^*$ is the leading order term of the the weak-field limit of the 00 component of the scalar field energy-momentum tensor. Writing the previous integral in terms of the hat-quantities of Eq. (5.5), we obtain $M_{\mathrm{SC}} = M_f/\mu$ where

$$M_f = \int \rho_f(t,r)dV = \frac{1}{4\pi}\int \psi\psi^* dV\,, \qquad (5.10)$$

which in the case of the stationary configuration, can be simplified to

$$M_f = \frac{1}{4\pi}\int_0^\infty \psi^*\psi dV = \int_0^\infty f(r)f^*(r)r^2 dr\,. \qquad (5.11)$$

[1] In the low-energy limit this difference is very small. Moreover, since we are working with the "hat-quantities" (see Eq. (5.5)), the value of γ that we present in the equations is related with that normalized system of coordinates; to convert it back to Planck units, one has to multiply it by λ^2, which will consistently make it small

[2] Using the non-scaled variables, one can see that see that $\frac{\gamma}{\mu} = \frac{\omega}{\mu} - 1$, and because the bound state condition is $\frac{\omega}{\mu} < 1$, a bound state must have $\frac{\gamma}{\mu} < 0$.

Having calculated the mass, one can write the boundary behavior for the gravitational potential in the hat-quantities as

$$\lim_{r\to\infty} U(r) = -\frac{M_f}{r}. \tag{5.12}$$

Imposing these conditions along with the value for the scalar field at the origin which, since we are working with the normalized "hat quantities" can be $f(0) = 1$, one obtains, numerically, a profile for $f(r)$. To this profile corresponds a unique value of the quantities γ and $U(r = 0)$. Since we are only interested in the 0-node, ground state solutions, we quote here only its characteristic values,

$$\begin{aligned} \gamma &= -0.6922, \quad U(0) = -1.3418, \\ M_f &= 2.0622, \quad R_{99} = 4.8228\,, \end{aligned} \tag{5.13}$$

where R_{99} is the radial position up to which 99% of the mass of the scalar configuration is contained.

5.1.2 The point-like particle

We now want to understand how an orbiting mass M_p disturbs, dynamically, the previous self-gravitating massive scalar structure. We model the orbiting mass as pointlike particle [3] and use its energy-momentum tensor in the Einstein-Klein-Gordon system (see section 6.5 of Ref. [153])

$$T_P^{\mu\nu} = \frac{1}{\sqrt{-g}} M_p \int \frac{dx_P^\mu}{d\tau}\frac{dx_P^\nu}{d\tau}\delta^{(4)}(x^\alpha - x_P^\alpha(\tau))\mathrm{d}\tau\,, \tag{5.14}$$

where x_P^α are the spacetime coordinates of the point-particle, τ is its proper-time and $\delta^{(4)}$ is the Dirac-delta. A low-energy analysis of the Einstein-Klein-Gordon system with the pointlike mass included yields (see Appendix A)

$$\begin{aligned} \mathrm{i}\partial_t\psi &= -\frac{1}{2}\nabla^2\psi + U\psi\,, \\ \nabla^2 U &= \psi\psi^* + P(\boldsymbol{x}, \boldsymbol{x}_P)\,, \end{aligned} \tag{5.15}$$

with

$$P(\boldsymbol{x}, \boldsymbol{x}_P) = \frac{4\pi M_P}{r^2}\delta(r - r_P)\delta(\cos\theta - \cos\theta_P)\delta(\phi - \phi_P)\,, \tag{5.16}$$

[3] Due to the nonlinear nature of Einstein's field equations, problems arise in the definition of point particles in such context. However, we will always be working in the Newtonian limit where such idealization is acceptable.

where r_P, θ_P and ϕ_P correspond to the spherical coordinates indicating the position of the point-like particle. Notice that since we are using the "hat quantities" of Eq. (5.5), the value of the mass of the orbiting particle, M_p, when converted to Planck units, must also be multiplied by μ. Using the spherical harmonics closure relation [154]

$$\delta(\cos\theta - \cos\theta_P)\delta(\phi - \phi_P) = \sum_{\ell m} Y^*_{\ell m}(\theta_P, \phi_P) Y_{\ell m}(\theta, \phi)\,, \tag{5.17}$$

Eq. (5.16) can be re-written as a sum of spherical harmonics

$$P(\boldsymbol{x}, \boldsymbol{x}_P) = p_A(r, \boldsymbol{x}_P) + \sum_{\ell,m} p_{\ell,m}(r, \boldsymbol{x}_P) Y_{\ell m}(\theta, \phi)\,, \tag{5.18}$$

where

$$p_A(r, \boldsymbol{x}_P) = \frac{M_P \delta(r - r_P)}{r^2}, \tag{5.19}$$

$$p_{\ell,m}(r, \boldsymbol{x}_P) = \frac{4\pi M_P \delta(r - r_P)}{r^2} Y^*_{\ell m}(\theta_P, \phi_P), \tag{5.20}$$

This expansion motivates us to write the other quantities involved in the problem in a similar way, i.e.

$$\psi(r, \theta, \phi) = \varphi_A(r) + \sum_{\ell,m} \varphi_{\ell,m}(r) Y_{\ell m}(\theta, \phi), \tag{5.21}$$

$$U(r, \theta, \phi) = V_A(r) + \sum_{\ell,m} V_{\ell,m}(r) Y_{\ell m}(\theta, \phi). \tag{5.22}$$

5.1.3 The evolution equations

When the pointlike particle is put in orbit, both the scalar field and the gravitational potential will, in general, develop a multipolar strucuture which will translate in the development of non-trivial profiles for the (ℓ, m) components of the expansions of Eqs. (5.21) and (5.22). This development will be coordinated by the SP system of equations, where we introduce the aforementioned expressions for the scalar field and gravitational potential, which are then projected in each (ℓ, m) component. By doing that, we obtain two equations for each mode, one for $\varphi_{\ell,m}$, coming from the projection of the Schrodinger equation, and one for $V_{\ell,m}$ coming from the projection of the Poisson equation. Particularly, in order to harvest the zeroth order component (which we indicate with "A") we integrate both sides of it over the whole sphere and we obtain

$$\begin{cases} \partial_t \varphi_A &= \frac{\mathrm{i}}{2}\nabla_r^2 \varphi_A - \mathrm{i}\int \mathrm{d}\Omega[U\psi] \\ \nabla_r^2 V_A &= p_A + \int \mathrm{d}\Omega[\psi\psi^*] \end{cases}, \tag{5.23}$$

where $d\Omega = \sin\theta d\phi d\theta$ and $\nabla_r^2 \equiv \frac{\partial^2}{\partial r^2} + \frac{2}{r}\frac{\partial}{\partial r}$. To obtain the equations corresponding to a general (ℓ, m) mode we integrate each side of the equations multiplied by the corresponding spherical harmonic function and we obtain

$$\begin{cases} \partial_t \varphi_{\ell,m} = \frac{\mathrm{i}}{2}\left(\nabla_r^2 - \frac{\ell(\ell+1)}{r^2}\right)\varphi_{\ell,m} - \mathrm{i}\int \mathrm{d}\Omega[U\psi]Y^*_{\ell,m} \\ \left(\nabla_r^2 - \frac{\ell(\ell+1)}{r^2}\right)V_{\ell,m} = p_{\ell,m} + \int \mathrm{d}\Omega[\psi\psi^*]Y^*_{\ell,m} \end{cases}. \tag{5.24}$$

5.2 Running the simulation

In order to study the evolution of our two body system we evolve the SP-equations for each (ℓ, m) mode to account for the scalar field structure, along with the equations of motion of the point particle, which are given by Newton's laws of motion (see Appendix F for the numerical details). This is accomplished with the following algorithm:

1. Given the initial conditions, calculate the gravitational potential of the "scalar field + particle" system using a sparse matrix solver included in SciPy [155];

2. From $t = 0$ to $t = \Delta t$, use the iterated Crank-Nicolson method [156] to advance the scalar field and the Euler's method [157] to advance the position and velocity of the particle;

3. Calculate the gravitational potential of the "scalar field + particle" system using a sparse matrix solver;

4. From $t = \Delta t$ to $t = 2\Delta t$, use the iterated Crank-Nicolson method to advance the scalar field and the two-step Adams-Bashforth [157] method to advance the position and velocity of the particle;

5. Repeat the former and the latter steps until $t = 700$.

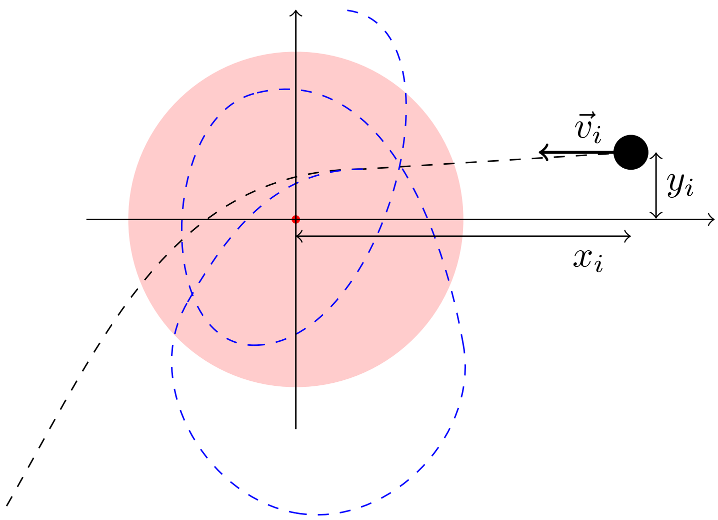

Figure 5.1: Pictorial description of the different outcomes of throwing a pointlike particle at a scalar, self-gravitating structure. We expect that the particle with initial conditions $\boldsymbol{r}_i = (x_i, y_i)$, $\boldsymbol{v}_i = (-v_i, 0)$, being thrown towards the center of the oscillaton, either scatters (schematically represented in dashed black) or stays in a bounded orbit (in dashed blue).

5.2.1 The initial conditions

At $t = 0$, the scalar field is given by the ground-state, 0-node, stable configuration described in Eq. (5.13). The point particle's degrees of freedom are its initial position and velocity. We performed several simulations to study the influence of varying these parameters on the evolution of the system. In each simulation, the initial condition for the field and the gravitational potential are

$$\begin{gathered}\varphi_A(t=0) = f_E(r)\,, \qquad V_A(t=0) = U_E(r)\,, \\ \varphi_{\ell,m}(t=0) = 0\,, \qquad V_{\ell,m}(t=0) = 0\,,\end{gathered} \tag{5.25}$$

where f_E and U_E are given by the 0-node solutions of Eq. (5.8). The point particle will be thrown at the scalar self-gravitating structure, a setup characterized by (see Fig. 5.1),

1. the impact parameter y_i,
2. the mass M_P of the particle being thrown,
3. the velocity v_i with which the particle is thrown.

To write the initial conditions of this motion, we consider the plane that contains the position and velocity vectors of the particle (for all purposes it can be the $\theta = \pi/2$ plane). In this plane, we put the center of coordinates in the center of the scalar field structure, we use (x_i, y_i) to indicate the initial position of the perturbing particle and $(-v_i, 0)$ to indicate its initial velocity. Then, we can obtain the initial conditions in polar coordinates of the plane (see Fig. 5.1):

$$r_i = \sqrt{x_i^2 + y_i^2}, \quad \phi_i = \arctan\left(\frac{y_i}{x_i}\right), \tag{5.26}$$

$$\dot{r}_i = -v_i \cos\phi_i, \quad \dot{\phi}_i = \frac{v_i}{r_i}\sin\phi_i. \tag{5.27}$$

We run 27 simulations, spanning the following set of initial conditions

$$x_i = 8, \quad y_i \in \{1.0, 3.0, 5.0\}, \tag{5.28}$$

$$v_i \in \{0.3, 0.5, 0.7\}, \quad M_p \in \{0.1, 0.001, 10^{-5}\}. \tag{5.29}$$

To make it easier to refer to each simulation, we assign a unique code to each of them. The first character of the code refers to the mass of the particle – "L", "M" or "S", i.e., large, medium or small – for, respectively, $M_p = 0.1, 10^{-3}$ or 10^{-5}; the remaining characters will indicate explicitly the impact parameter y_i and the initial velocity v_i. As an example, the simulation that has as initial conditions $y_i = 1.0, v_i = 0.3, M_P = 0.1$ is called "simulation $\mathbf{L}Y1V03$".

We also run 9 simulations in which we evolve the equations of motion of the particle and the SP-system side-by-side without considering the effect of the particle on the scalar field. We will call these the "control tests" and we will refer to them with a similar code indicating the impact parameter and the initial velocity. So, the "control test" that has as initial conditions $y_i = 1.0, v_i = 0.3$ is referred to by "control test $Y1V03$".

5.2.2 The boundary conditions of the SP-system

Regarding the scalar field components, we demand regularity at the boundaries of all quantities. At the origin, regularity is guaranteed by fixing $\varphi'_A(0) = \varphi_{\ell,m}(0) = \varphi'_{\ell,m}(0) = 0$ and $U'(0) = 0$. To treat the boundary condition at infinity, we benefit from the careful analysis made in Ref. [51]. The authors show that in order to treat spatial infinity in this system, one must either put it far enough from the active zone or add a sponge to the simulation so that no reflections at the infinity boundary occur. We choose the first option. All the runs of our code were made with a spatial grid that extends up to $r = 1000$ (in the agreed units). We consider that at the infinity boundary all components of the scalar field and of the potential are zero except the spherical component of the potential, V_A. In fact, as the mass of the scalar field structure has to be conserved in the grid, we impose that $V_A(r = 1000) = -M_f/1000$, where M_f is given in Eq. (5.13).

5.2.3 Time and space discretization of the system

We tested the code – with results that can be seen in Appendix F – and based on that we decided to conduct all the simulations using a spatial grid of $\Delta r = 0.1$ and time step of $\Delta t = 10^{-3}$.

5.3 Results

In the simulations of the "scalar field + particle" system, the evolution of both components encodes information about the whole system. We will show details regarding the movement of the particle and the struture of the scalar field configuration as a function of time. Particularly, we will analyse how the backreactions of the field affect the movement of the particle and how the non-spherical components of the field evolve.

5.3.1 General evolution of the field

We verified that in the simulations we ran, the description of all the quantities involved – the scalar field, the gravitational potential, and the trajectory of the point-particle – were dominated by the $\ell = 0$ and $\ell = 1$ terms of the expansions in Eqs. (5.21) and (5.22). Particularly, we verify that for the cases with particle mass given by $M_p = 10^{-3}$ and $M_p = 10^{-5}$ the terms $\ell \geq 2$ are completely negligible, whereas for the case with $M_p = 0.1$, we verify that $\max[|\varphi_{2,m}|/|\varphi_{1,m}|] \sim \max[|V_{2,m}|/|V_{1,m}|] \sim \mathcal{O}(10^{-2})$, which is the upper bound for any other ratio of the form $\max[|\varphi_{\ell+1,m}|/|\varphi_{\ell,m}|]$ or $\max[|V_{\ell+1,m}|/|V_{\ell,m}|]$, for $\ell > 1$ in the $M_p = 0.1$ case. The latter fact is translated in a slight change in the numerical values of some of the quantities that are calculated in what follows. However, since our focus will be on orders of magnitude and not in exact numerical values, we will, for the sake of simplicity and economy in the length of the expressions, use throughout this section a truncated series to describe the meaningful quantities, i.e.,

$$\psi(r,\theta,\phi) = \varphi_A(r) + \sum_{m=-1}^{1} \varphi_{1,m}(r) Y_{1m}(\theta,\phi), \tag{5.30}$$

$$U(r,\theta,\phi) = V_A(r) + \sum_{m=-1}^{1} V_{1,m}(r) Y_{1m}(\theta,\phi). \tag{5.31}$$

Notice that the term $m = 0$ isn't considered in this expansion. This is due to the fact that the orbital plane is taken to be $\theta = \pi/2$ (see Section 5.2.1), and so the $m = 0$ components are identically zero.

5.3.2 Effects on the orbiting particle

The set of initial conditions of the orbiting particle (see Section 5.2.1), gives rise to *bounded and unbounded orbits of the equilibrium scalar field structure*. Technically, an unbounded orbit has energy per unit mass,

$$\varepsilon = \frac{1}{2}\left(\dot{r}^2 + r^2\dot{\phi}^2\right) - U_E(r)\,, \tag{5.32}$$

larger than zero. In such case the expression

$$\dot{r}^2 = 2\varepsilon - U_{\text{eff}}\,, \tag{5.33}$$

is always non-negative, where U_{eff} is given by

$$U_{\text{eff}} = \frac{\mathcal{L}}{r^2} - 2U_E(r)\,, \tag{5.34}$$

for initial angular momentum per unit mass[4] $\mathcal{L}$. In our case, however, whenever we say that an orbit is unbounded, we simply mean that the apoastron of the orbit wasn't observed in the grid during the whole simulation time. In this sense, we find that all simulations result in bounded orbits except **M**$Y1V07$, **S**$Y1V07$, $Y1V07$, **M**$Y3V07$, **S**$Y3V07$, $Y3V07$, **L**$Y5V07$, **M**$Y5V07$, **S**$Y5V07$ and $Y5V07$. Notice that all the unbounded orbits correspond to initial velocity $v_i = 0.7$ and that for the cases $y_i = 1.0, 3.0$ the control test is unbounded whereas the corresponding simulation with $M_P = 0.1$ is bounded. These cases show that the reaction of the scalar field to the presence of the massive particle alters significantly its trajectory.

[4]This classification is valid for the equilibrium configuration, in which angular momentum is conserved.

Friction force

The backreaction of the scalar configuration on the motion of the particle can be computed through the calculation of the effective force that appears in the movement of the particle as it travels through the scalar cloud. We call this a "friction force". To calculate it, we employ two different methods. The first method is to compare the acceleration vector in the orbital plane of the simulations with backreactions (indicated by the subscript "sim") with the respective "control tests"[5] (indicated by the subscript "control"), i.e.

$$\boldsymbol{F}_{\rm f} = \boldsymbol{F}_{\rm sim} - \boldsymbol{F}_{\rm control}\,, \tag{5.35}$$

with $\boldsymbol{F}_{\rm control} = M_p \boldsymbol{a}_{\rm control}$ (same thing for "sim" component); the acceleration vector is written as

$$\boldsymbol{a} = \left[\frac{d^2 r}{dt^2} - r\left(\frac{d\phi}{dt}\right)^2\right]\hat{r} + \left[r\frac{d^2\phi}{dt^2} + 2\frac{dr}{dt}\frac{d\phi}{dt}\right]\hat{\phi}\,. \tag{5.36}$$

So, we will write

$$\left(\frac{\boldsymbol{F}_{\rm f}}{M_P} \equiv\right) \boldsymbol{f}_{\rm f} = \boldsymbol{a}_{\rm sim} - \boldsymbol{a}_{\rm control}\,. \tag{5.37}$$

The other method of quantifying this friction force is through the gravitational potential function

$$\boldsymbol{f}_f = -\nabla U_{\rm sim}(r,\phi) + \nabla U_{\rm control}(r), \tag{5.38}$$

where U represents the gravitational potential. The difference between the two should reflect the extra force that appears as a finite mass effect. The gravitational potential in Eq. (5.31) can be written as[6]

$$U = V_A(r) + 2\sqrt{\frac{3}{8\pi}}\sin\theta\Big(R(r)\cos\phi + I(r)\sin\phi\Big), \tag{5.39}$$

[5] Remember the classification introduced in subsection 5.2.1

[6] We verify that the source terms of the Poisson equation for the $\ell = 1$ components of the gravitational potential – see Eq. (5.22) –, given by $s_{1,\pm1} = \int\int(\psi\psi^* + p_{1,\pm1}Y_{1,\pm1})Y^*_{1,\pm1}\sin\theta{\rm d}\theta{\rm d}\phi$ where $p_{1,\pm1}$ comes from the point-particle contribution (see Eqs. (5.15) and (5.18)), satisfy the following identity $(s_{1,-1} + s^*_{1,-1}) = -(s_{1,1} + s^*_{1,1})$ and $(s_{1,-1} - s^*_{1,-1}) = (s_{1,1} - s^*_{1,1})$, which means that ${\rm Re}[s_{1,1}] = -{\rm Re}[s_{1,-1}]$ and ${\rm Im}[s_{1,1}] = {\rm Im}[s_{1,-1}]$. This relation between the real and imaginary parts of the source terms allows us to write $V_{1,-1} = R(r) + {\rm i}I(r)$ and $V_{1,1} = -V^*_{1,-1}$.

where $R \equiv \mathrm{Re}[V_{1,-1}]$ and $I \equiv \mathrm{Im}[V_{1,-1}]$. In the plane of motion, which we consider to be $\theta = \pi/2$, we can write $\boldsymbol{f}_f$ as

$$\boldsymbol{f}_f = -\left[\frac{\partial V_{\mathrm{Asim}}}{\partial r} - \frac{\partial V_{\mathrm{Acontrol}}}{\partial r} + 2\sqrt{\frac{3}{8\pi}}\left(\frac{\partial R(r)}{\partial r}\cos\phi + \frac{\partial I(r)}{\partial r}\sin\phi\right)\right]\hat{r} - \\ - \frac{2}{r}\left[\sqrt{\frac{3}{8\pi}}\Big(-R(r)\sin\phi + I(r)\cos\phi\Big)\right]\hat{\phi}. \tag{5.40}$$

Using both methods to assess the friction force, we calculate the quantity

$$\langle \boldsymbol{f}_{\mathrm{f}} \rangle = \frac{1}{t_{\mathrm{out}} - t_{\mathrm{in}}} \int_{t_{\mathrm{in}}}^{t_{\mathrm{out}}} \boldsymbol{f}_{\mathrm{f}}\, \mathrm{d}t, \tag{5.41}$$

where $t_{\mathrm{in}}, t_{\mathrm{out}}$ are, respectively, the time in which the particle penetrated and left the scalar field structure for the first time. In order to understand the influence of each of the parameters on the movement of the particle, we run tests in groups of simulations where only one of the parameters is changing:

1. same mass and initial velocity: MV1 = $\{\mathbf{L}Y1V07, \mathbf{L}Y3V07, \mathbf{L}Y5V07\}$, MV2 = $\{\mathbf{M}Y1V05, \mathbf{M}Y3V05, \mathbf{M}Y5V05\}$;

2. same mass and impact parameter: MI1 = $\{\mathbf{L}Y1V03, \mathbf{L}Y1V05, \mathbf{L}Y1V07\}$, MI2 = $\{\mathbf{M}Y1V03, \mathbf{M}Y1V05, \mathbf{M}Y1V07\}$;

3. same velocity and impact parameter: VI1 = $\{\mathbf{L}Y1V07, \mathbf{M}Y1V07, \mathbf{S}Y1V07\}$, VI2 = $\{\mathbf{L}Y1V05, \mathbf{M}Y1V05, \mathbf{S}Y1V05\}$.

One can make three comments on the results of this exercise. The first comment is that the two methods to calculate the friction force give, as expected, the same results. The second has to do with the direction of the average force. We obtain that the average friction force has negative components in both planar directions. The third, and final, comment is that the mass is the factor that influences the most the magnitude of the friction force[7]. As can be seen in Fig. 5.2, the variation of the initial velocity v_i and the impact parameter y_i does not affect significantly the order of magnitude of the friction force, whereas one can see a systematic and clear variation

[7]This is not surprising in our context given that the range of variation of the value of the mass is much bigger than the one of the other two parameters. We can say that we are conditioned by the size of the scalar field structure. If the impact parameter and/or the velocity are too big or too small the simulations won't work properly either because the particle wouldn't spend enough time close to the scalar field structure or because it would pass too far from it in such a way that the interaction wouldn't produce measurable effects.

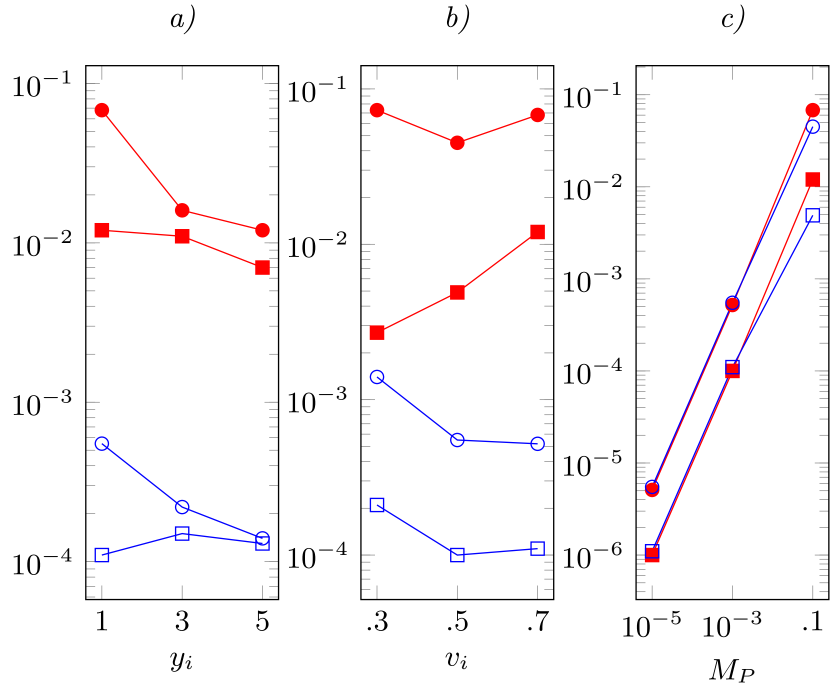

Figure 5.2: Representing $-\langle f_{\rm f}^r \rangle$ (by $\bullet$ or $\circ$) and $-\langle f_{\rm f}^\phi \rangle$ (by $\blacksquare$ or $\square$) for different sets of simulations. In panel a), MV1, MV2, i.e. mass and velocity are kept constant; red, filled points represent $M_P = 0.1, v_i = 0.7$ and blue, hollow points represent $M_P = 0.001, v_i = 0.5$. In panel b) MI1, MI2 i.e. mass and impact parameter are kept constant; red, filled points represent $M_P = 0.1, y_i = 1.0$ and blue, hollow points represent $M_P = 0.001, y_i = 1.0$. In panel c) VI1, VI2 i.e. velocity and impact parameter are kept constant; red, filled points represent $v_i = 0.7, y_i = 1.0$ and blue, hollow points represent $v_i = 0.5, y_i = 1.0$

of this value as one changes the value of the mass of the particle. Specifically, one verifies that

$$- \langle f_{\mathrm{f}}^{r} \rangle \sim \alpha_r M_P, \quad - \left\langle f_{\mathrm{f}}^{\phi} \right\rangle \sim \alpha_\phi M_P, \tag{5.42}$$

where α_r depends on the initial velocity and the impact parameter, while α_ϕ almost doesn't depend on those parameters, presenting a value of the order 10^{-1} in all instances. The dependence of α_r in the y_i and v_i parameters is asymmetrical: the variation of the initial velocity doesn't affect significantly its value – the order of magnitude does not change – whereas the bigger the impact parameter the smaller is the order of magnitude of the coefficient. In fact, while for cases in which $y_i = 1, 3$ we verify $\alpha_r \sim \mathcal{O}(1)$ for $y_i = 5$ we observe $\alpha_r \sim \mathcal{O}(10^{-1})$. This comes as no surprise since the bigger the impact parameter the farther from the center of the scalar structure the particle will pass which means that the particle crosses regions where the scalar field is more and more diluted, decreasing the value of the friction force. Moreover, since the value we are calculating corresponds to a force per unit mass, which by the relations of Eq. (5.42) is proportional to the mass of the incoming particle, we conclude that the total force $\boldsymbol{F}$ scales as the square of the incoming particle M_p. This is not a new result (see, for instance, [158]), but provides a connection between our study and the study of the drag force in self-interacting media.

Loss of angular momentum

Another way to describe the effect of the interaction between the orbiting particle and the scalar field is to study the angular momentum of the former. We don't use the energy because the energy depends on the gravitational potential which in our scenario is dynamical and so it doesn't provide a good measure to characterize the movement of the orbiting particle. The angular momentum, however, is a good measure in the sense that it depends only on kinematic variables. Having said that, we are going to study the quantity

$$\Delta\mathcal{L} = \frac{\mathcal{L}_{\text{out}} - \mathcal{L}_{\text{in}}}{\mathcal{L}_{\text{in}}} \tag{5.43}$$

where $\mathcal{L}_{\text{out}}$, $\mathcal{L}_{\text{in}}$ represent the angular momentum per unit mass of the orbiting particle when it leaves and when it enters the scalar field structure, respectively. We show in Fig. 5.3, the angular momentum per unit mass as a function of time. From the picture, we can see that, as expected, the loss of angular momentum is mainly affected by the mass of the orbiting particle.

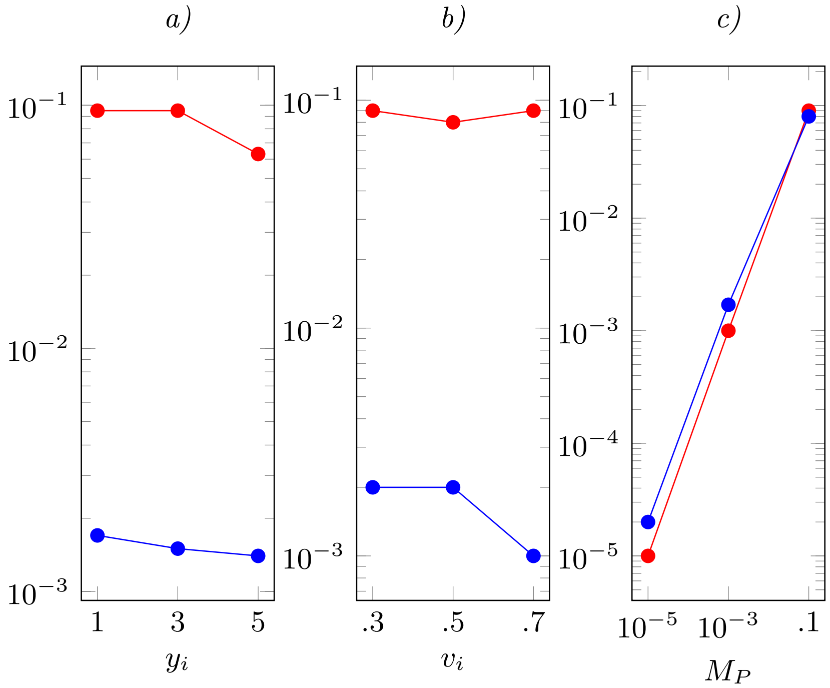

Figure 5.3: Representing $-\Delta\mathcal{L}$ (see Eq. (5.43)) for different sets of simulations. In panel a), MV1, MV2, i.e. mass and velocity are kept constant; red points represent $M_P = 0.1, v_i = 0.7$ and blue points represent $M_P = 0.001, v_i = 0.5$. In panel b) MI1, MI2 i.e. mass and impact parameter are kept constant; red points represent $M_P = 0.1, y_i = 1.0$ and blue points represent $M_P = 0.001, y_i = 1.0$. In panel c) VI1, VI2 i.e. velocity and impact parameter are kept constant; red points represent $v_i = 0.7, y_i = 1.0$ and blue points represent $v_i = 0.5, y_i = 1.0$

Particularly, the following relation can be found

$$\Delta\mathcal{L} = \sigma M_P \tag{5.44}$$

with the proportionality factor, σ, varying slightly with the initial velocity and impact factor being, however, always of order 10^{-1}.

5.3.3 Changes in the density distribution of the field

The appearance of the friction force and the loss of angular momentum are related to the dynamical reaction of the scalar field to the presence of the incoming particle. In this respect, it is verified that the scalar field structure develops non-spherical over-densities that are time dependent. In order to appreciate this behavior, we will isolate the different components of the scalar field density. Using Eqs. (5.30) and (5.31) we can write the quantity $\rho_f = (4\pi)^{-1}\psi\psi^*$ (see Eq. (5.10)) as

$$\rho_f = \frac{1}{4\pi}\left(\rho_A + \rho_{1,-1}Y_{1-1} + \rho_{1,1}Y_{11}\right), \tag{5.45}$$

where

$$\rho_A = \varphi_A\varphi_A^* + \frac{3\sin^2\theta}{8\pi}\left(\varphi_{1,-1}\varphi_{1,-1}^* + \varphi_{1,1}\varphi_{1,1}^*\right), \tag{5.46}$$

$$\rho_{1,-1} = \varphi_{1,-1}\varphi_A^* - \varphi_A\varphi_{1,1}^*, \tag{5.47}$$

$$\rho_{1,1} = \varphi_{1,1}\varphi_A^* - \varphi_A\varphi_{1,-1}^*. \tag{5.48}$$

To simplify the expression for ρ_f, we observe that (see footnote 6)

$$\mathrm{Re}[\rho_{1,-1}] = -\mathrm{Re}[\rho_{1,1}], \quad \mathrm{Im}[\rho_{1,-1}] = \mathrm{Im}[\rho_{1,1}], \tag{5.49}$$

which allows us to write, without loss of generality,

$$\rho_{1,-1}(t,r) = A(t,r) + \mathrm{i}B(t,r)\,,\ \rho_{1,1}(t,r) = -\rho_{1,-1}^*(t,r)\,, \tag{5.50}$$

and with that we can rewrite ρ_f as

$$\rho_f = \frac{1}{4\pi}\left(\rho_A + \sqrt{\frac{3}{2\pi}}\left[A(t,r)\cos\phi + B(t,r)\sin\phi\right]\right), \tag{5.51}$$

where we fixed the value $\theta = \pi/2$ for the orbital plane.

Time dependence of the non-spherical density

The time dependence of the functions $A(t,r)$ and $B(t,r)$ (see Eq. (5.50)) is illustrated in Fig. 5.4. In the figure, we see that the profile of the non-spherical components of the density evolves with time, a behavior that, combined with the angular dependence conveyed by the sinusoidal functions (see Eq. (5.51)), will result in rotating and oscillating non-spherical component of the density of the scalar field. A dramatic example of such behavior can be appreciated in Fig. 5.5 in which it is displayed the value of the density function in the plane $\theta = \pi/2$ for the simulation **L**$Y5V07$. In this particular simulation, the incoming particle is scattered by the scalar field structure and moves past it. However, the short time in which the particle is close to the center of the scalar field structure is enough to give rise to a rotating over-density, as can be seen in the last contour plot presented in the respective figure. This example is simple to represent, however, when the particle stays in a bounded orbit, the non-spherical over-densities have a less organized behavior. In this case, there are two competing effects: on the one hand

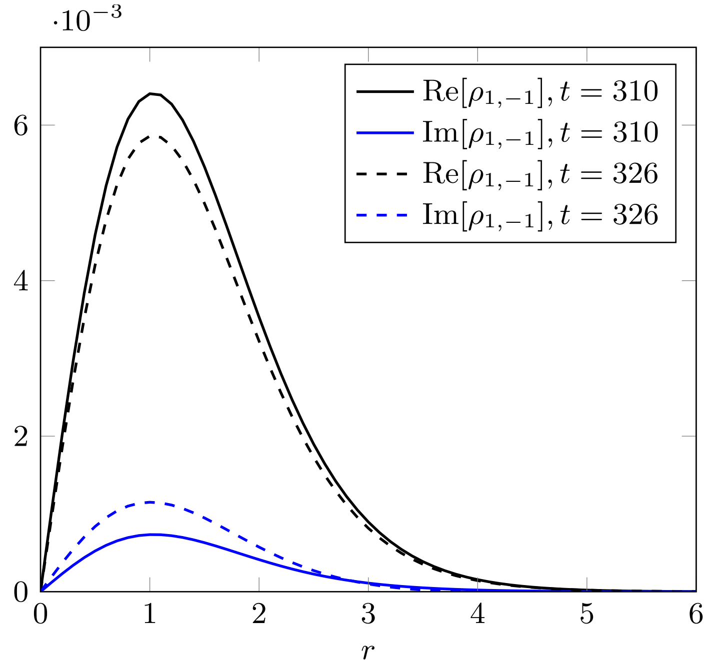

Figure 5.4: Representing the non-spherical components ($A(t,r) = \mathrm{Re}[\rho_{1,-1}]$ and $B(t,r) = \mathrm{Im}[\rho_{1,-1}]$) of the scalar field density obtained from simulation $\mathbf{M}Y5V03$ in two different instants of time. In these two instants of time, we see that as the maximum value of the real component decreases, the imaginary component one increases.

the scalar field structure is dictating the evolution of the non-spherical densities through the SP system and on the other hand the movement of the bounded particle introduces an oscillating "forcing term" on top of that.

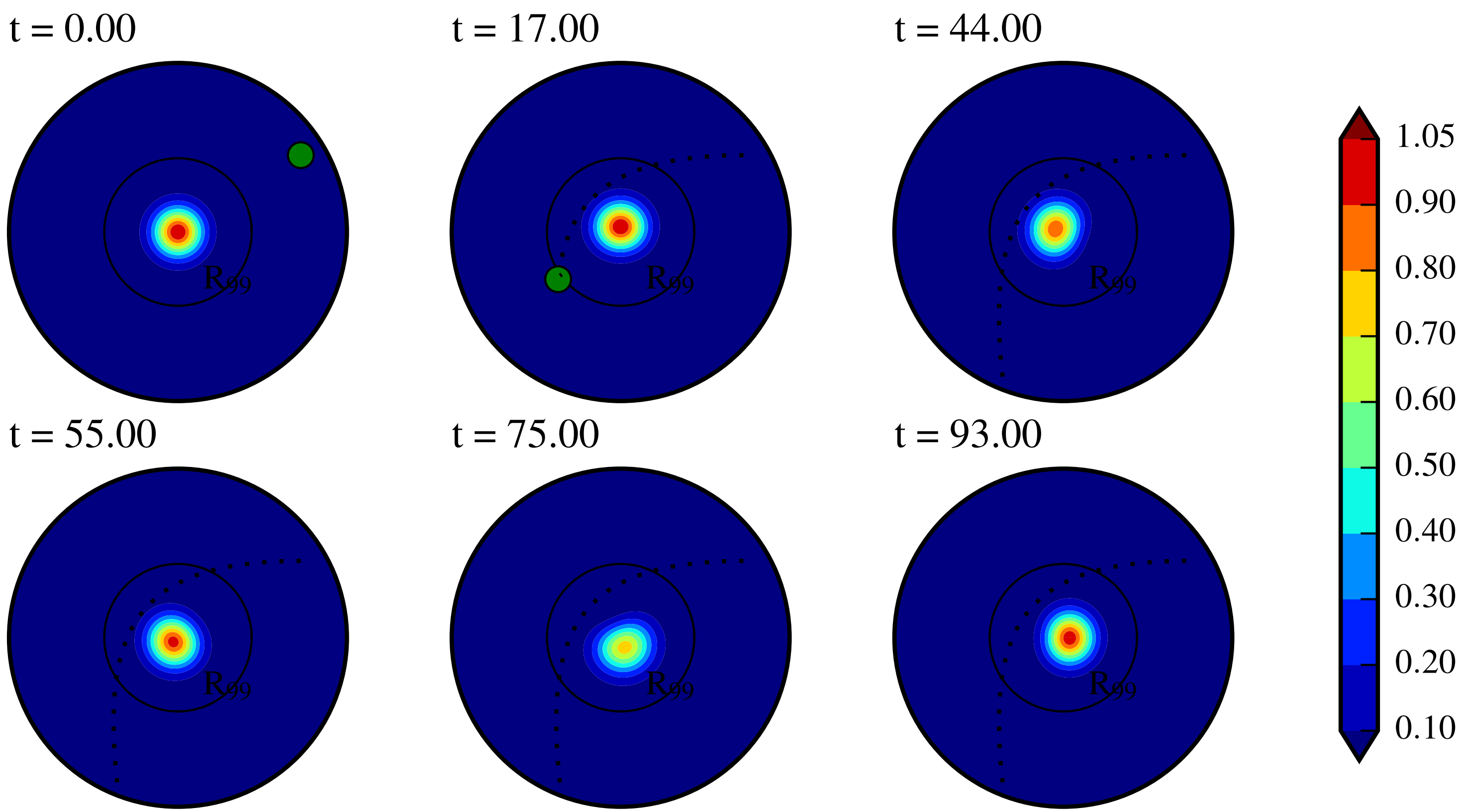

Figure 5.5: We represent the contour plot of the density of the field as in Eq. (5.51) for different instants of time using the simulation $\mathbf{L}Y5V07$. The pointlike particle is shown as a green circle and R_{99} represents the radius of the stable scalar field configuration (see Eq. (5.13)). It is clear that after the passing of the point particle, the scalar field density develops a rotating movement around the origin of coordinates.

In order to illustrate this behavior we will consider the position of the center of mass of the scalar field configuration, which, as shown below, is directly related to the functions A and B (see Eq. (5.50)). The position of the center of mass of the scalar field configuration $\boldsymbol{r}_{CM} = (x_{CM}, y_{CM}, z_{CM})$ is given by

$$\boldsymbol{r}_{CM} = \frac{\int \rho_f(\boldsymbol{r})\boldsymbol{r}\mathrm{d}^3r}{\int \rho_f(\boldsymbol{r})\mathrm{d}^3r}, \tag{5.52}$$

where $\rho_f(\boldsymbol{r})$ is given by Eq. (5.51). Then, the denominator is written as

$$M_f = \int \rho_f(\boldsymbol{r})\mathrm{d}^3r = \frac{1}{4\pi}\left(4\pi \int \varphi_A^*\varphi_A r^2\mathrm{d}r + W_1\left[-\int \varphi_{1,-1}^*\varphi_{1,-1}r^2\mathrm{d}r - \int \varphi_{1,1}^*\varphi_{1,1}r^2\mathrm{d}r\right]\right), \tag{5.53}$$

and since $W_1 = \iint Y_{1-1}Y_{1,1}\sin\theta\mathrm{d}\theta\mathrm{d}\phi = -1$ we obtain that

$$M_f = \int \varphi_A^*\varphi_A r^2\mathrm{d}r + \frac{1}{4\pi}\left(\int \varphi_{1,-1}^*\varphi_{1,-1}r^2\mathrm{d}r + \int \varphi_{1,1}^*\varphi_{1,1}r^2\mathrm{d}r\right). \tag{5.54}$$

In all our simulations the movement is planar, so it suffices to calculate the (x, y) coordinates of the center of mass (the origin of the coordinates is at the center of the initial configuration of the scalar field). We obtain that

$$x_{\mathrm{CM}}M_f = \frac{1}{3}\sqrt{\frac{3}{2\pi}}\int r^3A(t,r)\mathrm{d}r, \tag{5.55}$$

and

$$y_{\mathrm{CM}}M_f = \frac{1}{3}\sqrt{\frac{3}{2\pi}}\int r^3B(t,r)\mathrm{d}r. \tag{5.56}$$

We verify that the center of mass of the scalar configuration oscillates around its initial position – $x_{\mathrm{CM}} = y_{\mathrm{CM}} = 0$ – and the magnitude of the oscillation depends mainly on the mass of the particle. As we can see in Figs. 5.6 and 5.7, bounded orbits will produce less organized oscillations of the coordinates of the center of mass whereas unbounded orbits create a more organized, regular pattern. Moreover, independently of the other parameters, one verifies that $\mathcal{O}(x_{\mathrm{CM}}) \sim 10^{-1}$ for $M_P \sim 10^{-1}$, $\mathcal{O}(x_{\mathrm{CM}}) \sim 10^{-2}$ for $M_P \sim 10^{-3}$ and $\mathcal{O}(x_{\mathrm{CM}}) \sim 10^{-4}$ for $M_P \sim 10^{-5}$; the same relations hold for y_{CM}.

As became clear in the study of the friction force and the loss of angular momentum, the mass of the particle is the most important factor determining the change in its dynamics. Taking that into account, we will focus on the characteristics of the movement of the center of mass of

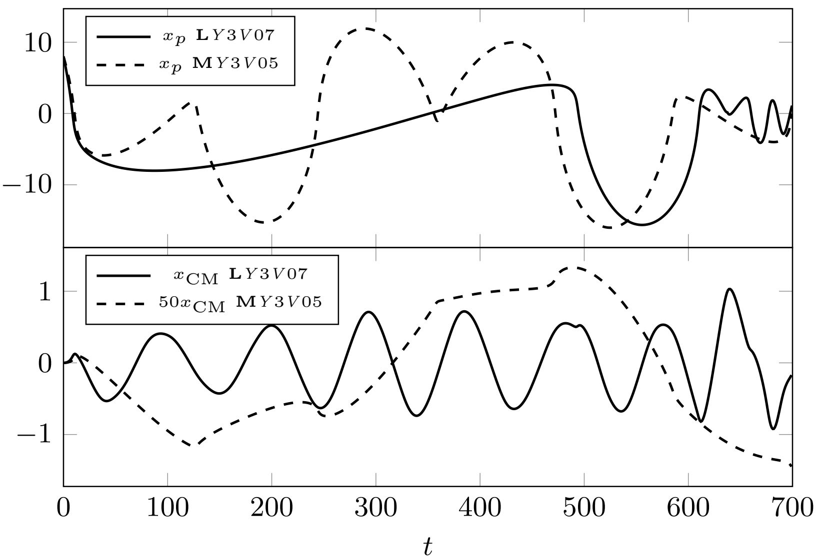

Figure 5.6: Representing the evolution in time of the x-coordinate of the center of mass of the scalar field structure $(x_{\rm CM})$ and of the orbiting particle (x_P) for simulations **L**$Y3V07$ and **M**$Y3V05$. Both simulations represent bounded orbits and they differ only in the mass of the orbiting particle. Notice that the bigger the mass of the particle, the bigger the value of $x_{\rm CM}$ and the more oscillations it presents.

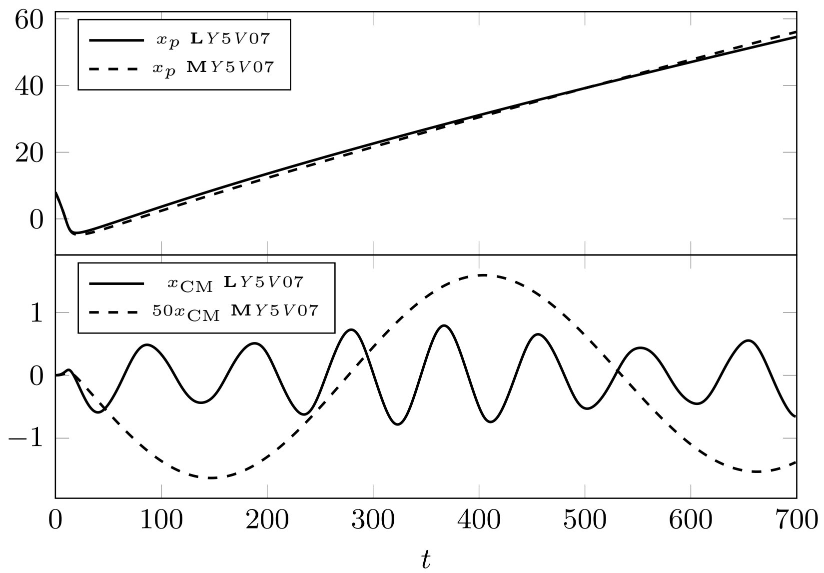

Figure 5.7: Representing the evolution in time of the x-coordinate of the center of mass of the scalar field structure $(x_{\rm CM})$ and of the orbiting particle (x_P) for simulations **L**$Y5V07$ and **M**$Y5V07$. Both simulations represent unbounded orbits and they differ only in the mass of the orbiting particle. Similarly to the bounded orbit case, the bigger the mass of the particle, the bigger the value of $x_{\rm CM}$ and the more it oscillates, but in this case, the particle is unbounded. The center-of-mass of the scalar field structure keeps moving even when the particle goes away.

the scalar field configuration using the simulations **S**$Y5V07$, **M**$Y5V07$ and **L**$Y5V07$. Using this set of simulations is appropriate for two reasons: 1) all the orbits are unbounded, which allows a clearer and simpler analysis of the dynamical aspects of the center of mass; 2) the simulations differ from each other by the value of the mass of the incoming particle, which is exactly the parameter that influences the most all the details of the dynamics of the system. We calculate the radial and angular velocity of the center of mass by using the values of $x_{\rm CM}$ and $y_{\rm CM}$ that we calculate directly from the simulation files (see Eqs. (5.55) and (5.56)). To do it, we use the following expressions

$$r_{\rm CM} = \sqrt{x_{\rm CM}^2 + y_{\rm CM}^2}\,, \tag{5.57}$$

$$\phi_{\rm CM} = \arctan\left(\frac{y_{\rm CM}}{x_{\rm CM}}\right)\,, \tag{5.58}$$

$$\dot{r}_{\rm CM} = \frac{x_{\rm CM}\dot{x}_{\rm CM} + y_{\rm CM}\dot{y}_{\rm CM}}{r_{\rm CM}}\,, \tag{5.59}$$

$$\dot{\phi}_{\rm CM} = \frac{\dot{y}_{\rm CM}x_{\rm CM} - y_{\rm CM}\dot{x}_{\rm CM}}{r_{\rm CM}^2}. \tag{5.60}$$

in which $\dot{x} \equiv dx/dt$. We present the results of these calculations in Fig. 5.8 and from there two things are evident: 1) the behavior of the simulations with the smaller values of the mass of the particle are very similar, except for the frequency of oscillation and the magnitude; 2) the magnitude of the velocity components scales with the mass of the incoming particle, and we verify that

$$\max[\dot{r}_{\rm CM}] = \max[(r\dot{\phi})_{\rm CM}] \propto 0.1 M_P. \tag{5.61}$$

Magnitude of the non-spherical density

In Fig. 5.4 it is plotted the profile of the non-spherical components of the scalar field density, namely $A(t,r)$ and $B(t,r)$ for two different moments in time. The magnitude of these non-spherical components depends on the mass of the neighboring particle: the bigger the mass M_P, the bigger the magnitude of these components, as can be seen in Fig. 5.9. There, we represent the maximum value of the magnitude of functions A and B (see Eq. (5.50)) in the different sets of simulations MV1, MV2, MI1, MI2, VI1 and VI2. We see that, again, of the three initial parameters of the incoming particle, the mass has the strongest influence on the magnitude of the non-spherical components of the scalar field density. In fact, similarly to the

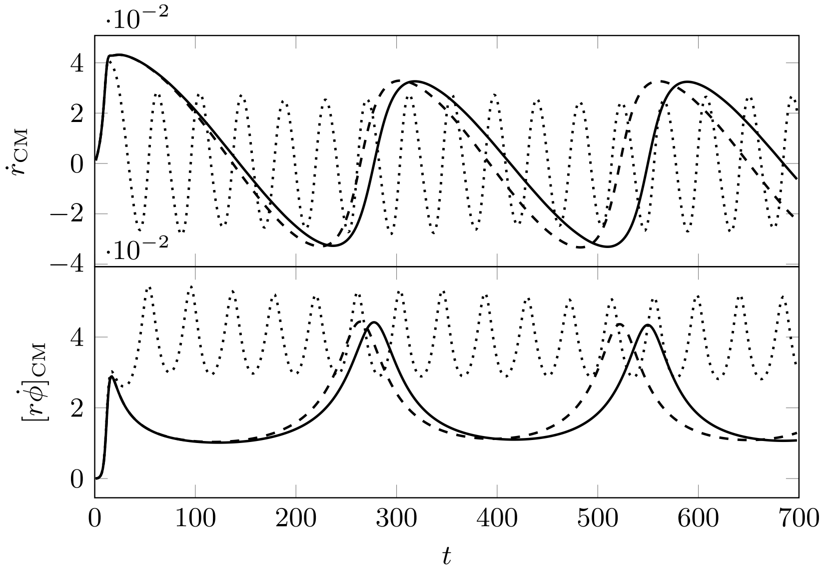

Figure 5.8: Representing the evolution in time of the radial and angular velocities of the center-of-mass of the scalar field structures – Eqs. (5.55) and (5.56) – obtained for the simulations $\mathbf{L}Y5V07$, $\mathbf{M}Y5V07$ and $\mathbf{S}Y5V07$. Dotted lines represent the simulation $\mathbf{L}Y5V07$, dashed lines represent the values of the simulation $\mathbf{M}Y5V07$ multiplied by 10^2 and the filled lines represent the CM velocities of simulation $\mathbf{S}Y5V07$ multiplied by 10^4. Notice the dependence of the magnitude of the CM velocities on the mass of the incoming particle and the similarities of the frequencies and shape of the evolution of simulations $\mathbf{M}Y5V07$ and $\mathbf{S}Y5V07$.

case of the friction force, one can write

$$\max{[A]} \sim \beta_A M_P, \quad \max{[B]} \sim \beta_B M_P, \tag{5.62}$$

i.e., the maximum magnitude of both A and B is directly proportional to the mass of the incoming particle, with the proportionality factors $\beta_{A,B}$ presenting values between 3 and 5 without any correlation with the initial velocity and impact parameter of the particle.

5.4 Discussion

We studied what happens to a stable, low-energy scalar field configuration when a particle-like body passes in its neighborhood. The apparent strong connection between the mass of the incoming particle and the effects it leaves on the scalar field structure, may become a good lead in investigations about the history of the latter. In the scenarios in which DM is described by such scalar field structures, the detection of rotating clumps of DM in galaxies may be explained by a primordial encounter between the DM aggregate and a passing massive particle-like body. Moreover, the results about the gravitational friction force felt by the orbiting particle

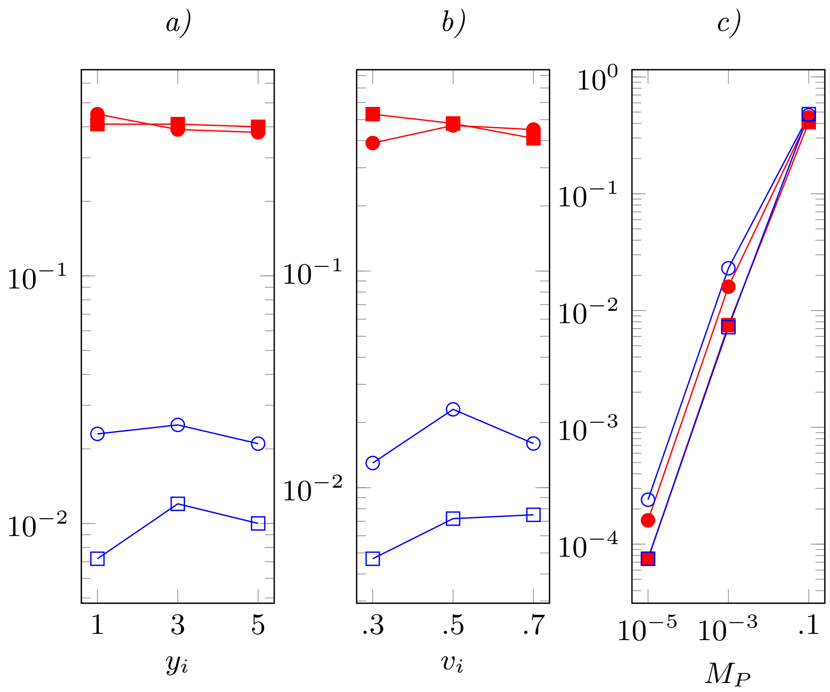

Figure 5.9: Representing the maximum value in time and space of $\mathrm{Re}[\rho_{1,-1}]$ (by $\bullet$ or $\circ$) and $\mathrm{Im}[\rho_{1,-1}]$ (by $\blacksquare$ or $\square$) for different sets of simulations. In panel a) MV1,MV2, i.e. mass and velocity are kept constant; red, filled points represent $M_P = 0.1, v_i = 0.7$ and blue, hollow points represent $M_P = 0.001, v_i = 0.5$. In panel b) MI1, MI2 i.e. mass and impact parameter are kept constant; red, filled points represent $M_P = 0.1, y_i = 1.0$ and blue, hollow points represent $M_P = 0.001, y_i = 1.0$. In panel c) VI1, VI2 i.e. velocity and impact parameter are kept constant; red, filled points represent $v_i = 0.7, y_i = 1.0$ and blue, hollow points represent $v_i = 0.5, y_i = 1.0$.

provide a good description of the backreaction effects of a scalar field structure. Although one needs sufficiently massive bodies to obtain a dominant effect of this force, improvements in the data-gathering techniques and ever more precise instrumentation may allow for the detection of deviations on the trajectories of astrophysical bodies due to this force.

Chapter 6

Conclusion

The investigations that address the existence of astrophysically-relevant scalar-field structures are developed by anticipation. Following a path illuminated by reasonable considerations (both theoretical and observational), they anticipate the signatures the existence of those structures may leave. As anything that is done by anticipation, several things can be said and done that fit the available information or intuition about the problem under consideration. In the worst case scenario, the exercise of anticipation can lead to a miriad of possibilities that are, all of them, unattainable; in the best case scenario, the outcome of this project may lead at least to one instance in which a good prediction is produced. Being the latter the situation we're hoping to obtain, we devoted this thesis to explore and calculate effects that the existence of scalar-field structures may leave on the measurable chacteristics of celestial bodies. Here are the additions we made to a vast (and growing) body of work:

- the development of a scalar cloud in the SMBH-part of a generic EMRI gives rise to orbital resonances which can influence the inspiraling of the lighter-part of the binary (Ref. [125]);

- the development of a scalar cloud in the SMBH in the center of the Milky Way gives rise to peculiar variations of the orbital elements of the S2 star, one the stars that populates that central region of the galaxy (Ref. [142]);

- low-energy boson stars can develop long-lived rotating clumps after a scattering event with a point-like body; moreover, the point-like body, as it traverses the boson star, is acted upon by a gravitational friction force that scales as the square of its mass (Ref. [152]).

The great interest in the development of instruments that can provide more data about the Universe can only serve as a source of optimism with respect to the search for its hidden components. The recent succession of outstanding detections – gravitational wave detection by the LIGO collaboration, the measurement of the gravitational redshift by GRAVITY, the first picture of a shadow of a BH by the Event Horizon Telescope – makes us feel as if we are on the verge of uncovering something fundamental. It is with this spirit of expectation and enthusiasm that we look forward for a moment in which conclusive observational data can put our astrophysical scenarios to the test.

Appendix A

Newtonian utilities

In this appendix we start by analysing the case in which the spacetime metric is a small deviation of the Minkowski metric and how to quantify that deviation. Then we write the dominant components of the energy-momentum tensor of a scalar field in a weak-field regime and we relate them to the underlying spacetime metric. Still in the weak-field regime, we note that the Klein-Gordon equation can be effectively described by the Schroedinger equation and we analyse the description of a point-particle as a source of the Poisson's equation. We finish this appendix with a discussion on the harmonic decomposition technique and a note on Lagrangian points.

A.1 Linearized gravity

We'll follow an analysis presented in many books (e.g. [159, 160]). Here, we'll discuss an approximation of General Relativity which is valid when gravity is everywhere weak, i.e., when spacetime is approximately flat:

$$g_{\alpha\beta} = \eta_{\alpha\beta} + h_{\alpha\beta}, \tag{A.1}$$

where $\eta_{\alpha\beta}$ is the Minkowski metric, which will be the background, and $h_{\alpha\beta}$ is a perturbation tensor that is small compared to the background, i.e., $|h_{\alpha\beta}| \ll 1$. In what follows we only retain the terms of the equations that are first order in the perturbation of the metric. Imposing this decomposition of the metric tensor implies that part of the coordinate freedom of General Relativity is lost, because not all the coordinate transformations preserve the decomposition of Eq. (A.1). The subset of coordinate transformations that satisfy this condition are some Lorentz transformations and transformations of the form

$$x^{\alpha} \to x'^{\alpha} = x^{\alpha} + \chi^{\alpha}(x^{\beta}), \tag{A.2}$$

for vectors χ^{α} of the same order of the perturbation $h_{\alpha\beta}$. Under this transformation of coordinates, the metric perturbation transforms in such a way that resembles a gauge transformation (see chapter 17 of [160]); we'll skip those details.

A consequence of keeping only the terms up to first order in the metric perturbation is that the indices of quantitites of such order are lowered and raised using the background metric, i.e.

$$h^{\alpha\beta} = \eta^{\alpha\mu}\eta^{\beta\nu}h_{\mu\nu}, \quad h = \eta^{\alpha\beta}h_{\alpha\beta}. \tag{A.3}$$

Moreover, considering the relation $g^{\alpha\nu}g_{\nu\beta} = \delta^{\alpha}_{\beta}$, the inverse total metric, up to terms of first order in the perturbation metric, is given by

$$g^{\alpha\beta} = \eta^{\alpha\beta} - h^{\alpha\beta}. \tag{A.4}$$

The Christoffel symbols are, up to first order in the perturbation of the metric, given by

$$\Gamma^{\alpha}_{\beta\gamma} = \frac{1}{2}\left(\partial_{\beta}h^{\alpha}_{\ \gamma} + \partial_{\gamma}h^{\alpha}_{\ \beta} - \partial^{\alpha}h_{\beta\gamma}\right), \tag{A.5}$$

and the Riemann tensor reads[1]

$$R_{\alpha\beta\mu\nu} = \frac{1}{2}\left(\partial_{\beta\mu}h_{\alpha\nu} - \partial_{\beta\nu}h_{\alpha\mu} - \partial_{\alpha\mu}h_{\beta\nu} + \partial_{\alpha\nu}h_{\beta\mu}\right), \tag{A.6}$$

where $\partial_{\alpha\beta} = \partial_{\alpha}\partial_{\beta}$. The Ricci tensor and scalar are

$$R_{\alpha\beta} = -\frac{1}{2}\left(\Box h_{\alpha\beta} + \partial_{\alpha\beta}h - \partial_{\alpha\mu}h^{\mu}_{\ \beta} - \partial_{\beta\mu}h^{\mu}_{\ \alpha}\right), \tag{A.7}$$

$$R = -\Box h + \partial_{\mu\nu}h^{\mu\nu}, \tag{A.8}$$

where $\Box = \eta^{\alpha\beta}\partial_{\alpha\beta}$. One can now write the Einstein tensor

$$G_{\alpha\beta} = -\frac{1}{2}\left(\Box h_{\alpha\beta} + \partial_{\alpha\beta}h - \partial_{\alpha\mu}h^{\mu}_{\ \beta} - \partial_{\beta\mu}h^{\mu}_{\ \alpha}\right) + \frac{1}{2}\eta_{\alpha\beta}\left(\Box h - \partial_{\mu\nu}h^{\mu\nu}\right). \tag{A.9}$$

[1]The linearized Riemann tensor is gauge-invariant (see Eq. (A.2).

Before analysing Einstein's equations we will first decompose both the perturbation tensor $h_{\alpha\beta}$ and the enery-momentum tensor $T_{\alpha\beta}$ in their explicit scalar, vector and tensor components[2]. This decomposition can be written as

$$h_{00} = 2U/c^2, \tag{A.10}$$

$$h_{0j} = -4U_j/c^3 - \partial_j A/c, \tag{A.11}$$

$$h_{ij} = 2\delta_{jk}V/c^2 + \left(\partial_{jk} - \frac{1}{3}\delta_{jk}\nabla^2\right)B + \left(\partial_j B_k + \partial_k B_j\right)/c^2 + h_{jk}^{\mathrm{TT}}, \tag{A.12}$$

with the elements of the decomposion satisfying the following conditions:

$$\partial_j U^j = 0, \quad \partial_j B^j = 0, \quad \partial_k h_{\mathrm{TT}}^{jk} = 0 = \delta_{jk} h_{\mathrm{TT}}^{jk}. \tag{A.13}$$

With this decomposition, the original ten degrees of freedom of the metric perturbation tensor $h_{\alpha\beta}$ are made explicit:

- one component in the potential U;
- two components in the vector potential U_j
- one component in the scalar A;
- one component in the scalar B;
- two components in the vector B_j;
- two components in the transverse, traceless tensor h_{ij}^{TT}

The factors in the decomposition were added following Ref. [159] for later convenience.

It was first observed by Bardeen [163] that it is possible to combine the different components of the metric into gauge-invariant variables (see Eq. (A.2)) – the so-called Bardeen variables –

[2] A symmetric 4×4 spacetime tensor $A_{\mu\nu}$ in a constant curvature background manifold can be decomposed into scalar, vector and tensor independent parts. This is the statement of the scalar-vector-tensor decomposition. This decomposition is related to the way each component transforms under the group of rotations of the background. Given that A_{00} has no spatial indices, it is a scalar; $A_{0i} = A_{i0}$ has one spatial index, so it is a vector; finally, $A_{ij} = A_{ji}$ is a spatial tensor. The decomposition is not complete since it is possible to decompose both the vector A_{0i} and the tensor A_{ij} in scalar, vector and tensor components. This second part of the decomposition is made by observing that the symmetry of the spatial part of the background manifold allows the expansion of vectors and symmetric tensors in terms of solutions of the Helmholtz equation (see, for instance, [161–165]). This is achieved by projecting each object in the basis elements of the space of solutions of the Helmholtz equation [165, 166]. Consequently, an arbitrary vector is broken into a scalar and a transverse vector (a rendition of the original Helmholtz theorem); an arbitrary symmetric tensor is decomposed into two scalars, one transverse vector and a transverse traceless tensor [164, 166].

given by

$$\tilde{\Phi} = U + \partial_t A + \frac{1}{2}\partial_{tt} B \tag{A.14}$$

$$\tilde{\Phi}_j = U_j + \frac{1}{4}\partial_t B_j \tag{A.15}$$

$$\tilde{\Psi} = V - \frac{c^2}{6}\nabla^2 B \tag{A.16}$$

where $\tilde{\Phi}$ and $\tilde{\Psi}$ account for two degrees of freedom, $\tilde{\Phi}_j$, which is subjected to the condition $\partial_i \tilde{\Phi}^i = 0$, carries two degrees of freedom. Besides these three variables, the transverse-traceless component h_{ij}^{TT} is also gauge-invariant, and describes two degrees of freedom. This means that of the ten original degrees of freedom of the perturbation tensor, only six are gauge-invariant, i.e., the gravitational perturbation only has six physical degrees of freedom; the other four are *coordinate artifacts*.

Having identified the meaningful quantities, one can now fix a convenient gauge in order to perform actual calculations. We'll focus on the Coulomb gauge which fixes

$$A = B = B_j = 0 \tag{A.17}$$

so that the perturbation tensor components read

$$h_{00} = 2U/c^2, \quad h_{0j} = -4U_j/c^3, \quad h_{jk} = 2\delta_{jk} V/c^2 + h_{jk}^{\mathrm{TT}} \tag{A.18}$$

along with the condition $\partial_j U^j = 0$. In this gauge, the corresponding Bardeen coordinates are more clearly related to the potentials obtained in the decomposition of the metric tensor, i.e.,

$$\tilde{\Phi} = U, \quad \tilde{\Phi}_j = U_j, \quad \tilde{\Psi} = V. \tag{A.19}$$

Introducing the metric of Eq. (A.18) in the linearized Riemann tensor[3] one obtains the components of the Einstein's tensor (pay attention to the use of the index t, it is related to the index 0

[3]The Riemann tensor is gauge-invariant.

as $x^0 = ct$)

$$G_{00} = -\frac{2}{c^2}\nabla^2 V, \tag{A.20}$$

$$G_{0j} = -\frac{2}{c^3}\partial_{tj}V + \frac{2}{c^3}\nabla^2 U_j, \tag{A.21}$$

$$G_{jk} = -\frac{2}{3c^2}\delta_{jk}\nabla^2(U-V) - \frac{2}{c^4}\delta_{jk}\partial_{tt}V + \frac{1}{c^2}\left(\partial_{jk} - \frac{1}{3}\delta_{jk}\nabla^2\right)(U-V),$$
$$+\frac{2}{c^4}\left(\partial_{tk}U_k + \partial_{tk}U_j\right) - \frac{1}{2}\Box h^{\mathrm{TT}}_{jk}, \tag{A.22}$$

where $\Box = \eta^{\alpha\beta}\partial_{\alpha\beta}$; in this form, the Einstein tensor is decomposed in its various decoupled pieces. Before turning to the Einstein's equations one has to decompose the energy-momentum tensor in the same way:

$$T^{00} = c^2\rho, \tag{A.23}$$

$$T^{0j} = c(s^j + \partial^j s), \tag{A.24}$$

$$T^{jk} = \tau\delta^{jk} + \left(\partial^{jk} - \frac{1}{3}\delta^{jk}\nabla^2\right)\sigma + \partial^j\sigma^k + \partial^k\sigma^j + \sigma^{jk}, \tag{A.25}$$

where, by virtue of the decomposion, the following conditions are verified

$$\partial_j s^j = 0, \quad \partial_j\sigma^j = 0, \quad \partial_k\sigma^{jk} = 0 = \delta_{jk}\sigma^{jk}. \tag{A.26}$$

Similarly to the case of the metric tensor, out of the ten degrees of freedom of the energy-momentum tensor, the physical information is contained only in six of them. They can be identified by using the linearized energy-momentum conservation condition $\partial_\beta T^{\alpha\beta} = 0$ to the energy-momentum tensor in the decomposed form, giving

$$\nabla^2 s = -\partial_t\rho, \quad \nabla^2\sigma^j = -\partial_t s^j, \quad \nabla^2\sigma = -\frac{3}{2}(\partial_t s + \tau), \tag{A.27}$$

which mean that only ρ, s^j, τ and σ_{jk} are independent (making six degrees of freedom) and the other components depend on these. Now, using Eqs. (A.20), (A.21) and (A.22) and Eqs. (A.23), (A.24) and (A.25) in the Einstein's equations, one obtains the following equations:

$$\nabla^2 V = -4\pi G\rho, \tag{A.28}$$

$$\nabla^2 (U - V) = -\frac{12\pi G}{c^2}(\partial_t s + \tau), \tag{A.29}$$

$$\nabla^2 U_j = -4\pi G s_j, \tag{A.30}$$

$$\Box h^{\rm TT}_{jk} = -\frac{16\pi G}{c^4}\sigma_{jk}. \tag{A.31}$$

A.2 Energy-momentum tensor of a scalar field in the weak-field regime

Here we will look at the two scalar field cases, the real and the complex one. The simplest is the complex scalar field because its enery-momentum tensor doesn't depend on time. As a consequence, the only component of order c^{-2} will appear in T_{00}. This is not the case for the real scalar field, in which besides this component, the diagonal components T_{ij} will also be of order c^{-2}.

Independently of the nature of the field – real or complex – its energy momentum tensor can be organized as follows

$$T_{00} = \frac{m_s^2 c^2}{2\hbar^2}\left|\Phi\right|^2 + \frac{1}{2c^2}\left(\partial_t \Phi\right)\left(\partial_t \Phi^*\right) + \mathcal{O}(1), \tag{A.32}$$

$$T_{0j} \sim \mathcal{O}(c^{-1}), \tag{A.33}$$

$$T_{jk} = \delta_{jk}\left(-\frac{m_s^2 c^2}{2\hbar^2}\left|\Phi\right|^2 + \frac{1}{2c^2}\left(\partial_t \Phi\right)\left(\partial_t \Phi^*\right)\right) + \mathcal{O}(1), \tag{A.34}$$

where δ_{jk} is the Kronecker delta.

This low-energy analysis is appropriate for any scalar-field configuration in a almost-flat spacetime, so we won't distinguish between the BHs quasi-bound state case

$$\Phi = A_0 g(r)\sin\theta \mathrm{e}^{-\mathrm{i}(\omega t - \phi)}, \quad \text{complex case} \tag{A.35}$$

$$\Phi = A_0 g(r)\sin\theta\cos(\omega t - \phi), \quad \text{real case} \tag{A.36}$$

where

$$g(r) = \left[\frac{2\alpha^2 r}{\ell + n + 1}\right]\exp\left(-\frac{\alpha^2 r}{\ell + n + 1}\right), \tag{A.37}$$

(see Eqs. (2.23) and (2.24)) and the self-gravitation bound state case[4]

$$\Phi = \phi(r)\mathrm{e}^{-\mathrm{i}\omega t}, \quad \text{complex case – boson star} \tag{A.38}$$

$$\Phi = \phi_1(r)\cos(\omega t) \quad \text{real case – oscillaton.} \tag{A.39}$$

In fact, there's something that is shared between all the cases under analysis, which is the fact that their fundamental frequency, in this low-energy regime, is given by (notice we're introducing the fundamental constants here)

$$\omega \sim \frac{m_s c^2}{\hbar}. \tag{A.40}$$

The only difference will appear in the treatment between the real and the complex case. In the complex case, we obtain that the energy-momentum tensor is given by

$$T^C_{00} = \frac{m_s^2 c^2}{\hbar^2}\left(A_0 g(r)\sin\theta\right)^2 + \mathcal{O}(1), \tag{A.41}$$

$$T^C_{0j} \sim \mathcal{O}(c^{-1}), \tag{A.42}$$

$$T^C_{jk} = \mathcal{O}(1), \tag{A.43}$$

whereas in the real case we obtain

$$T^R_{00} = \frac{m_s^2 c^2}{2\hbar^2}\left(A_0 g(r)\sin\theta\right)^2 + \mathcal{O}(1), \tag{A.44}$$

$$T^R_{0j} \sim \mathcal{O}(c^{-1}), \tag{A.45}$$

$$T^R_{jk} = -\frac{m_s^2 c^2}{2\hbar^2}\left(A_0 g(r)\sin\theta\right)^2 \cos\left(2(\omega t - \phi)\right) + \mathcal{O}(1). \tag{A.46}$$

Comparing these explicit calculations with the expansions in Eqs. (A.23), (A.24) and (A.25) and matching, order by order, with the elements of Eqs. (A.20), (A.21) and (A.22), one concludes

[4]Notice that we are assuming that the oscillaton is described only with one element of the cosine expansion – this is the correct assumption given that in this regime the first component is the absolute dominant (this approach is considered in other works, for instance in Ref. [51]).

that Eqs. (A.28) to (A.31), reduce to, in the Coulomb gauge,

$$\nabla^2 V = -4\pi G \frac{m_s^2}{\hbar^2} \left[A_0 g(r) \sin\theta\right]^2, \tag{A.47}$$

$$\nabla^2 U = \nabla^2 V, \tag{A.48}$$

$$\nabla^2 U_j = 0, \tag{A.49}$$

$$\Box h_{jk}^{\mathrm{TT}} = 0. \tag{A.50}$$

for the complex case and

$$\nabla^2 V = -4\pi G \frac{m_s^2}{2\hbar^2} \left[A_0 g(r) \sin\theta\right]^2, \tag{A.51}$$

$$\nabla^2 (U - V) = -\frac{12\pi G}{c^2} \left(-\frac{m_s^2 c^2}{2\hbar^2} \left[A_0 g(r) \sin\theta\right]^2 \cos\left(2(\omega t - \phi)\right) \right), \tag{A.52}$$

$$\nabla^2 U_j = 0, \tag{A.53}$$

$$\Box h_{jk}^{\mathrm{TT}} = 0, \tag{A.54}$$

for the real case, from were we can conclude that

$$\nabla^2 U = -4\pi G \frac{m_s^2}{2\hbar^2} \left[A_0 g(r) \sin\theta\right]^2 \Big(1 - 3\cos\left(2(\omega t - \phi)\right) \Big). \tag{A.55}$$

Identifying the Newtonian potential

In the Coulomb gauge of the weak-field regime, the only relevant components of the metric due to the presence of scalar field configuration are the potentials U and V:

$$ds^2 = [-1 + 2U/c^2](cdt)^2 + [\delta_{jk}(1 + 2V/c^2)]dx^j dx^k. \tag{A.56}$$

Plugging this metric in the geodesic equation and collecting only the terms up to order c^{-2}, we obtain

$$\frac{d^2 t}{d\tau^2} = 0 + \mathcal{O}(c^{-2}), \tag{A.57}$$

$$\frac{d^2 x^i}{d\tau^2} - \left(\frac{dt}{d\tau}\right)^2 \frac{dU}{dx^i} = 0 + \mathcal{O}(c^{-2}), \tag{A.58}$$

$$\tag{A.59}$$

particularly, we know that

$$\dot{t} = \frac{dt}{d\tau} = \sqrt{\frac{1}{1 - \frac{v^2}{c^2} - \frac{2U}{c^2} - \frac{2Vv^2}{c^4}}} \sim 1 + \mathcal{O}(c^{-2}), \tag{A.60}$$

because we assume that the particle is non-relativistic. From here, the geodesic equation for the coordinate time is satisfied - $\ddot{t} = 0 + \mathcal{O}(c^{-2})$ and the geodesic equation for the space coordinates reduce to

$$\ddot{\boldsymbol{x}} = \nabla U + \mathcal{O}(c^{-2}). \tag{A.61}$$

We conclude that the perturbation potential U of the g_{tt} component of the metric corresponds to the Newtonian potential.

A.3 Klein-Gordon equation

Using the post-Newtonian metric $ds^2 = [-1 + 2U/c^2](cdt)^2 + [\delta_{jk}(1 + 2U/c^2)]dx^j dx^k$ and the scalar field in the weak-field regime (see Eq. (2.86))

$$\Psi(t, \boldsymbol{x}) = \exp\left(-\mathrm{i}\frac{m_s c^2}{\hbar} t\right) \psi(t, \boldsymbol{x}), \tag{A.62}$$

where we explicitly wrote the fundamental constants, in the Klein-Gordon equation

$$\frac{1}{\sqrt{-g}} \partial_\nu \left(\sqrt{-g} g^{\mu\nu} \partial_\mu \Psi\right) - \frac{m_S^2 c^2}{\hbar^2} \Psi = 0, \tag{A.63}$$

we can write

$$\mathrm{i}\partial_t \psi + \frac{\hbar}{2m_S} \nabla^2 \psi + \frac{m_S}{\hbar} U \psi + \mathcal{O}(c^{-2}) = 0. \tag{A.64}$$

From here, we see that the dynamics described by the Klein-Gordon equation is dominated by the Schrodinger equation in the weak-field regime.

A.4 Derivation of the equations for the influence of the orbiting particle in the low-energy regime

To account for the influence of a point-like particle, we'll follow section 6 of Ref. [153] to write its energy-momentum tensor (reintroducing the fundamental constants)

$$T^{\mu\nu} = \frac{1}{\sqrt{-g}} m_p c \int \frac{dx_p^\mu}{d\tau}\frac{dx_p^\nu}{d\tau}\delta^{(4)}(x - x_p(\tau))d\tau, \tag{A.65}$$

where m_p and x_p^μ are the mass and the coordinates of the point-particle, τ is the proper-time and g is the determinant of the metric. Writing explicitly the time-coordinate part of the Dirac delta,

$$T^{\mu\nu} = \frac{1}{\sqrt{-g}} m_p c \int \frac{dx_p^\mu}{d(ct)}\frac{dx_p^\nu}{d(ct)}\left(\frac{d(ct)}{d\tau}\right)^2 \delta((ct)-(ct_p))\delta^{(3)}(x-x_p(t(\tau)))\frac{d\tau}{d(ct)}d(ct), \tag{A.66}$$

we integrate in ct (which is the space-time coordinate x^0) and we obtain

$$T^{\mu\nu} = \frac{1}{\sqrt{-g}} m_p \frac{dx_p^\mu}{dt}\frac{dx_p^\nu}{dt}\left(\frac{dt}{d\tau}\right)\delta^{(3)}(x - x_p(t(\tau))), \tag{A.67}$$

which agrees with the expression given in Ref. [164] for the case of flat metric.

Considering that the mass of the point-particle, as well as its velocity, are within a Newtonian regime, we can use the weak-field metric $ds^2 = [-1 + 2U/c^2](cdt)^2 + [\delta_{jk}(1 + 2V/c^2)]dx^j dx^k$ to obtain the value for $dt/d\tau$ by observing that the proper time τ of a timelike particle is defined as

$$c^2 d\tau^2 = -ds^2 = -g_{\mu\nu}dx^\mu dx^\nu = -[-1 + 2U/c^2](cdt)^2 - [\delta_{jk}(1 + 2V/c^2)]dx^j dx^k, \tag{A.68}$$

and so

$$\left(\frac{d\tau}{dt}\right)^2 = 1 - \frac{v^2}{c^2} - \frac{2U}{c^2} - \frac{2Vv^2}{c^4}, \tag{A.69}$$

where v is the modulus of the velocity of the particle. Expanding in powers of the velocity of light, we obtain

$$\left(\frac{dt}{d\tau}\right)^2 = \frac{1}{1 - \frac{v^2}{c^2} - \frac{2U}{c^2} - \frac{2Vv^2}{c^4}} \approx 1 + \frac{v^2 + 2U}{c^2} + \mathcal{O}(c^{-4}). \tag{A.70}$$

Using the same metric, we can also write

$$\frac{1}{\sqrt{-g}} = \frac{1}{\sqrt{1 - \frac{16UV^3}{c^8} - \frac{24UV^2}{c^6} + \frac{8V^3}{c^6} - \frac{12UV}{c^4} + \frac{12V^2}{c^4} - \frac{2U}{c^2} + \frac{6V}{c^2}}} \approx 1 + \frac{U - 3V}{c^2} + \mathcal{O}(c^{-4}). \tag{A.71}$$

Finally, the energy-momentum tensor of the particle in a weak-field limit is given by

$$T^{\mu\nu} = m_p \frac{dx_p^\mu}{dt}\frac{dx_p^\nu}{dt}\delta^{(3)}(x - x_p(t(\tau))). \tag{A.72}$$

The components of this energy-momentum tensor can be written as

$$\frac{8\pi G}{c^4}T_{00} = 8\pi G\left(\frac{m_p}{c^2} + \mathcal{O}(c^{-4})\right)\delta^{(3)}(x - x_P)\,, \tag{A.73}$$

$$\frac{8\pi G}{c^4}T_{0j} = 8\pi G\left(-\frac{m_p}{c^3}v_j + \mathcal{O}(c^{-5})\right)\delta^{(3)}(x - x_P)\,, \tag{A.74}$$

$$\frac{8\pi G}{c^4}T_{jk} = 8\pi G\left(\frac{m_p}{c^4}v_j v_k + \mathcal{O}(c^{-6})\right)\delta^{(3)}(x - x_P)\,. \tag{A.75}$$

where we introduced the factor $(8\pi G)/(c^4)$ because it'll be used in the Einstein's equations. Considering that the velocity of the particle is much smaller than the velocity of light, its energy momentum tensor reduces to

$$\begin{aligned} \frac{8\pi G}{c^4}T_{00} &= 8\pi G\left(\frac{m_p}{c^2} + \mathcal{O}(c^{-4})\right)\delta^{(3)}(x - x_P)\,, \\ \frac{8\pi G}{c^4}T_{0j} &= \mathcal{O}(c^{-3})\,, \\ \frac{8\pi G}{c^4}T_{jk} &= \mathcal{O}(c^{-4})\,, \end{aligned} \tag{A.76}$$

which is a reflection of the fact that the behavior of the particle is dominated by its rest mass.

The Einstein tensor, with the metric $ds^2 = [-1 + 2U/c^2](cdt)^2 + [\delta_{jk}(1 + 2V/c^2)]dx^j dx^k$, is given by

$$G_{00} = -\frac{2}{c^2}\nabla^2 V + \mathcal{O}(c^{-4})\,, \tag{A.77}$$

$$G_{0j} = \mathcal{O}(c^{-3})\,, \tag{A.78}$$

$$G_{jk} = -\frac{2}{3c^2}\delta_{jk}\nabla^2(U - V) + \frac{1}{c^2}\left(\partial_{jk} - \frac{1}{3}\delta_{jk}\nabla^2\right)(U - V) + \mathcal{O}(c^{-4}).$$

Using the energy-momentum of the point particle as a source of the Einstein's equations,

$$G_{\alpha\beta} = \frac{8\pi G}{c^4} T_{\alpha\beta}\,, \tag{A.79}$$

and collecting the dominant terms, one obtains

$$\nabla^2 U = \nabla^2 V = -4\pi G \left(m_p \delta^{(3)}(x - x_P) \right). \tag{A.80}$$

A.5 Harmonic decomposition

To solve Poisson's equation

$$\nabla^2 U_{\rm N} = -4\pi\rho, \tag{A.81}$$

we employ the spherical harmonic decomposition technique [159]. With this technique, the solution to the Poisson's equation is given by

$$U_{\rm N} = \sum_{\ell m} \frac{4\pi}{2\ell+1} \left[q_{\ell m}(r) \frac{Y_{\ell m}(\theta,\phi)}{r^{\ell+1}} + p_{\ell m}(r) Y_{\ell m}(\theta,\phi) \right], \tag{A.82}$$

where $Y_{\ell m}$ are spherical harmonics and

$$q_{\ell m}(r) = \int_0^r s^\ell \tilde{\rho}_{\ell m}(t,s) s^2 {\rm d}s, \tag{A.83}$$

$$p_{\ell m}(r) = \int_r^\infty \frac{\tilde{\rho}_{\ell m}(t,s)}{s^{\ell+1}} s^2 {\rm d}s, \tag{A.84}$$

$$\tilde{\rho}_{\ell m} = \int \rho Y^*_{\ell m} \sin\theta {\rm d}\theta {\rm d}\phi. \tag{A.85}$$

A.6 Lagrangian points

A general potential $U = U(r,\phi)$ produces a motion governed by equations on a plane (r,ϕ) rotating with angular velocity Ω_p given by

$$\ddot{r} - r(\dot{\phi} + \Omega_p)^2 + \frac{\partial U}{\partial r} = 0 \tag{A.86}$$

$$\frac{d}{dt}(r^2(\dot{\phi} + \Omega_p)) + \frac{\partial U}{\partial \phi} = 0 \tag{A.87}$$

The Lagrangian points are the points where the forces acting on the orbiting particle cancel exactly. To uncover those locations, one forces the equations of motion to describe a particle at rest in this frame, i.e. $\dot{r} = \ddot{r} = \ddot{\phi} = \dot{\phi} = 0$, which amounts to

$$\frac{\partial U}{\partial r} = r\Omega_p^2, \tag{A.88}$$

$$\frac{\partial U}{\partial \phi} = 0. \tag{A.89}$$

Applying this reasoning to the total potential in Eq. (3.12), $U = V_0 + V_1$, one can see from Eq. (A.89) that the Lagrangian points are located at $\phi = 0, \pi/2, \pi, 3\pi/2, ...$ since

$$\frac{\partial U}{\partial \phi} = 0 \Leftrightarrow \sin(2\phi) = 0 \Leftrightarrow \phi = 0, \pi/2, \pi, 3\pi/2, ... \tag{A.90}$$

Substituting these values in Eq. (A.88), we obtain that the radial position of the Lagrangian points satisfies

$$\frac{\partial V_0}{\partial r} + \frac{\partial Q_1}{\partial r} \pm \frac{\partial Q_3}{\partial r} = r\Omega_p^2, \tag{A.91}$$

where $\pm$ refers to the unstable ($\phi = \pi/2, ...$) or stable points ($\phi = 0, ...$), respectively. Considering that the derivatives of both Q_1 and Q_3 are negligible, which is a safe assumption in general, we obtain that the radial location of the Lagrangian points is given by

$$\frac{1}{r}\frac{dV_0}{dr} - \Omega_p^2 = 0 \Leftrightarrow \Omega(r)^2 - \Omega_p^2 = 0 \tag{A.92}$$

which means that these points are located in a circle with radius given by the radius of the Keplerian circular orbit with angular velocity equal to Ω_p. Given that this is the velocity at which the reference frame is rotating, this is called the corotation radius.

Appendix B

Analytical expression for the perturbation to the circular orbit at corotation

In this appendix we present some details regarding the analytical solution for the perturbations to the circular orbit at corotation. The equations of motion (3.48) and (3.49) can be written as

$$\frac{dX}{dt} = \hat{A}X + B, \tag{B.1}$$

in which

$$X^T = (r_1, \phi_1, R_1, \Phi_1), \tag{B.2}$$

with $R_1 = \dot{r}_1$, $\Phi_1 = \dot{\phi}_1$,

$$\hat{A} = \begin{pmatrix} 0 & 0 & 1 & 0 \\ 0 & 0 & 0 & 1 \\ -(\Psi_0'' - \omega_R^2) & -2P_3' \sin(2\phi_i) & 0 & 2\omega_R R_c \\ 0 & \frac{4P_3}{R_C^2}\cos(2\phi_i) & -\frac{2\omega_R}{R_C} & 0 \end{pmatrix}, \tag{B.3}$$

and

$$B^T = \left(0, 0, -C(R_C) - P_3' \cos(2\phi_i), \frac{2P_3}{R_C^2}\sin(2\phi_i)\right). \tag{B.4}$$

The solution, obtained from standard methods, has the form

$$X = X_h + X_p, \tag{B.5}$$

in which

$$X_h = \sum_{i=1}^{4} c_i V_i \exp(\lambda_i t), \tag{B.6}$$

with c_i, V_i, λ_i being constants of integration, eigenvectors and eigenvalues of $\hat{A}$, respectively, and X_p is a constant vector.

The general form of the solutions will depend on Lagrangian point around which the analysis is being made. We observe that independently of the Lagrangian point, it is verified that $\lambda_2 = -\lambda_1$ and $\lambda_4 = -\lambda_3$. For stable Lagrangian points ($\phi_i = 0, \pi$) all the eigenvalues λ_i are purely imaginary, which implies that the solution is given by

$$r_1(t) = C_1 \cos(\mathrm{Im}(\lambda_1)t) + C_2 \cos(\mathrm{Im}(\lambda_3)t), \tag{B.7}$$

$$\phi_1(t) = C_3 \sin(\mathrm{Im}(\lambda_1)t) + C_4 \sin(\mathrm{Im}(\lambda_3)t), \tag{B.8}$$

where the constants C_i are determined in terms of c_i, V_i and the vector X_p. For unstable Lagrangian points ($\phi_i = \pi/2, 3\pi/2$) two of the eigenvalues are real and two are imaginary; the solution is

$$r_1(t) = \tilde{C}_1 \cos(\mathrm{Im}(\lambda_1)t) + \tilde{C}_2(\mathrm{e}^{-\lambda_3 t} + \mathrm{e}^{\lambda_3 t}), \tag{B.9}$$

$$\phi_1(t) = \tilde{C}_3 \sin(\mathrm{Im}(\lambda_1)t) + \tilde{C}_4(\mathrm{e}^{-\lambda_3 t} - \mathrm{e}^{\lambda_3 t}), \tag{B.10}$$

where it was assumed that λ_1, λ_2 are imaginary and λ_3, λ_4 are real and the constants $\tilde{C}_i$ depend on c_i, V_i, X_p. The two solutions have different limits of validity. Around the stable Lagrange points the solution is valid for all times t. On the other hand, around $\phi_i = \pi/2, 3\pi/2$, the unstable points, the solution is valid in a limited range of the time coordinate: the presence of the exponential terms force the values of r_1 and ϕ_1 out of the smallness assumption in which rests the validity of the solution.

Appendix C

Orbital elements in the BH frame

The orbital elements of the S2 star were measured with respect to the frame of reference of the observer, sitting on Earth. To describe the orbit of the star in another reference frame, one needs to convert the orbital elements to that reference frame. One is not expecting that the geometrical orbital elements – the semi-major axis a and the eccentricity e – are altered from reference frame to reference frame, but the angular ones should change.

The perturbing gravitational potential due to the presence of the scalar field cloud was calculated in a reference frame centered in the SMBH in the center of the Galaxy and considering the the z axis was aligned with the direction of the angular momentum of the BH. To convert the orbital parameters from the Earth-based observer's reference frame to the BH-centered reference frame, we'll follow the recipe presented in Ref. [143] which we reproduce here; Fig. C.1 serves as a pictorial guide to this operation:

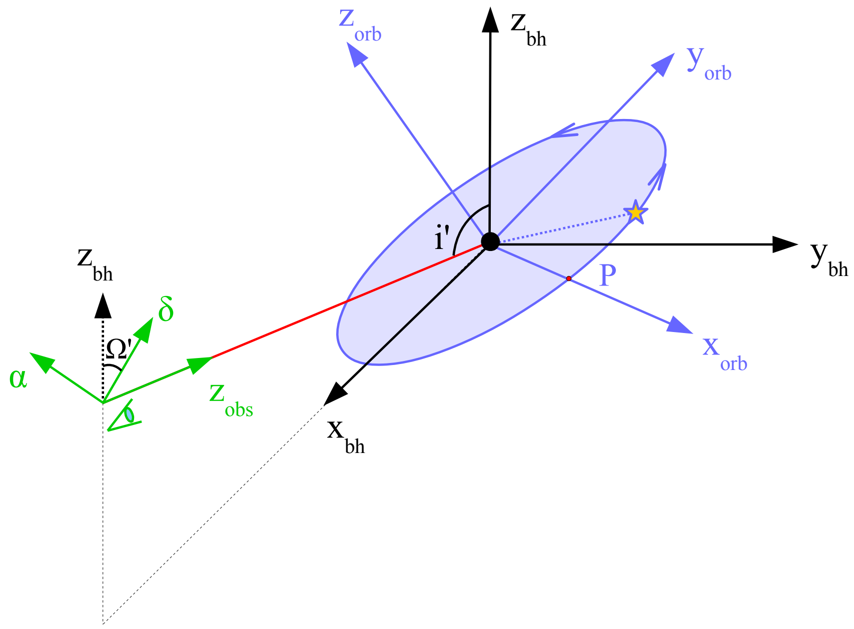

Figure C.1: Representation of the Earth-based reference frame $(\alpha_s, \delta_s, z_{s,obs})$, the reference frame centered in the (x_{bh}, y_{bh}, z_{bh}) and the angles (i', Ω') that relate one with the other. Image taken from Ref. [143].

1. We use orbital elements in the equations[1][167]

$$x = \frac{a(1-e^2)}{1+e\cos f}\left[\cos\Omega\cos(\omega+f) - \sin\Omega\sin(\omega+f)\cos i\right], \tag{C.1}$$

$$y = \frac{a(1-e^2)}{1+e\cos f}\left[\sin\Omega\cos(\omega+f) + \cos\Omega\sin(\omega+f)\cos i\right], \tag{C.2}$$

$$z = \frac{a(1-e^2)}{1+e\cos f}\sin(\omega+f)\sin i, \tag{C.3}$$

$$\dot{x} = -\frac{na}{\sqrt{1-e^2}}\left[\cos\Omega\sin(\omega+f) + \sin\Omega\cos(\omega+f)\cos i + e(\cos\Omega\sin\omega + \sin\Omega\cos\omega\cos i)\right], \tag{C.4}$$

$$\dot{y} = -\frac{na}{\sqrt{1-e^2}}\left[\sin\Omega\sin(\omega+f) - \cos\Omega\cos(\omega+f)\cos i + e(\sin\Omega\sin\omega - \cos\Omega\cos\omega\cos i)\right], \tag{C.5}$$

$$\dot{z} = \frac{na}{\sqrt{1-e^2}}\left[\cos(\omega+f) + e\cos\omega\right]\sin i. \tag{C.6}$$

to the position and velocity of the star in a corresponding Cartesian reference frame; then we use Eq. (B.7) of Ref. [143] to convert to the variables in the Earth-based observer's reference frame – $(\alpha_s, \delta_s, z_{s,obs}, v_{\alpha s}, v_{\delta s}, v_{zs,obs})$ in Fig. C.1;

[1] n is the mean motion – see Eq. (D.6)

2. Then we apply the rotation matrix of eq (1) of Ref. [143]

$$M = \begin{bmatrix} \sin(i'')\sin(\Omega') & \sin(i'')\cos(\Omega') & -\cos(i'') \\ -\cos(\Omega') & \sin(\Omega') & 0 \\ \cos(i'')\sin(\Omega') & \cos(i'')\cos(\Omega') & \sin(i'') \end{bmatrix}, \tag{C.7}$$

to convert $\boldsymbol{r} = (\alpha_s, \delta_s, z_{s,obs})$ and $\dot{\boldsymbol{r}} = (v_{\alpha s}, v_{\delta s}, v_{zs,obs})$ (i.e. the position and velocity of the star in the observer's reference frame) to $\boldsymbol{r}_{BH}$ and $\dot{\boldsymbol{r}}_{BH}$ (the same vectors in the BH-centered reference frame). Notice the angles Ω' and $i'' = i' + 3\pi/2$ (see Fig.C.1), they are related to the direction of the BH's spin with respect to the observer's reference frame.

3. Use $\boldsymbol{r}_{BH}$ and $\dot{\boldsymbol{r}}_{BH}$ to obtain the orbital parameters in the BH-centered frame.

Having calculated the vectors $\boldsymbol{r}_{BH}$ and $\dot{\boldsymbol{r}}_{BH}$, we proceed to calculate orbital parameters in the BH frame. We start by calculating the orbital angular momentum vector in the BH frame

$$\boldsymbol{h} = \boldsymbol{r}_{BH} \times \dot{\boldsymbol{r}}_{BH} \tag{C.8}$$

and the eccentricity vector

$$\boldsymbol{e} = \dot{\boldsymbol{r}}_{BH} \times \boldsymbol{h} - \frac{\boldsymbol{r}_{BH}}{||\boldsymbol{r}_{BH}||}. \tag{C.9}$$

Then, one can determine the vector $\boldsymbol{n}$,

$$\boldsymbol{n} = (0, 0, 1) \times \boldsymbol{h}, \tag{C.10}$$

which points towards the ascending node. Having all these vectors, one can start calculating the orbital parameters. The eccentricity is the norm of the eccentricity vector

$$e = ||\boldsymbol{e}||. \tag{C.11}$$

The inclination can be found from the relation

$$\cos i = \frac{h_z}{||\boldsymbol{h}||}; \tag{C.12}$$

the semi-major axis can be obtained from the relation

$$\frac{1}{a} = \frac{2}{||\boldsymbol{r}_{BH}||} - ||\dot{\boldsymbol{r}}_{BH}||^2. \tag{C.13}$$

The longitude of the ascending node and the argument of the periapsis can be found from

$$\Omega = \begin{cases} \arccos \frac{n_x}{||\boldsymbol{n}||} & \text{for } n_y \geq 0, \\ 2\pi - \arccos \frac{n_x}{||\boldsymbol{n}||} & \text{for } n_y < 0, \end{cases} \tag{C.14}$$

where n_y is the y-component of the vector in Eq. (C.10) and

$$\omega = \begin{cases} \arccos \frac{\boldsymbol{n}\cdot\boldsymbol{e}}{||\boldsymbol{n}||||\boldsymbol{e}||} & \text{for } e_z \geq 0, \\ 2\pi - \arccos \frac{\boldsymbol{n}\cdot\boldsymbol{e}}{||\boldsymbol{n}||||\boldsymbol{e}||} & \text{for } e_z < 0, \end{cases} \tag{C.15}$$

where n_z is the z-component of the eccentricity vector.

The orbital elements and the direction of the BH's angular momentum

The orbital elements of the S2 star, measured in the Earth-based observer's frame are given by ([141])

$$\begin{aligned} &a_0 = 2.5 \times 10^4, \quad e_0 = 0.88473, \quad i_0 = 133.817^{\text{o}} \\ &\omega_0 = 66.12^{\text{o}}, \quad \Omega_0 = 227.82^{\text{o}}, \end{aligned} \tag{C.16}$$

where the value of the semi-major axis is in the normalized units of Eq. (2.27). In order to translate these orbital elements to the BH-centered reference frame, we have to make a fundamental assumption, i.e., the choice of the direction of the BH's spin. From Eq. (C.7), which contains the matrix with which the transformation between reference frames is performed, we see that such transformation depends on the angles Ω' and $i'' = i' + 3\pi/2$ (see Fig.C.1), which refer to the direction of the BH's spin.

The direction of the BH spin is not a well established quantity. Using the assumption made by Ref. [143] for the values of the angles i' and Ω', we run the aforementioned recipe and we obtain

$$a_0 = 2.5 \times 10^4, \quad e_0 = 0.88473, \quad i_0 = 90.98^{\mathrm{o}}$$
$$\omega_0 = 81.60^{\mathrm{o}}, \quad \Omega_0 = 254.191^{\mathrm{o}}. \tag{C.17}$$

Appendix D

Keplerian orbits formalism

Using the re-scaled distance and time coordinates (Eq. (2.27)), the equation of motion of a mass in a Keplerian gravitational field reads

$$\frac{d^2\boldsymbol{r}}{dt^2} = -\frac{\boldsymbol{r}}{r^3}, \tag{D.1}$$

where we consider a reference frame centered in the SMBH (in the "center of the galaxy", let's say) with the z-axis aligned with the angular momentum of the SMBH. In a system of cartesian coordinates, the orbiting mass will follow a path described by

$$\begin{cases} x &= r[\cos\Omega\cos(\omega+f) - \sin\Omega\sin(\omega+f)\cos i], \\ y &= r[\sin\Omega\cos(\omega+f) + \cos\Omega\sin(\omega+f)\cos i], \\ z &= r\sin(\omega+f)\sin i, \end{cases} \tag{D.2}$$

where

$$r = \frac{a(1-e^2)}{(1+e\cos f)}. \tag{D.3}$$

The parameters $(a, e, i, \Omega, \omega)$ are the orbital elements characterizing the orbit; the size and the shape are given by the values of the eccentricity (e) and the semi-major axis (a), the orientation of the orbit is given by the values of the inclination (i) and the longitude of the ascending node (Ω); finally the position of the star in the orbit is given by the argument of the periapsis (ω) and by the true anomaly (f). Only the latter value is not constant for a Keplerian orbit: the true anomaly is $f = 0$ when the star is in the periastron and $f = \pi$ in the apoastron. The true anomaly is related to time by the Kepler equation

$$\mathcal{M} = E - e\sin E, \tag{D.4}$$

where

$$\mathcal{M} = \mathcal{M}_0 + n(t - t_0), \tag{D.5}$$

is the mean anomaly, $\mathcal{M}_0$ is the mean anomaly at epoch[1],

$$n = \sqrt{\frac{1}{a^3}}, \tag{D.6}$$

is the mean motion[2] and E is the eccentric anomaly, which is related to the true anomaly by

$$\tan\frac{f}{2} = \sqrt{\frac{1+e}{1-e}}\tan\frac{E}{2}. \tag{D.7}$$

D.1 Perturbing a Keplerian orbit

A perturbed Keplerian orbit is described by the equation of motion

$$\frac{d^2\boldsymbol{r}}{dt^2} + \frac{\boldsymbol{r}}{r^3} = \boldsymbol{F}_{\rm pert}, \tag{D.8}$$

where $\boldsymbol{F}_{\rm pert}$ represents the perturbing force. Following the osculating conics method (see, e.g., Ref. [167]), the perturbed orbit will be described by the same expressions of Eq. (D.2) but with

[1] If we fix t_0 to be the time of periapsis passage, then one can set $\mathcal{M}_0 = 0$ implying that $\mathcal{M}(t = t_0 + T/2) = \pi$, which corresponds to the value in the apoapsis.

[2] The mean motion is defined by $n = 2\pi/T$, where T is the period of the orbit. Before re-scaling, the mean motion reads $n = \sqrt{GM/a^3}$ which becomes $\bar{n} = \sqrt{1/\bar{a}^3}$ after re-scaling.

orbital parameters varying according to

$$\frac{da}{dt} = \frac{2}{n\sqrt{1-e^2}}\left(eF_R \sin f + F_T \frac{p}{r}\right), \tag{D.9}$$

$$\frac{de}{dt} = \frac{\sqrt{1-e^2}}{na}\left[F_R \sin f + F_T\left(\cos f + \cos E\right)\right], \tag{D.10}$$

$$\frac{di}{dt} = \frac{r\cos(f+\omega)}{na^2\sqrt{1-e^2}}F_N, \tag{D.11}$$

$$\frac{d\Omega}{dt} = \frac{r\sin(f+\omega)}{na^2\sqrt{1-e^2}\sin i}F_N, \tag{D.12}$$

$$\frac{d\omega}{dt} = -\cos i\frac{d\Omega}{dt} + \frac{\sqrt{1-e^2}}{nae}\left[-F_R\cos f + F_T\left(1+\frac{r}{p}\right)\sin f\right], \tag{D.13}$$

$$\frac{d\mathcal{M}_0}{dt} = -\sqrt{1-e^2}\left(\frac{d\omega}{dt} + \cos i\frac{d\Omega}{dt}\right) - \frac{2r}{na^2}F_R, \tag{D.14}$$

and the mean anomaly of the perturbed motion looks like

$$\mathcal{M} = \mathcal{M}_0 + \int_{t_0}^{t} n(t')dt', \tag{D.15}$$

where $p = a(1-e^2)$ is the semi latus rectum and

$$\begin{cases} F_R &= \hat{n}\cdot \boldsymbol{F}_{\text{pert}}, \\ F_T &= (\hat{k}\times\hat{n})\cdot \boldsymbol{F}_{\text{pert}}, \\ F_N &= \hat{k}\cdot \boldsymbol{F}_{\text{pert}}, \end{cases} \tag{D.16}$$

are the radial, transversal and normal (to the orbit) components of the perturbing force. Notice that $\hat{n} = \boldsymbol{r}/r$ is the radial unit vector and $\hat{k}$ is the unit vector orthogonal to the instantaneous orbital plane; the unit vector $\hat{k}$ can be written as

$$\hat{k} = \frac{\boldsymbol{r}\times\dot{\boldsymbol{r}}}{|\boldsymbol{r}\times\dot{\boldsymbol{r}}|}. \tag{D.17}$$

D.2 Perturbation due to the presence of a scalar-field cloud

Using the perturbing force expression due to the complex scalar-field of Chapter 4

$$\boldsymbol{F}_{\text{pert}} = \Lambda\nabla\left[P_1(r) + P_2(r)\cos^2\theta\right], \tag{D.18}$$

in Eq. (D.16), we obtain the following components of the force

$$F_R = \sin^2(i)\sin^2(f+\omega)P_2'(r) + P_1'(r), \tag{D.19}$$

$$F_T = -\frac{\sin^2(i)(e\cos(f)+1)\sin(2(f+\omega))P_2(r)}{a\,(e^2-1)}, \tag{D.20}$$

$$F_N = -\frac{\sin(2i)(e\cos(f)+1)\sin(f+\omega)P_2(r)}{a\,(e^2-1)}, \tag{D.21}$$

where the prime $'$ stands for derivative with respect to the radial coordinate. Using these, the equations governing the time-variation of the orbital parameters (see Eqs. (D.9) to (D.14)) due to the scalar-field cloud are

$$\frac{da}{dt}\frac{dt}{df} = 2a^2(1-e^2)\,[T_1] + 2a^3e(1-e^2)\sin(f)\,[R_2]\,, \tag{D.22}$$

$$\frac{de}{dt}\frac{dt}{df} = a^2\left(e^2-1\right)^2\left(\left(e\cos^2(f)+e+2\cos(f)\right)[T_3] + \sin(f)\,[R_2]\right), \tag{D.23}$$

$$\frac{di}{dt}\frac{dt}{df} = a^2\left(e^2-1\right)^2\cos(f+\omega)\,[N_3]\,, \tag{D.24}$$

$$\frac{d\Omega}{dt}\frac{dt}{df} = a^2\left(e^2-1\right)^2\csc(i)\sin(f+\omega)\,[N_3]\,, \tag{D.25}$$

$$\begin{aligned}\frac{d\omega}{dt}\frac{dt}{df} = &-\left\{\frac{a^2(e^2-1)^2(-e\sin(f)\cos(f)-2\sin(f))}{e}\right\}[T_3] - \left\{\frac{a^2(e^2-1)^2\cos(f)}{e}\right\}[R_2] \\ &-\left\{a^2(e^2-1)^2\cot(i)\sin(f+\omega)\right\}[N_3]\,,\end{aligned} \tag{D.26}$$

$$\frac{d\mathcal{M}_0}{dt}\frac{dt}{df} = \frac{a^2\left(1-e^2\right)^{5/2}}{e}\left(\left(e\cos^2(f)-2e+\cos(f)\right)[R_3] - \sin(f)(e\cos(f)+2)\,[T_3]\right), \tag{D.27}$$

where

$$T_1 = -\frac{\sin^2(i)\sin(2(f+\omega))}{a\,(e^2-1)}P_2(f), \tag{D.28}$$

$$T_3 = -\frac{\sin^2(i)\sin(2(f+\omega))}{a\,(e^2-1)}\left[\frac{P_2(f)}{(e\cos(f)+1)^2}\right], \tag{D.29}$$

$$N_3 = -\frac{\sin(2i)\sin(f+\omega)}{a\,(e^2-1)}\left[\frac{P_2(f)}{(e\cos(f)+1)^2}\right], \tag{D.30}$$

$$R_2 = \left[\frac{P_1'(r)}{(e\cos(f)+1)^2}\right] + \sin^2(i)\sin^2(f+\omega)\left[\frac{P_2'(r)}{(e\cos(f)+1)^2}\right], \tag{D.31}$$

$$R_3 = \left[\frac{P_1'(r)}{(e\cos(f)+1)^3}\right] + \sin^2(i)\sin^2(f+\omega)\left[\frac{P_2'(r)}{(e\cos(f)+1)^3}\right]. \tag{D.32}$$

Appendix E

Describing an extended mass in the center of the galaxy

Theoretical studies regarding the distribution of stars in the center of galaxies – there are stellar dynamics studies that approached the problem ([168–170]) and N-body confirmation ([171–173]) – in which a density distribution of stars around the BH may be described by a power-law function, describing a stellar cusp around a BH, appear to be validated by the observational results obtained so far (see, e.g. Ref. [174] and references). A discussion of these matters is beyond the scope of this thesis, but in order to estimate the orders of magnitude associated with the effects that may come from the population of stars in the center of the galaxy, we will use the simple approach of modeling the density of the population of stars by a power law (as in [147, 149, 150]). We will consider that the mean density in the galatic center is given by

$$\rho(r) = \rho_0 \left(\frac{r}{r_0}\right)^{-\gamma} \tag{E.1}$$

which ρ_0 the stellar density at the characteristic radius of normalization r_0. The enclosed mass, i.e., the mass of the stars that are described by this density function are given by

$$M(r) = 4\pi \int_0^r \rho(x) x^2 dx = \frac{4\pi\rho_0 r_0^3}{3-\gamma}\left(\frac{r}{r_0}\right)^{3-\gamma}, \quad \gamma < 3. \tag{E.2}$$

Considering that $r_0 = 0.01$ pc the total mass stellar mass within this radius is given by

$$M_*(r_0) = \frac{4\pi\rho_0 r_0^3}{3-\gamma}, \tag{E.3}$$

so that we can write that the average galactic potential is given by

$$U_{\rm gal}(r) = -\frac{M_*(r_0)}{(2-\gamma)r_0}\left(\frac{r}{r_0}\right)^{2-\gamma}, \quad \gamma \neq 2. \tag{E.4}$$

So, the resulting force that perturbs the Keplerian orbit is ($F = \nabla U_{\rm gal}$)

$$F_R = -\frac{M_*(r_0)}{r_0^2}\left(\frac{a-ae^2}{r_0(1+e\cos(f))}\right)^{1-\gamma}, \quad F_T = F_N = 0. \tag{E.5}$$

Given that Ref. [147] also analyses the S2 star, we are going to follow their choices for the exponents γ and the values of the enclosed mass $M_*(r_0)$; so, we will consider two cases

$$\begin{cases} \gamma_l = 1.5, \quad M_*(r_0) = 2\times 10^3 M_\odot, \\ \gamma_h = 2.1, \quad M_*(r_0) = 2\times 10^4 M_\odot, \end{cases} \tag{E.6}$$

where the subscript l and h corresponds to the type of stars that are considered to source the density distribution under analysis. Since stars with different masses get distributed with different density profiles, and given the uncertainty associated with modelling the Galactic potential, these two cases aim to illustrate two extremal cases.

Appendix F

Numerical details about the SP system

F.1 Testing the code

We evolve the two components of our two-body system using different techniques. To solve SP system of equations, of the form of Eqs. (5.23) and (5.24), we use a centered finite difference stencil to write the derivatives. Particularly, at a generic point $u_j = j\Delta u$, we discretize the first derivatives as

$$\frac{\partial H}{\partial u} = \frac{H_{j+1} - H_{j-1}}{2\Delta u}, \tag{F.1}$$

and the second derivatives as

$$\frac{\partial^2 H}{\partial u^2} = \frac{H_{j+1} - 2H_j + H_{j-1}}{(\Delta u)^2}, \tag{F.2}$$

for a general function $H(u)$, indicating $H(u_j) = H_j$. Having discretized the equations, we apply the iterated Crank-Nicolson method with two iterations, following the conclusions of Ref. [156]. To solve the equations of motion of the point-particle, which can be cast in the generic form $dv/dt = G(t, v)$, we use Euler's method, with the evolution step given by

$$\begin{cases} v_{n+1} &= v_n + \Delta t G(t_n, v_n), \\ t_{n+1} &= t_n + \Delta t, \end{cases} \tag{F.3}$$

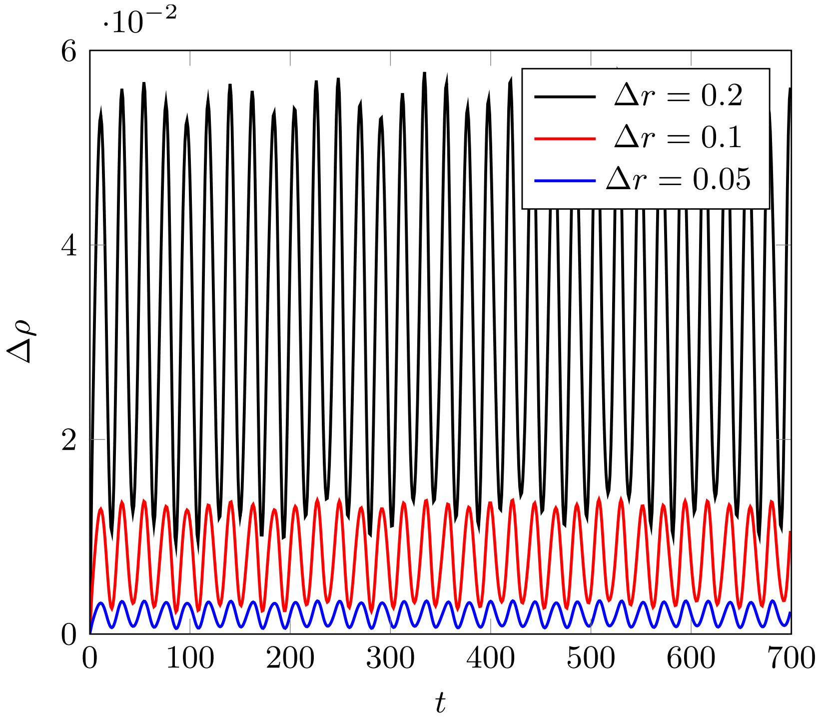

Figure F.1: Representing the evolution of the quantity $\Delta\rho$ of Eq. (F.5) using $\Delta t = 10^{-3}$ and with three different grid values. We observe that the maximum value of $\Delta\rho$ in each simulation is related to the grid spacing as $(\Delta r)^2$.

and the two-step Adams-Bashforth method given by

$$\begin{cases} v_{n+2} &= v_{n+1} + \frac{3}{2}\Delta t G(t_{n+1}, v_{n+1}) - \frac{1}{2}\Delta t G(t_n, v_n), \\ t_{n+2} &= t_{n+1} + \Delta t. \end{cases} \tag{F.4}$$

Evolving a stationary scalar field solution

Using a timestep $\Delta t = 10^{-3}$, we run a test with three different grid spacings - $\Delta r = 0.2, 0.1, 0.05$. To quantify the effect of the grid spacing in the evolution of the field, define

$$\Delta\rho(t) = \max\left(|\rho_E(r) - \rho(t,r)|\right) , \tag{F.5}$$

where $\rho_E(r) = f_E f_E^*$ is the equilibrium density of the scalar field (see Eq. (5.8)) and $\rho(t,r)$ is the density of the field that is evolved in time using our code. The results of this evolution are shown in Fig. F.1. The test allows us to conclude that with decreasing resolution, the magnitude of the deviations from the initial stationary configuration decreases. Moreover, we obtain that $\max\left[\Delta\rho\right] \sim (\Delta r)^2$.

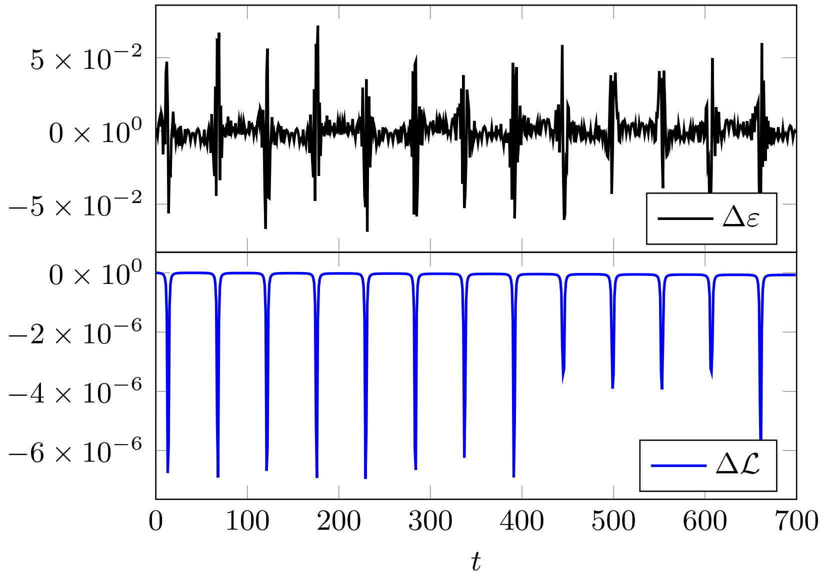

Figure F.2: Represening the evolution of the energy and angular momentum per unit mass (see Eq. (F.6)) for the simulation $Y3V03$. This simulation was run with $\Delta t = 10^{-3}$ and $\Delta r = 0.1$.

Testing the code evolving the orbiting particle

The evolution of the particle will be made with the same time step as the one used for the SP-equations. To correctly describe this evolution, the code has to guarantee the conservation of the energy and angular momentum per unit mass for the control tests. To visualize that conservation, we calculate the following quantities

$$\Delta\varepsilon = \frac{\varepsilon(t) - \varepsilon(0)}{\varepsilon(0)}, \quad \Delta\mathcal{L} = \frac{\mathcal{L}(t) - \mathcal{L}(0)}{\mathcal{L}(0)}, \tag{F.6}$$

where $\varepsilon(0)$ and $\mathcal{L}(0)$ represent the initial energy and angular momentum per unit mass, respectively. In Fig. F.2 we show the evolution of these quantities for the control test $Y3V03$. We observe that both the energy and the angular momentum are conserved, in the worst case, up to the percent level.

F.2 Discretizing the Dirac delta

In order to describe the perturbing mass orbiting the scalar configuration as a point particle, it is necessary to use the Dirac delta. To describe it in a numerical grid, we follow an approach used in previous works (see Ref. [175] and references therein) in which the construction of the discretized version of the Dirac delta is made considering that its defining feature is integrability.

This means that we obtain the discretized Dirac delta by studying the expression

$$\int_{-\infty}^{\infty} f(x)\delta(x - X_0)dx = f(X_0) \tag{F.7}$$

for some "well-behaved" (continuous with continuous derivatives) function $f(x)$. The finite difference version of the previous expression is given by

$$dx \sum_i f_i \delta_i = f_{i*} \tag{F.8}$$

where f_i and δ_i represent the values of function f and the Dirac delta, respectively, at the grid point i. In our case it suffices to consider that the point X_0 is always a grid point such that $X_0/dx = i*$. With this setup, we can say that the only point of the grid in which the Dirac delta takes a non-zero value is precisely the grid point corresponding to X_0. This implies that the finite difference formula of Eq. (F.8) can be written as

$$dx f(X_0)\delta_{i*} = f(X_0), \tag{F.9}$$

from where we can read that the Dirac delta has the following finite difference representation

$$\delta_i = \begin{cases} \frac{1}{dx}, & i = i* \\ 0, & i \neq i* \end{cases}. \tag{F.10}$$

This definition agrees, in the respective limits, with the simplest definition for the Dirac delta of [175]. We decided to use a one-point-only discretized Dirac delta for two reasons: a) it works well; b) given the scales of the problem at hand, we want to reinforce as much as possible the localized nature of the perturbing mass.

Bibliography

[1] Serguei Chatrchyan, Vardan Khachatryan, Albert M Sirunyan, Armen Tumasyan, Wolfgang Adam, Ernest Aguilo, Thomas Bergauer, M Dragicevic, J Erö, C Fabjan, et al. Observation of a new boson at a mass of 125 gev with the cms experiment at the lhc. *Physics Letters B*, 716(1):30–61, 2012.

[2] Georges Aad, Tatevik Abajyan, B Abbott, J Abdallah, S Abdel Khalek, Ahmed Ali Abdelalim, O Abdinov, R Aben, B Abi, M Abolins, et al. Observation of a new particle in the search for the standard model higgs boson with the atlas detector at the lhc. *Physics Letters B*, 716(1):1–29, 2012.

[3] Dimitri V Nanopoulos, Keith A Olive, and M Srednicki. After primordial inflation. *Physics Letters B*, 127(1-2):30–34, 1983.

[4] Howard Baer, Ki-Young Choi, Jihn E Kim, and Leszek Roszkowski. Dark matter production in the early universe: beyond the thermal wimp paradigm. *Physics Reports*, 555: 1–60, 2015.

[5] Bharat Ratra and Philip JE Peebles. Cosmological consequences of a rolling homogeneous scalar field. *Physical Review D*, 37(12):3406, 1988.

[6] Robert R Caldwell, Rahul Dave, and Paul J Steinhardt. Cosmological imprint of an energy component with general equation of state. *Physical Review Letters*, 80(8):1582, 1998.

[7] Emanuele Berti, Enrico Barausse, Vitor Cardoso, Leonardo Gualtieri, Paolo Pani, Ulrich Sperhake, Leo C Stein, Norbert Wex, Kent Yagi, Tessa Baker, et al. Testing general relativity with present and future astrophysical observations. *Classical and Quantum Gravity*, 32(24):243001, 2015.

[8] Roberto D Peccei and Helen R Quinn. Cp conservation in the presence of pseudoparticles. *Physical Review Letters*, 38(25):1440, 1977.

[9] Steven Weinberg. A new light boson? *Physical Review Letters*, 40(4):223, 1978.

[10] Frank Wilczek. Problem of strong p and t invariance in the presence of instantons. *Physical Review Letters*, 40(5):279, 1978.

[11] Peter Svrcek and Edward Witten. Axions in string theory. *Journal of High Energy Physics*, 2006(06):051, 2006.

[12] Asimina Arvanitaki, Savas Dimopoulos, Sergei Dubovsky, Nemanja Kaloper, and John March-Russell. String axiverse. *Physical Review D*, 81(12):123530, 2010.

[13] C Lohmeyer, J Dargert, M Cunningham, M Harkness, E Levenson-Falk, S Mumford, A Kapitulnik, A Arvanitaki, I Lee, E Smith, et al. Progress on the ariadne axion experiment. In *Microwave Cavities and Detectors for Axion Research: Proceedings of the 2nd International Workshop*, volume 211, page 151. Springer, 2018.

[14] Paola Arias, Davide Cadamuro, Mark Goodsell, Joerg Jaeckel, Javier Redondo, and Andreas Ringwald. Wispy cold dark matter. *Journal of Cosmology and Astroparticle Physics*, 2012(06):013, 2012.

[15] Lam Hui, Jeremiah P Ostriker, Scott Tremaine, and Edward Witten. Ultralight scalars as cosmological dark matter. *Physical Review D*, 95(4):043541, 2017.

[16] R Ballou, G Deferne, M Finger Jr, M Finger, L Flekova, J Hosek, S Kunc, K Macuchova, KA Meissner, P Pugnat, et al. New exclusion limits on scalar and pseudoscalar axionlike particles from light shining through a wall. *Physical Review D*, 92(9):092002, 2015.

[17] E Armengaud, FT Avignone, M Betz, P Brax, P Brun, Giovanni Cantatore, JM Carmona, GP Carosi, F Caspers, S Caspi, et al. Conceptual design of the international axion observatory (iaxo). *Journal of Instrumentation*, 9(05):T05002, 2014.

[18] N Du, N Force, R Khatiwada, E Lentz, R Ottens, LJ Rosenberg, Gray Rybka, G Carosi, N Woollett, D Bowring, et al. Search for invisible axion dark matter with the axion dark matter experiment. *Physical review letters*, 120(15):151301, 2018.

[19] Renée Hlozek, Daniel Grin, David JE Marsh, and Pedro G Ferreira. A search for ultralight axions using precision cosmological data. *Physical Review D*, 91(10):103512, 2015.

[20] David JE Marsh. Axion cosmology. *Physics Reports*, 643:1–79, 2016.

[21] Asimina Arvanitaki and Sergei Dubovsky. Exploring the string axiverse with precision black hole physics. *Physical Review D*, 83(4):044026, 2011.

[22] Steven L Liebling and Carlos Palenzuela. Dynamical boson stars. *Living Reviews in Relativity*, 20(1):5, 2017.

[23] Phillippe Jetzer. Boson stars. *Physics Reports*, 220(4):163–227, 1992.

[24] Andrew R Liddle and Mark S Madsen. The structure and formation of boson stars. *International Journal of Modern Physics D*, 1(01):101–143, 1992.

[25] Eckehard W Mielke and Franz E Schunck. Boson stars: Early history and recent prospects. *arXiv preprint gr-qc/9801063*, 1998.

[26] Franz E Schunck and Eckehard W Mielke. General relativistic boson stars. *Classical and Quantum Gravity*, 20(20):R301, 2003.

[27] Theodoros JM Zouros and Douglas M Eardley. Instabilities of massive scalar perturbations of a rotating black hole. *Annals of physics*, 118(1):139–155, 1979.

[28] Steven Detweiler. Klein-gordon equation and rotating black holes. *Physical Review D*, 22(10):2323, 1980.

[29] Vitor Cardoso and Shijun Yoshida. Superradiant instabilities of rotating black branes and strings. *Journal of High Energy Physics*, 2005(07):009, 2005.

[30] Sam R Dolan. Instability of the massive klein-gordon field on the kerr spacetime. *Physical Review D*, 76(8):084001, 2007.

[31] David J Kaup. Klein-gordon geon. *Physical Review*, 172(5):1331, 1968.

[32] Remo Ruffini and Silvano Bonazzola. Systems of self-gravitating particles in general relativity and the concept of an equation of state. *Physical Review*, 187(5):1767, 1969.

[33] Eckehard W Mielke and Reinhard Scherzer. Geon-type solutions of the nonlinear heisenberg-klein-gordon equation. *Physical Review D*, 24(8):2111, 1981.

[34] JD Breit, S Gupta, and A Zaks. Cold bose stars. *Physics Letters B*, 140(5-6):329–332, 1984.

[35] R Friedberg, TD Lee, and Y Pang. Mini-soliton stars. *Physical Review D*, 35(12):3640, 1987.

[36] Marcelo Gleiser. Stability of boson stars. *Physical Review D*, 38(8):2376, 1988.

[37] Philippe Jetzer. Dynamical instability of bosonic stellar configurations. *Nuclear Physics B*, 316(2):411–428, 1989.

[38] Marcelo Gleiser and Richard Watkins. Gravitational stability of scalar matter. *Nuclear Physics B*, 319(3):733–746, 1989.

[39] Ph Jetzer. Stability of excited bosonic stellar configurations. *Physics Letters B*, 222(3-4): 447–452, 1989.

[40] Edward Seidel and Wai-Mo Suen. Dynamical evolution of boson stars: Perturbing the ground state. *Physical Review D*, 42(2):384, 1990.

[41] Jayashree Balakrishna, Edward Seidel, and Wai-Mo Suen. Dynamical evolution of boson stars. ii. excited states and self-interacting fields. *Physical Review D*, 58(10):104004, 1998.

[42] F Siddhartha Guzman. Evolving spherical boson stars on a 3d cartesian grid. *Physical Review D*, 70(4):044033, 2004.

[43] Edward Seidel and Wai-Mo Suen. Oscillating soliton stars. *Physical review letters*, 66 (13):1659, 1991.

[44] GH Derrick. Comments on nonlinear wave equations as models for elementary particles. *Journal of Mathematical Physics*, 5(9):1252–1254, 1964.

[45] Miguel Alcubierre, Ricardo Becerril, F Siddhartha Guzmán, Tonatiuh Matos, Darío Núñez, and L Arturo Urena-López. Numerical studies of ϕ2-oscillatons. *Classical and Quantum Gravity*, 20(13):2883, 2003.

[46] Hirotada Okawa, Vitor Cardoso, and Paolo Pani. Collapse of self-interacting fields in asymptotically flat spacetimes: do self-interactions render minkowski spacetime unstable? *Physical Review D*, 89(4):041502, 2014.

[47] Philippe Grandclément, Gyula Fodor, and Péter Forgács. Numerical simulation of oscillatons: Extracting the radiating tail. *Physical Review D*, 84(6):065037, 2011.

[48] Don N Page. Classical and quantum decay of oscillations: Oscillating self-gravitating real scalar field solitons. *Physical Review D*, 70(2):023002, 2004.

[49] Gyula Fodor, Peter Forgacs, and Márk Mezei. Mass loss and longevity of gravitationally bound oscillating scalar lumps (oscillatons) in d dimensions. *Physical Review D*, 81(6): 064029, 2010.

[50] Edward Seidel and Wai-Mo Suen. Formation of solitonic stars through gravitational cooling. *Physical review letters*, 72(16):2516, 1994.

[51] F Siddhartha Guzman and L Arturo Urena-López. Evolution of the schrödinger-newton system for a self-gravitating scalar field. *Physical Review D*, 69(12):124033, 2004.

[52] F Siddhartha Guzman and L Arturo Urena-Lopez. Gravitational cooling of self-gravitating bose condensates. *The Astrophysical Journal*, 645(2):814, 2006.

[53] Robert Ferrell and Marcelo Gleiser. Gravitational atoms: Gravitational radiation from excited boson stars. *Physical Review D*, 40(8):2524, 1989.

[54] L Arturo Ureña-López, Tonatiuh Matos, and Ricardo Becerril. Inside oscillatons. *Classical and Quantum Gravity*, 19(23):6259, 2002.

[55] Richard Brito, Vitor Cardoso, and Paolo Pani. Superradiance. *Lect. Notes Phys*, 906(1): 1501–06570, 2015.

[56] Helvi Witek, Vitor Cardoso, Akihiro Ishibashi, and Ulrich Sperhake. Superradiant instabilities in astrophysical systems. *Physical Review D*, 87(4):043513, 2013.

[57] Hirotada Okawa, Helvi Witek, and Vitor Cardoso. Black holes and fundamental fields in numerical relativity: initial data construction and evolution of bound states. *Physical Review D*, 89(10):104032, 2014.

[58] Juan Barranco, Argelia Bernal, Juan Carlos Degollado, Alberto Diez-Tejedor, Miguel Megevand, Miguel Alcubierre, Darío Núñez, and Olivier Sarbach. Schwarzschild black holes can wear scalar wigs. *Physical review letters*, 109(8):081102, 2012.

[59] Nicolas Sanchis-Gual, Juan Carlos Degollado, Pedro J Montero, and José A Font. Quasistationary solutions of self-gravitating scalar fields around black holes. *Physical Review D*, 91(4):043005, 2015.

[60] Carlos AR Herdeiro and Eugen Radu. Kerr black holes with scalar hair. *Physical review letters*, 112(22):221101, 2014.

[61] Carlos AR Herdeiro and Eugen Radu. Asymptotically flat black holes with scalar hair: a review. *International Journal of Modern Physics D*, 24(09):1542014, 2015.

[62] Shahar Hod. Stationary scalar clouds around rotating black holes. *Physical Review D*, 86(10):104026, 2012.

[63] Carolina L Benone, Luís CB Crispino, Carlos Herdeiro, and Eugen Radu. Kerr-newman scalar clouds. *Physical Review D*, 90(10):104024, 2014.

[64] Sam R Dolan. Superradiant instabilities of rotating black holes in the time domain. *Physical Review D*, 87(12):124026, 2013.

[65] João G Rosa and Thomas W Kephart. Stimulated axion decay in superradiant clouds around primordial black holes. *Physical review letters*, 120(23):231102, 2018.

[66] B Garbrecht and JI McDonald. Axion configurations around pulsars. *Journal of Cosmology and Astroparticle Physics*, 2018(07):044, 2018.

[67] Taishi Ikeda, Richard Brito, and Vitor Cardoso. Blasts of light from axions. *Physical Review Letters*, 122(8):081101, 2019.

[68] Benjamin P Abbott, Richard Abbott, TD Abbott, MR Abernathy, Fausto Acernese, Kendall Ackley, Carl Adams, Thomas Adams, Paolo Addesso, RX Adhikari, et al. Observation of gravitational waves from a binary black hole merger. *Physical review letters*, 116(6):061102, 2016.

[69] Miguel Bezares and Carlos Palenzuela. Gravitational waves from dark boson star binary mergers. *Classical and Quantum Gravity*, 35(23):234002, 2018.

[70] Carlos Palenzuela, Paolo Pani, Miguel Bezares, Vitor Cardoso, Luis Lehner, and Steven Liebling. Gravitational wave signatures of highly compact boson star binaries. *Physical Review D*, 96(10):104058, 2017.

[71] Vitor Cardoso, Seth Hopper, Caio FB Macedo, Carlos Palenzuela, and Paolo Pani. Gravitational-wave signatures of exotic compact objects and of quantum corrections at the horizon scale. *Physical review D*, 94(8):084031, 2016.

[72] Huai-Ke Guo, Kuver Sinha, and Chen Sun. Probing boson stars with extreme mass ratio inspirals. *arXiv preprint arXiv:1904.07871*, 2019.

[73] Noah Sennett, Tanja Hinderer, Jan Steinhoff, Alessandra Buonanno, and Serguei Ossokine. Distinguishing boson stars from black holes and neutron stars from tidal interactions in inspiraling binary systems. *Physical Review D*, 96(2):024002, 2017.

[74] MI Krivoruchenko, F Šimkovic, and Amand Faessler. Constraints for weakly interacting light bosons from existence of massive neutron stars. *Physical Review D*, 79(12):125023, 2009.

[75] Susana Valdez-Alvarado, Carlos Palenzuela, Daniela Alic, and L Arturo Ureña-López. Dynamical evolution of fermion-boson stars. *Physical Review D*, 87(8):084040, 2013.

[76] Richard Brito, Vitor Cardoso, and Hirotada Okawa. Accretion of dark matter by stars. *Physical review letters*, 115(11):111301, 2015.

[77] Richard Brito, Vitor Cardoso, Caio FB Macedo, Hirotada Okawa, and Carlos Palenzuela. Interaction between bosonic dark matter and stars. *Physical Review D*, 93(4):044045, 2016.

[78] AB Henriques, Andrew R Liddle, and RG Moorhouse. Combined boson-fermion stars. *Physics Letters B*, 233(1-2):99–106, 1989.

[79] AB Henriques, Andrew R Liddle, and RG Moorhouse. Combined boson-fermion stars: configurations and stability. *Nuclear Physics B*, 337(3):737–761, 1990.

[80] Luís M Lopes and Alfredo B Henriques. Boson-fermion stars: going to larger boson masses. *Physics Letters B*, 285(1-2):80–84, 1992.

[81] Alfredo B Henriques and Luís E Mendes. Boson–fermion stars: Exploring different configurations. *Astrophysics and Space Science*, 300(4):367–379, 2005.

[82] FH Vincent, Z Meliani, P Grandclément, E Gourgoulhon, and O Straub. Imaging a boson star at the galactic center. *Classical and Quantum Gravity*, 33(10):105015, 2016.

[83] M Gracia-Linares and FS Guzman. Accretion of supersonic winds on boson stars. *Physical Review D*, 94(6):064077, 2016.

[84] Caio FB Macedo, Tom Stratton, Sam Dolan, and Luís CB Crispino. Spectral lines of extreme compact objects. *Physical Review D*, 98(10):104034, 2018.

[85] F Siddhartha Guzmán. Accretion disk onto boson stars: A way to supplant black hole candidates. *Physical Review D*, 73(2):021501, 2006.

[86] Franz E Schunck and Andrew R Liddle. The gravitational redshift of boson stars. *Physics Letters B*, 404(1-2):25–32, 1997.

[87] Caio FB Macedo, Vitor Cardoso, Luís CB Crispino, and Paolo Pani. Quasinormal modes of relativistic stars and interacting fields. *Physical Review D*, 93(6):064053, 2016.

[88] Raissa FP Mendes and Huan Yang. Tidal deformability of boson stars and dark matter clumps. *Classical and Quantum Gravity*, 34(18):185001, 2017.

[89] Pedro VP Cunha, José A Font, Carlos Herdeiro, Eugen Radu, Nicolas Sanchis-Gual, and Miguel Zilhão. Lensing and dynamics of ultracompact bosonic stars. *Physical Review D*, 96(10):104040, 2017.

[90] Valeria Diemer, Keno Eilers, Betti Hartmann, Isabell Schaffer, and Catalin Toma. Geodesic motion in the space-time of a noncompact boson star. *Physical Review D*, 88(4):044025, 2013.

[91] Caio FB Macedo, Paolo Pani, Vitor Cardoso, and Luís CB Crispino. Astrophysical signatures of boson stars: quasinormal modes and inspiral resonances. *Physical Review D*, 88(6):064046, 2013.

[92] Philippe Grandclement, Claire Somé, and Eric Gourgoulhon. Models of rotating boson stars and geodesics around them: new type of orbits. *Physical Review D*, 90(2):024068, 2014.

[93] Z Meliani, FH Vincent, P Grandclément, E Gourgoulhon, R Monceau-Baroux, and O Straub. Circular geodesics and thick tori around rotating boson stars. *Classical and Quantum Gravity*, 32(23):235022, 2015.

[94] M Grould, Z Meliani, FH Vincent, P Grandclément, and E Gourgoulhon. Comparing timelike geodesics around a kerr black hole and a boson star. *Classical and Quantum Gravity*, 34(21):215007, 2017.

[95] Caio FB Macedo, Paolo Pani, Vitor Cardoso, and Luís CB Crispino. Into the lair: gravitational-wave signatures of dark matter. *The Astrophysical Journal*, 774(1):48, 2013.

[96] Philippe Grandclément. Light rings and light points of boson stars. *Physical Review D*, 95(8):084011, 2017.

[97] Michael Kesden, Jonathan Gair, and Marc Kamionkowski. Gravitational-wave signature of an inspiral into a supermassive horizonless object. *Physical Review D*, 71(4):044015, 2005.

[98] Yves Brihaye, Valeria Diemer, and Betti Hartmann. Charged q-balls and boson stars and dynamics of charged test particles. *Physical Review D*, 89(8):084048, 2014.

[99] Ricardo Becerril, Tonatiuh Matos, and Luis Ureña-López. Geodesics around oscillatons. *General Relativity and Gravitation*, 38(4):633–641, 2006.

[100] Mariusz P Dabrowski and Franz E Schunck. Boson stars as gravitational lenses. *The Astrophysical Journal*, 535(1):316, 2000.

[101] Franz E Schunck, Burkhard Fuchs, and Eckehard W Mielke. Scalar field haloes as gravitational lenses. *Monthly Notices of the Royal Astronomical Society*, 369(1):485–491, 2006.

[102] Hyerim Noh, Jai-chan Hwang, and Chan-Gyung Park. Axion as a cold dark matter candidate: Proof to fully nonlinear order. *The Astrophysical Journal*, 846(1):1, 2017.

[103] Jan Veltmaat, Jens C Niemeyer, and Bodo Schwabe. Formation and structure of ultralight bosonic dark matter halos. *Physical Review D*, 98(4):043509, 2018.

[104] Nitsan Bar, Diego Blas, Kfir Blum, and Sergey Sibiryakov. Galactic rotation curves versus ultralight dark matter: Implications of the soliton-host halo relation. *Physical Review D*, 98(8):083027, 2018.

[105] Andrei Khmelnitsky and Valery Rubakov. Pulsar timing signal from ultralight scalar dark matter. *Journal of Cosmology and Astroparticle Physics*, 2014(02):019, 2014.

[106] Diego Blas, Diana López Nacir, and Sergey Sibiryakov. Ultralight dark matter resonates with binary pulsars. *Physical review letters*, 118(26):261102, 2017.

[107] Diego Blas. New orbitals probes of ultra-light dark matter. *International Journal of Modern Physics A*, 33(34):1845018, 2018.

[108] Nitsan Bar, Kfir Blum, Thomas Lacroix, and Paolo Panci. Looking for ultralight dark matter near supermassive black holes. *arXiv preprint arXiv:1905.11745*, 2019.

[109] Hirotaka Yoshino and Hideo Kodama. Gravitational radiation from an axion cloud around a black hole: Superradiant phase. *Progress of Theoretical and Experimental Physics*, 2014(4):043E02, 2014.

[110] Richard Brito, Vitor Cardoso, and Paolo Pani. Black holes as particle detectors: evolution of superradiant instabilities. *Classical and Quantum Gravity*, 32(13):134001, 2015.

[111] Pedro VP Cunha, Carlos AR Herdeiro, Eugen Radu, and Helgi F Rúnarsson. Shadows of kerr black holes with scalar hair. *Physical review letters*, 115(21):211102, 2015.

[112] FH Vincent, E Gourgoulhon, C Herdeiro, and E Radu. Astrophysical imaging of kerr black holes with scalar hair. *Physical Review D*, 94(8):084045, 2016.

[113] Nicola Franchini, Paolo Pani, Andrea Maselli, Leonardo Gualtieri, Carlos AR Herdeiro, Eugen Radu, and Valeria Ferrari. Constraining black holes with light boson hair and boson stars using epicyclic frequencies and quasiperiodic oscillations. *Physical Review D*, 95(12):124025, 2017.

[114] Yueying Ni, Menglei Zhou, Alejandro Cardenas-Avendano, Cosimo Bambi, Carlos AR Herdeiro, and Eugen Radu. Iron kα line of kerr black holes with scalar hair. *Journal of Cosmology and Astroparticle Physics*, 2016(07):049, 2016.

[115] Daniel Baumann, Horng Sheng Chia, and Rafael A Porto. Probing ultralight bosons with binary black holes. *Physical Review D*, 99(4):044001, 2019.

[116] Saul A Teukolsky. Rotating black holes: Separable wave equations for gravitational and electromagnetic perturbations. *Physical Review Letters*, 29(16):1114, 1972.

[117] Dieter R Brill, Paul L Chrzanowski, C Martin Pereira, Edward D Fackerell, and James R Ipser. Solution of the scalar wave equation in a kerr background by separation of variables. *Physical Review D*, 5(8):1913, 1972.

[118] Milton Abramowitz and Irene A Stegun. *Handbook of mathematical functions: with formulas, graphs, and mathematical tables*, volume 55. Courier Corporation, 1965.

[119] G. Dahlquist and A. Björck. *Numerical Methods*. Dover Publications, 2003.

[120] George David Birkhoff and Rudolph Ernest Langer. *Relativity and modern physics*. Harvard University Press, 1923.

[121] Nils Voje Johansen and Finn Ravndal. On the discovery of birkhoff's theorem. *General Relativity and Gravitation*, 38(3):537–540, 2006.

[122] Pau Amaro-Seoane, Heather Audley, Stanislav Babak, John Baker, Enrico Barausse, Peter Bender, Emanuele Berti, Pierre Binetruy, Michael Born, Daniele Bortoluzzi, et al. Laser interferometer space antenna. *arXiv preprint arXiv:1702.00786*, 2017.

[123] Pau Amaro-Seoane, Jonathan R Gair, Marc Freitag, M Coleman Miller, Ilya Mandel, Curt J Cutler, and Stanislav Babak. Intermediate and extreme mass-ratio inspirals: astrophysics, science applications and detection using lisa. *Classical and Quantum Gravity*, 24(17):R113, 2007.

[124] Jonathan R Gair, Michele Vallisneri, Shane L Larson, and John G Baker. Testing general relativity with low-frequency, space-based gravitational-wave detectors. *Living Reviews in Relativity*, 16(1):7, 2013.

[125] Miguel C Ferreira, Caio FB Macedo, and Vitor Cardoso. Orbital fingerprints of ultralight scalar fields around black holes. *Physical Review D*, 96(8):083017, 2017.

[126] J Bertrand. Theoreme relatif au mouvement dÕun point attirŽ vers un centre fixe. *C. R. Acad. Sci. Paris*, 77, 1873.

[127] Robert H Berman and JW-K Mark. Stellar dynamics in thin disk galaxies. i-a unified approach to hydrodynamic and orbit theories. *The Astrophysical Journal*, 216:257–270, 1977.

[128] Robert H Berman and James WK Mark. Stellar dynamics in thin disk galaxies. ii. stellar hydrodynamic equations. *The Astrophysical Journal*, 231:388–400, 1979.

[129] G Contopoulos. The particle resonance in spiral galaxies. nonlinear effects. *The Astrophysical Journal*, 181:657–684, 1973.

[130] George Contopoulos. Periodic orbits near the particle resonance in galaxies. *Astronomy and Astrophysics*, 64:323–332, 1978.

[131] James Binney and Scott Tremaine. *Galactic dynamics*, volume 20. Princeton university press, 2011.

[132] Herbert Goldstein, Charles Poole, and John Safko. *Classical mechanics*. AAPT, 2002.

[133] Vladimir Igorevich Arnol'd. Small denominators and problems of stability of motion in classical and celestial mechanics. *Russian Mathematical Surveys*, 18(6):85–191, 1963.

[134] Jacques Henrard. The adiabatic invariant theory and applications. In *Hamiltonian Dynamics. Theory and Applications*, pages 77–141. Springer, 2005.

[135] Peter Goldreich and Scott Tremaine. Disk-satellite interactions. *Astrophysical Journal*, 241(1):425–441, 1980.

[136] Peter Goldreich and Scott Tremaine. The excitation of density waves at the lindblad and corotation resonances by an external potential. *Astrophysical Journal*, 233(3):857–871, 1979.

[137] D Lynden-Bell and AJ Kalnajs. On the generating mechanism of spiral structure. *Monthly Notices of the Royal Astronomical Society*, 157(1):1–30, 1972.

[138] G Contopoulos and P Grosbøl. Orbits in barred galaxies. *Astronomy and Astrophysics Review*, 1(3):261–289, 1989.

[139] Daniel Ceverino and Anatoly Klypin. Resonances in barred galaxies. *Monthly Notices of the Royal Astronomical Society*, 379(3):1155–1168, 2007.

[140] Reinhard Genzel, Frank Eisenhauer, and Stefan Gillessen. The galactic center massive black hole and nuclear star cluster. *Reviews of Modern Physics*, 82(4):3121, 2010.

[141] Gravity Collaboration, R Abuter, A Amorim, N Anugu, M Bauböck, M Benisty, JP Berger, N Blind, H Bonnet, W Brandner, A Buron, et al. Detection of the gravitational redshift in the orbit of the star s2 near the galactic centre massive black hole. *Astronomy & Astrophysics*, 615:L15, 2018.

[142] A. Amorim, M. Bauböck, M. Benisty, J.-P. Berger, Y. Clénet, V. Coudé du Forest, T. de Zeeuw, J. Dexter, G. Duvert, A. Eckart, F. Eisenhauer, Miguel C. Ferreira, F. Gao, Paulo J.V. Garcia, E. Gendron, R. Genzel, S. Gillessen, P. Gordo, M. Habibi, M. Horrobin, A. Jimenez-Rosales, L. Jocou, P. Kervella, S. Lacour, J.-B. Le Bouquin, P. Léna, T. Ott, M. Pössel, T. Paumard, K. Perraut, G. Perrin, O. Pfuhl, G. Rodriguez Coira, G. Rousset, O. Straub, C. Straubmeier, E. Sturm, F. Vincent, S. von Fellenberg, I. Waisberg, and F. Widmann. Scalar field effects on the orbit of s2 star. *To be published*, 2019.

[143] M Grould, FH Vincent, T Paumard, and G Perrin. General relativistic effects on the orbit of the s2 star with gravity. *Astronomy & Astrophysics*, 608:A60, 2017.

[144] Stefan Gillessen, F Eisenhauer, S Trippe, T Alexander, R Genzel, F Martins, and T Ott. Monitoring stellar orbits around the massive black hole in the galactic center. *The Astrophysical Journal*, 692(2):1075, 2009.

[145] Masaharu Tanabashi, K Hagiwara, K Hikasa, K Nakamura, Y Sumino, F Takahashi, J Tanaka, K Agashe, G Aielli, C Amsler, et al. Review of particle physics. *Physical Review D*, 98(3):030001, 2018.

[146] Clifford M Will. Testing the general relativistic “no-hair” theorems using the galactic center black hole sagittarius a. *The Astrophysical Journal Letters*, 674(1):L25, 2008.

[147] Miguel Preto and Prasenjit Saha. On post-newtonian orbits and the galactic-center stars. *The Astrophysical Journal*, 703(2):1743, 2009.

[148] Lorenzo Iorio and Fupeng Zhang. On the post-keplerian corrections to the orbital periods of a two-body system and their application to the galactic center. *The Astrophysical Journal*, 839(1):3, 2017.

[149] David Merritt, Tal Alexander, Seppo Mikkola, and Clifford M Will. Testing properties of the galactic center black hole using stellar orbits. *Physical Review D*, 81(6):062002, 2010.

[150] Pau Amaro-Seoane. X-mris: Extremely large mass-ratio inspirals. *arXiv preprint arXiv:1903.10871*, 2019.

[151] Lorenzo Iorio. Post-keplerian effects on radial velocity in binary systems and the possibility of measuring general relativity with the star s2 in 2018. *Monthly Notices of the Royal Astronomical Society*, 472(2):2249–2262, 2017.

[152] Miguel C. Ferreira. How do scalar-field dark matter halos react to orbiting bodies? *Physical Review D*, 99(10):103008, 2019.

[153] Norbert Straumann. *General relativity*. Springer Science & Business Media, 2012.

[154] G.B. Arfken, H.J. Weber, and F.E. Harris. *Mathematical Methods for Physicists: A Comprehensive Guide*. Elsevier Science, 2011.

[155] Eric Jones, Travis Oliphant, Pearu Peterson, et al. SciPy: Open source scientific tools for Python, 2001–. URL `http://www.scipy.org/`. [Online; accessed September 19, 2019].

[156] Saul A Teukolsky. Stability of the iterated crank-nicholson method in numerical relativity. *Physical Review D*, 61(8):087501, 2000.

[157] E. Hairer, S.P. Nørsett, and G. Wanner. *Solving Ordinary Differential Equations I: Nonstiff Problems*. Springer Series in Computational Mathematics. Springer Berlin Heidelberg, 2008.

[158] Eve C Ostriker. Dynamical friction in a gaseous medium. *The Astrophysical Journal*, 513(1):252, 1999.

[159] Eric Poisson and Clifford M Will. *Gravity: Newtonian, post-newtonian, relativistic*. Cambridge University Press, 2014.

[160] Michael Paul Hobson, George P Efstathiou, and Anthony N Lasenby. *General relativity: an introduction for physicists*. Cambridge University Press, 2006.

[161] Hideo Kodama and Misao Sasaki. Cosmological perturbation theory. *Progress of Theoretical Physics Supplement*, 78:1–166, 1984.

[162] E Bertschinger. Cosmological dynamics: Course 1, in proceedings of the les houches school, 1996.

[163] James M Bardeen. Gauge-invariant cosmological perturbations. *Physical Review D*, 22 (8):1882, 1980.

[164] Michele Maggiore. *Gravitational Waves: Theory and Experiments*, volume 1. Oxford university press, 2008.

[165] Istvan Szapudi and Viktor G Czinner. Cosmological perturbations from a group theoretical point of view. *Classical and Quantum Gravity*, 29(1):015007, 2011.

[166] Guido Walter Pettinari. The intrinsic bispectrum of the cosmic microwave background [phd thesis]. *arXiv preprint arXiv:1405.2280*, 2014.

[167] Sergei Kopeikin, Michael Efroimsky, and George Kaplan. *Relativistic celestial mechanics of the solar system*. John Wiley & Sons, 2011.

[168] PJE Peebles. Star distribution near a collapsed object. *The Astrophysical Journal*, 178: 371–376, 1972.

[169] JN Bahcall and R Al Wolf. Star distribution around a massive black hole in a globular cluster. *The Astrophysical Journal*, 209:214–232, 1976.

[170] AP Lightman and SL Shapiro. The distribution and consumption rate of stars around a massive, collapsed object. *The Astrophysical Journal*, 211:244–262, 1977.

[171] Holger Baumgardt, Junichiro Makino, and Toshikazu Ebisuzaki. Massive black holes in star clusters. ii. realistic cluster models. *The Astrophysical Journal*, 613(2):1143, 2004.

[172] Miguel Preto, David Merritt, and Rainer Spurzem. N-body growth of a bahcall-wolf cusp around a black hole. *The Astrophysical Journal Letters*, 613(2):L109, 2004.

[173] Marc Freitag, Pau Amaro-Seoane, and Vassiliki Kalogera. Stellar remnants in galactic nuclei: mass segregation. *The Astrophysical Journal*, 649(1):91, 2006.

[174] M Habibi, S Gillessen, O Pfuhl, F Eisenhauer, PM Plewa, S von Fellenberg, F Widmann, T Ott, F Gao, I Waisberg, et al. Spectroscopic detection of a cusp of late-type stars around the central black hole in the milky way. *The Astrophysical Journal Letters*, 872(1):L15, 2019.

[175] Pranesh A Sundararajan, Gaurav Khanna, and Scott A Hughes. Towards adiabatic waveforms for inspiral into kerr black holes: A new model of the source for the time domain perturbation equation. *Physical Review D*, 76(10):104005, 2007.